CONTROLLING MARTENSITIC TRANSFORMATION CHARACTERISTICS IN DEFECT-FREE NITI SHAPE MEMORY ALLOYS FABRICATED USING LASER POWDER BED FUSION

A Dissertation

by

LEI XUE

Submitted to the Graduate and Professional School of
Texas A&M University
in partial fulfillment of the requirements for the degree of

DOCTOR OF PHILOSOPHY

Chair of Committee,	Ibrahim Karaman
Committee Members,	Alaa Elwany
	Raymundo Arroyave
	Dimitris Lagoudas
Head of Department,	Ibrahim Karaman

December 2021

Major Subject: Materials Science and Engineering

ABSTRACT

Laser powder bed fusion is a promising additive manufacturing technique for the fabrication of NiTi shape memory alloy parts with complex geometries that are otherwise difficult to fabricate through traditional processing methods. The technique is particularly attractive for the biomedical applications of NiTi SMAs, such as stents, implants, and dental and surgical devices, where primarily the superelastic effect is exploited. However, few additively manufactured NiTi parts have been reported to exhibit superelasticity under tension in the as-printed condition.

Laser powder bed fusion was utilized to fabricate fully dense, near-equiatomic ($Ni_{50.1}Ti_{49.9}$), Ni-rich NiTi ($Ni_{50.8}Ti_{49.2}$ and $Ni_{51.2}Ti_{48.8}$) shape memory alloy parts which exhibited tensile ductility up to 16%, shape memory strain of 6%, and tensile superelasticity up to 6%, almost twice the maximum reported value in the literature. The selection of optimum processing parameters that yielded fully dense parts was guided by a process optimization framework based on a computationally inexpensive analytical model used to predict the melt pool dimensions based on single-track experiments. This framework allowed for constructing printability maps for the present NiTi shape memory alloys and revealed that fully dense parts could be printed over a wide range of process parameters. By controlling the process parameters, in particular laser power, laser scan speed, and volumetric energy density, in the processing space that result in fully dense parts, it was demonstrated systematically that the composition of the printed parts could be precisely changed by controlling the evaporation of Ni. The flexibility of parameter selection to print defect-free NiTi SMAs and composition control by

preferential evaporation of Ni opens the possibility to print functional NiTi parts or devices without post-processing. Crystallographic texture analysis demonstrated that the as-printed NiTi parts had a strong preferential texture for superelasticity, a factor that needs to be carefully considered when complex shaped parts are to be subjected to combined loadings. Transmission electron microscopy investigations revealed the presence of nano-sized oxide particles and Ni-rich precipitates in the as-printed parts of $Ni_{50.8}Ti_{49.2}$ and $Ni_{51.2}Ti_{48.8}$, which play a role in the improved superelasticity by suppressing inelastic accommodation mechanisms for martensitic transformation.

DEDICATION

I dedicate this dissertation work:

To the loving memory of my grandmother Shufang Song.

To my father Youbing Xue.

To my mother Yaping Huang.

Finally, to my girlfriend Yue Du.

ACKNOWLEDGEMENTS

Firstly, I would like to express my special thanks to Dr. Ibrahim Karaman for accepting as his student and supporting my research here. His attitude towards research influenced me a lot as he is dedicated to research, and he never compromises to the difficulties. Apart from his enthusiasm and diligence in research, he has also inspired me by his knowledge and thorough understanding of the microstructure. I am also thankful to him for his tremendous support and guidance during my Ph.D and his efforts in providing a wonderful environment for performing research.

I would also like to thank my committee members, Dr. Alaa Elwany, Dr. Raymundo Arroyave, and Dr. Dimitris Lagoudas, for their guidance and support throughout my PhD study. I feel lucky to have the opportunity to work with them and it has been a great experience.

I highly appreciate Dr. Kadri Atli Can for his support and collaboration work on additive manufacturing of NiTi. His knowledge and skills on shape memory alloys is truly remarkable, and our discussion has been very useful. A special thanks to Cheng Zhang and Dr. Bing Zhang for their collaboration and assistance on this work. I would also like to thank Dr. Abhinav Srivastava, Dr. Sezer Picak and Dr. Asher Leff for their collaboration on crystallographic texture characterizations and transmission electron microscopy studies. I would also like to thank Nathan Hite for his help on sample characterization and handling. I would also like to thank Dr. Anup Bandopadhay for

conducting a number of DSC experiments. I would also like to thank Michael Eluverd for his support on material cutting and the great fun on his ranch.

I would also like to thank Dr. Ji Ma and Dr. Brian Franco for their guidance and valuable discussion on NiTi projects. I would also like to thank Raiyan Seede for our valuable discussion on general additive manufacturing.

Special thanks to the great students, staff and faculty of Material Science and Engineering department. Thanks also goes to Dr. Tejas Umale, Wenhao Lin and many more friends in our research group for friendship.

I would also like to thank my fluffy friends Angela and Egg Yellow.

Lastly, I would like to thank my family and girlfriend for their consistent support.

CONTRIBUTORS AND FUNDING SOURCES

Contributors

This work was supervised by a dissertation committee consisting of Professor Ibrahim Karaman and Professor Raymundo Arroyave of the Department of Materials Science and Engineering, Professor Alaa Elwany of the Department of Industrial & Systems Engineering, and Professor Dimitris Lagoudas of the Department of Aerospace Engineering. Part of the thermomechanical tests in Chapter III were performed by Dr. Kadri Atli Can of the Department of Material Science and Engineering. The Eagar and Tsai model predictions and printability maps in Chapter III and IV were provided by Dr. Bing Zhang and Cheng Zhang of the Department of Industrial & Systems Engineering. The TEM figures in Chapter III were provided by Dr. Sezer Picak of the Department of Mechanical Engineering. The XRD experiments and EBSD figures in Chapter IV were conducted/provided by Dr. Abhinav Srivastava of the Department of Materials Science and Engineering. The TEM figures in Chapter IV were provided by Dr. Asher of the Army Research Lab. The thermal diffusivity measurements were provided by Dr. Adam Wilson from Army research Lab. All other work conducted for the dissertation was completed by the student independently.

Funding Sources

This work was made possible in part by Carpenter Technology Corporation, U.S. Army Research Laboratory under cooperative agreement No. W911NF1920264, Qatar

National Research Fund (a member of The Qatar Foundation) under grant number NPRP12-S No: 0131-190029, and U.S. National Science Foundation under grant number1846676.

NOMENCLATURE

A_f	Austenite Finish Temperature
AM	Additive Manufacturing
A_s	Austenite Start Temperature
BSE	Back Scatter Electron
σ_{SIM}	Critical Stress for Martensitic Transformation
DED	Directed Energy Deposition
DSC	Differential Scanning Calorimetry
EBM	Electron Beam Melting
EBSD	Electron Backscatter Diffraction
EDS	Energy-Dispersive X-ray Spectroscopy
E-T	Eagar and Tsai
h	Hatch Spacing
HAADF	High Angle Annular Dark Field
LED	Linear Energy Density
L-PBF	Laser Powder Bed Fusion
M_f	Martensite Finish Temperature
M_s	Martensite Start Temperature
MT	Martensitic Transformation
OM	Optical Microscopy

p	Laser Power
PSD	Particle Size Distribution
SE	Superelasticity
SEM	Scanning Electron Microscope
SIM	Stress Induced Martensite
SMA	Shape Memory Alloy
SHT	Solution Heat Treatment
STEM	Scanning Transmission Elec tron Microscope
TT	Transformation Temperature
v	Laser Scan Speed
VED	Volumetric Energy Density
wire-EDM	Wire Electrical Discharge Machining
XRD	X-ray Diffraction

TABLE OF CONTENTS

Page

LIST OF FIGURES

Page

LIST OF TABLES

Page

CHAPTER I

INTRODUCTION*

1.1 Motivation

Nickel-titanium is the most commonly used shape memory alloy (SMA) due to its excellent function properties including shape memory effect and superelasticity. And its biocompatibility, corrosion resistance and low stiffness have made this alloy attractive to many biomedical applications. However, NiTi is not well suited for conventional machining processes for fabricating near-net-shape devices. Additive manufacturing (AM) has been identified as a potential fabrication method for creating otherwise hard-to-machine NiTi parts, enabling the fabrication of complex geometries that are not possible or prohibitively costly using conventional machining processes. Compared with the direct energy deposition (DED), laser powder bed fusion (L-PBF) provides better geometry accuracy and surface finish owing to its smaller beam size and finer powder size. In the existing literature, how melt pool morphology and dimensions affect the resulting porosity/defects in additively manufactured NiTi has not been laid out in a systematic fashion.

The aim of this work is to understand the effect of process parameters during L-PBF on the melt pool by developing a systematic framework. Melt pool geometry will

---

*Portions of this chapter are reprinted with permission from "Controlling Martensitic Transformation Characteristics in Defect-Free NiTi Shape Memory Alloys Fabricated Using Laser Powder Bed Fusion and a Process Optimization Framework" by L. Xue, K. C. Atli, S. Picak, C. Zhang, B. Zhang, A. Elwany, R. Arroyave, and I. Karaman. Acta Materialia 215 (2021) 117017

be studied to eliminate the resulting porosity in the built NiTi part. And Ni evaporation during the process will be identified for controlling transformation temperatures from a given powder composition. The thermomechanical properties and microstructures of the additively manufactured NiTi will be investigated to evaluate their functional properties and understand the underlying physics.

The motivation behind minimizing the porosity/defects through process parameter optimization is to improve the mechanical and functional properties of AM NiTi to the level of bulk parts fabricated with ingot metallurgy and minimize part-to-part variability. Better flexibility of parameter selection to print defect-free NiTi SMAs and composition control by preferential evaporation of Ni shall open the possibility to print NiTi SMA parts or devices with desired functional properties (e.g., transformation temperatures) in as-fabricated condition. And hopefully, perfect tensile superelasticity could be achieved in the as-fabricated condition, which is challenging and rare in the existing literature. The success of eliminating defects and understanding the microstructure evolution behind shall accelerate the penetration of AM NiTi into many application areas.

1.2 Objective

Very limited amount of systematic work has been done in additive manufacturing to explore parameter selection for fabricating defect-free NiTi parts. Also, good tensile superelasticity has not been achieved for additive manufactured NiTi as such functional properties are critical for its application. Hence the objectives of this study are:

1. To better understand the effect of processing parameters, single tracks will be printed with difference sets of laser power (*P*) and scanning speed (*v*) within the capability of the printer. The dimensions of the melt pools will be characterized by image processing, and the single tracks will be categorized by the morphology or the relationship of melt pool dimensions.
2. A computational inexpensive Eagar-Tsai (E-T) model will be calibrated with the experimental data and used to predict the melt pool dimensions. And the printability will be categorized into good, keyholing, lack of fusion and balling based on either single-track morphology, or the melt pool geometry predicted by the E-T model. Thus, the parameters combinations leading to detrimental defects can be identified and avoided during parameter selection process.
3. The maximum hatch spacing criteria will be applied based on melt pool geometry to ensure enough remelting between the adjacent tracks. The *P* and *v* combinations within in the good region will be selected with their appropriate hatch spacing (*h*) for fabricating fully dense NiTi.
4. For the AM NiTi prints, Archimedes' density will be measured, and cross-section surfaces will be investigated to further understand the possible porosity and defects.
5. The transformation temperatures of the as-fabricated NiTi samples will be investigated to understand the Ni evaporation and transformation temperature evolution during the L-PBF process.

6. Room temperature tensile ductility, shape memory effect and superelasticity will be evaluated the thermomechanical properties of the as-fabricated NiTi in this study.
7. Certain samples will be selected to study the crystallographic texture and microstructure. And this understanding shall further help us on engineering the printing process of NiTi.

A systematic approach containing experiments and modeling was taken to meet the above-mentioned objectives and is reported in the following chapters.

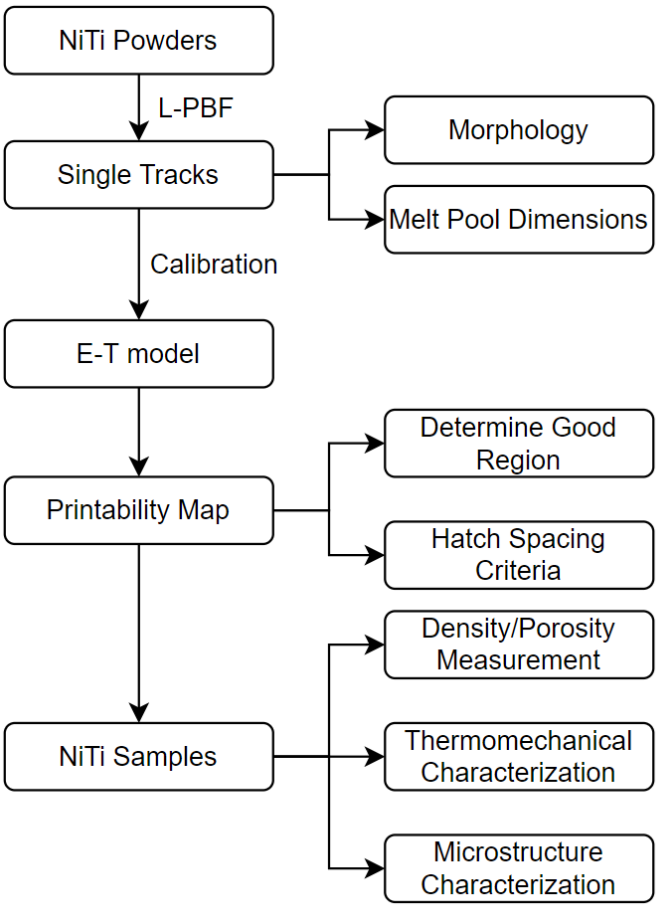

Figure 1.1 Schematic of the proposed approaches to fabricate and characterize defect-free NiTi through L-PBF.

CHAPTER II

BACKGROUND AND LITERATURE REVIEW*

In this chapter, a detailed background knowledge

2.1 Shape Memory Alloys

Shape memory alloys (SMAs) is a class of smart materials, which is capable to recover the deformation upon heating or applying magnetic field. The shape memory effect in NiTi is originated from the reversible transformation between a B2 austenite and B19' martensite. Upon loading and deformation in a self-accommodate martensite phase, the strain will be accommodated by the martensite reorientation and detwinning. The martensite will transform to austenite when heated up above austenite finish temperature (A_f) and recover the deformation. If the loading and deformation take place in austenite above A_f, the material may be deformed by stress induced martensitic transformation and detwinning of the transformed martensite. The stress induced martensite will transform back to austenite upon unloading and recover the deformation. This behavior is known as superelasticity.

These two unique features of shape memory alloys (SMAs), superelasticity (SE) and shape memory effect (SME) that result from a reversible martensitic phase transformation, have in the past decades resulted in the broad scale diffusion of these

---

*Portions of this chapter are reprinted with permission from "Controlling Martensitic Transformation Characteristics in Defect-Free NiTi Shape Memory Alloys Fabricated Using Laser Powder Bed Fusion and a Process Optimization Framework" by L. Xue, K. C. Atli, S. Picak, C. Zhang, B. Zhang, A. Elwany, R. Arroyave, and I. Karaman. Acta Materialia 215 (2021) 117017©2021 Elsevier Ltd

materials in many applications such as biomedical devices, actuators, couplings and seismic devices. NiTi is the material of choice for most of these applications, as it is the most widely researched and commercially available SMA, in addition to its superior shape memory properties, biocompatibility and corrosion resistance.

However, NiTi is not well suited for conventional machining processes that are required to bring the part to its final geometry, owing to its increased ductility, high toughness and high strain hardening, which cause excessive tool wear and burr formation [1-3]. Specialized techniques for machining NiTi such as cryogenic machining and wire electrical discharging machining (wire-EDM) provide alternative fabrication methods, however they are costly and limited in the geometries that can be produced.

2.2 Additive Manufacturing of NiTi

Additive manufacturing (AM) has been identified as a potential fabrication method for creating otherwise hard-to-machine NiTi parts, enabling the fabrication of complex geometries that are not possible or prohibitively costly using conventional machining processes. Efforts on additive manufacturing of NiTi date back to the beginning of the 2000s, with initial studies investigating the influence of processing parameters on the microstructure, mechanical properties, and phase transformation behavior [4, 5]. Powder bed fusion (PBF) [6-13] and directed energy deposition (DED) [14-20] additive manufacturing (AM) techniques have been extensively researched due to their capabilities of fabricating near-net-shape NiTi SMA parts, bypassing the associated costly machining challenges. PBF AM techniques such as laser-PBF (L-PBF) or electron beam melting (EBM) usually feature smaller beam size, finer powder size

and thinner layers, which results in better surface finish and geometrical accuracy, while DED offers more design freedom including changing the input powder composition during printing and can be used to repair or add additional material to existing components. Improved surface finish with less adherent particles is desired in biomedical applications such as implants for limiting the harmful Ni release [21], and substantial attention has been given to L-PBF of NiTi for this reason.

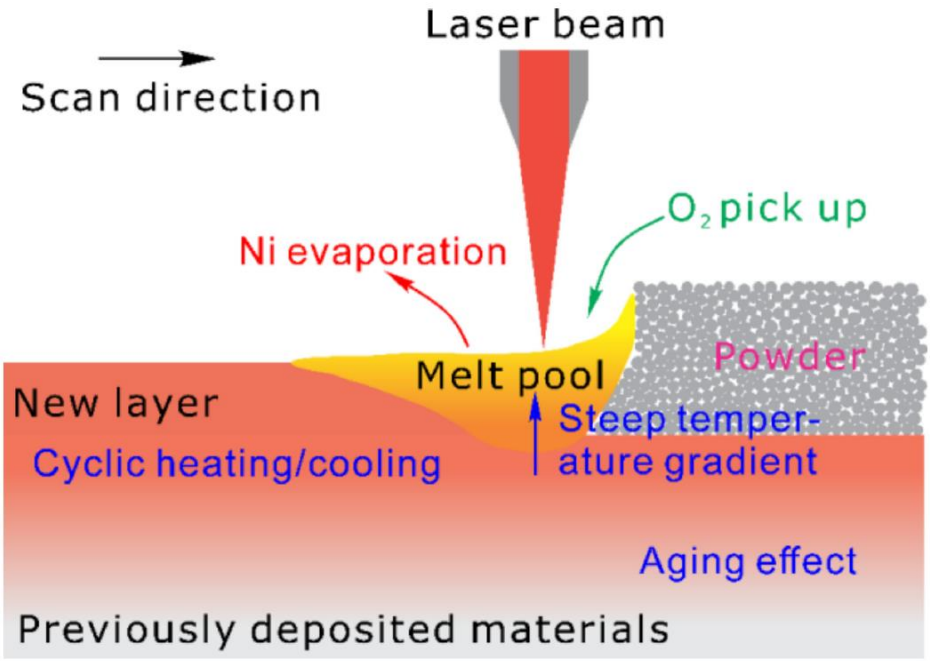

Figure 2.1 Schematic of the melt pool behavior in the L-PBF process. Reprinted from[22]

2.3 Optimization of Process Parameters

Considerable research efforts have been devoted to the optimization and selection of the process parameters to build AM NiTi SMA parts [11, 23-27]. This is

primarily because, unlike other easy to print conventional alloys such as Ti6Al4V, Ni-based superalloys, or stainless steel, the composition and microstructure of the printed NiTi parts are as important as the build quality/density since they greatly influence the functional properties such as transformation temperatures, shape memory and superelastic strain, which are critical for applications. Unlike conventional AM alloys, AM NiTi parts are also known to suffer from processing-induced micro-defects(Figure 2.2) such as balling, keyholing, and lack of fusion, and macroscopic defects such as delamination, cracks, and warping. A careful selection of processing parameters is therefore required to be able to circumvent these defects and fabricate quality parts while at the same time meeting the application requirements in terms of shape memory properties.

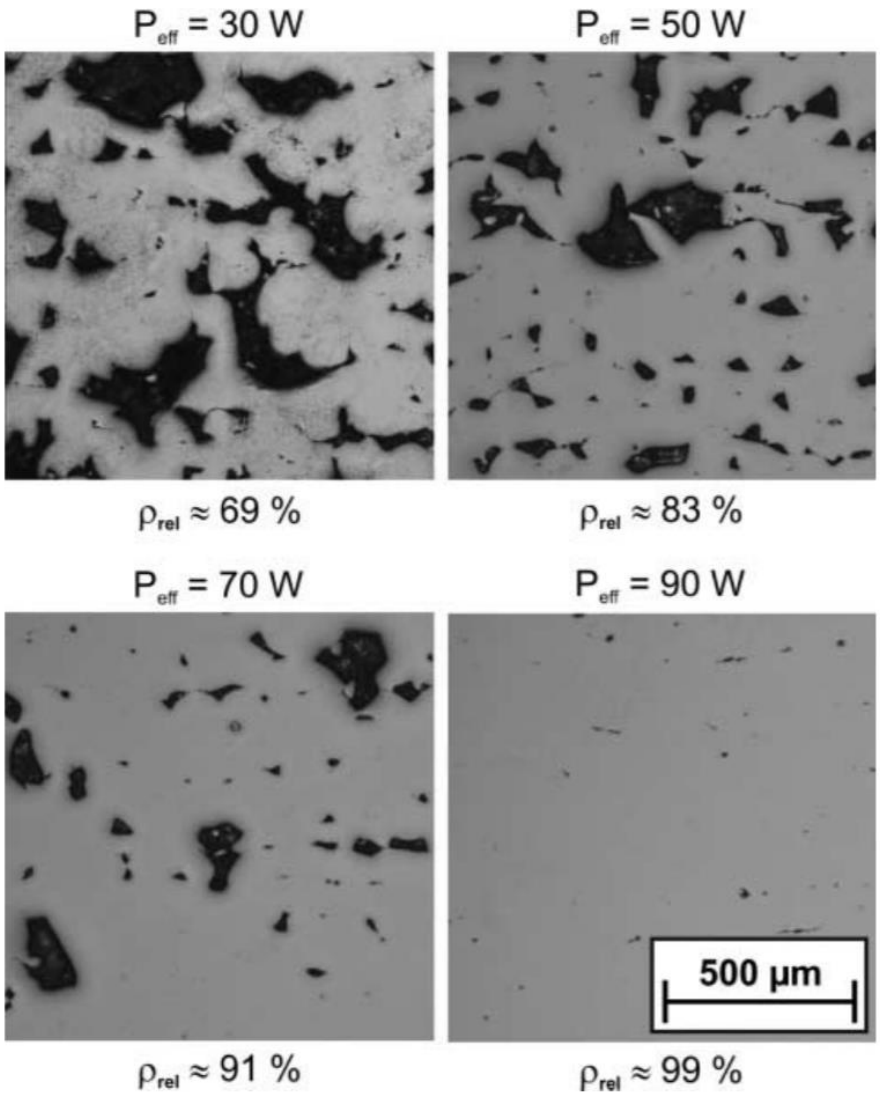

Figure 2.2 Micrographs of the cross sections showing different porosity for different effective laser powers. Reprinted from [28]

When existing literature on AM of NiTi SMAs is investigated, it is seen that optimization of process parameters is typically performed via a broad sweep of the parameter space, including power, scan speed, and hatch spacing, which is a time consuming and expensive procedure. Although several model-based approaches that

predict melt pool dimensions and expedite the search for optimized processing parameters have been proposed for easy-to-print alloys such as stainless steels or Ni-based superalloys [29-31], how melt pool dimensions affect the resulting porosity levels in a built part and how to eliminate them has not been laid out in a systematic fashion. In addition, due to the high sensitivity of NiTi SMAs and the possible hardware differences in each commercial AM system, process parameter sets generated by one group might be rendered unusable by others. Establishing a framework to implement model-based approaches to building porosity-free parts is therefore essential. Our group have recently developed such a framework based on the simple analytical Eagar and Tsai (E-T) model for predicting melt pool geometry, combined with single-track experiments, model uncertainty analysis, and a geometrical hatch spacing selection criterion to investigate the range of process parameters for AF9628 martensitic steels, which consistently led to full densification of Laser Powder Bed Fusion (L-PBF) parts [32]. The same methodology will be employed in the current study to optimize process parameters for printing two different compositions of NiTi SMAs with minimal or no porosity. As previously mentioned, process parameter optimization is an even more critical issue for SMAs, since these functional materials need to conform to additional standards in terms of shape memory properties, such as transformation temperatures and shape recoverability.

During L-PBF, excessive energy input can trap the vapor within the melt pool causing spherical pores, while insufficient energy input may lead to unmolten parts between the melt pools or weak bonding (microcracks) between layers. Although a

porous structure [9, 21, 33] may be preferred for biomedical implants for the low stiffness [9], pores may lead to early failure through crack formation and propagation, bringing serious consequences especially in applications requiring multiple actuations. Due to the characteristic high cooling rate and steep temperature gradient in L-PBF, residual stresses in the printed parts may also result in unpredictable mechanical behavior or cause macroscopic defects such as warping and delamination. Recent studies have suggested that the use of strip scanning patterns with shorter scanning length may favor smaller thermal gradient. Parts printed with such scanning patterns exhibited as high as 16% tensile ductility [34]. The highest tensile ductility reported so far for AM NiTi is ~20% which was achieved by utilizing a similar scanning pattern together with 25 ppm oxygen level in the build chamber [25], which is much lower than the 500 ppm suggested by ASTM F2063-05.

There are multiple factors that need to be considered during L-PBF of NiTi in order to fabricate defect-free and fully dense parts, e.g., powder composition and quality, the choice of scanning strategy, selection of processing parameters. Considerable research has been devoted for the optimal selection of processing parameters in different platforms, however it is a fact that one set of parameters optimized for one system may not always produce the same results due to hardware differences. Our group recently reported a framework-based method [32] which utilizes a simple analytical model to predict melt pool dimensions as a function of material properties and processing parameters, paired with single tracks experiments to identify the window of feasible process parameters for different alloys including NiTi. This framework saves

considerable efforts in parameter optimization compared with performing experiments spanning the full parameter space for a given kind of powder. The framework-based methodologies [32, 35] from single tracks are generally simplified for easy execution, and multiple detailed factors including the powder coverage/thickness after many layers, thermal history of the solidified layers, scanning strategies etc. were not considered. It is necessary to have a comprehensive understanding of these factors and the underlying physics together with precise predictions of the melt pool characteristics to build a reliable framework for streamlining the process of parameter selection.

2.4 Thermomechanical Properties of Additive Manufactured NiTi

Apart from producing parts with complex geometries, AM also has the capability of altering the matrix Ni/Ti ratio in NiTi SMAs through preferential evaporation of Ni [36-38] and inducing a unique defect structure due to rapid cooling [39], thus providing a feasible method to tailor the transformation temperatures and modify shape memory and mechanical properties. This versatility for AM-fabricated NiTi SMAs stems from the fact that functional properties of NiTi SMAs are highly sensitive to the Ni content and defect density, e.g., transformation temperatures drop about 20 °C per 0.1 at.% change above 50% Ni [40], and transformation temperature range increases and enthalpy decreases with an increase in dislocation density [41].

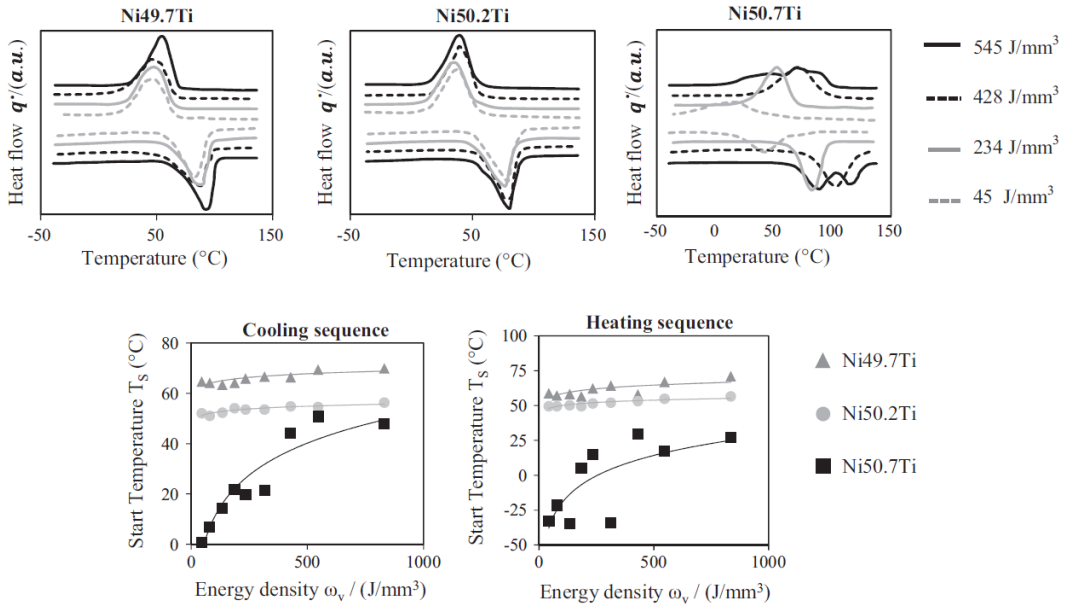

Figure 2.3 The effect of energy density on the martensitic and austenitic transformation start temperatures of NiTi with different compositions. Reprinted from [42]

NiTi parts fabricated using AM techniques have been reported to exhibit up to 10% recoverable compressive strain [10] and up to 8% tensile recoverable strain [25], comparable to NiTi parts fabricated via conventional ingot metallurgy techniques. However, the starting powder for these parts is usually a relatively Ni-lean NiTi powder (i.e. Ni < 50.5 at. %) and the printed parts typically have transformation temperatures above room temperature. Unfortunately, achieving SE in AM NiTi is not easy and straightforward compared to achieving SME. Firstly, in order to achieve SE in AM NiTi, the printed parts should have austenite finish (A_f) temperature lower than the testing temperature, which, for example, is generally as high as the body temperature for biomedical applications. This fact necessitates the use of a relatively Ni-rich NiTi

powder feedstock (i.e. Ni > 50.7 at. %) to be able to print NiTi parts with SE. As the laser or electron beam source in L-PBF causes differential evaporation of Ni from the powder [6, 7, 11, 25, 37, 42-46], processing parameters must be carefully selected to predict the resulting Ni content, and thus the transformation temperatures of the printed NiTi parts. Secondly, even if parts with transformation temperatures appropriate for a specific SE application are printed, perfect superelasticity might not be achieved. This occurs when the strength of the matrix is not high enough and the critical stress that induces martensite also induces slip in the parent phase during superelastic loading. Thirdly, the unique grain structure of the AM NiTi as a result of the epitaxial growth between successive layers, the inherent defect structure with porosity and residual stresses and the presence of any inclusions in the printed parts due to imperfections in the protective atmosphere of the building chamber or the impurities in the starting powder feedstock, might cause the part fail in a brittle manner without even showing a sign of superelasticity. Superelasticity has been reported in AM NiTi under both compressive and tensile stresses [11, 16, 33, 47-51], but the maximum tensile superelastic strain in as-fabricated condition was only 3% (Figure 2.4), accompanied by a relatively large residual strain, partly due to the abovementioned issues. Characterization of the tensile properties of AM NiTi is thus crucial since as-printed parts are more prone to fracture from defects (e.g., porosity and cracks) in tension as compared to in compression.

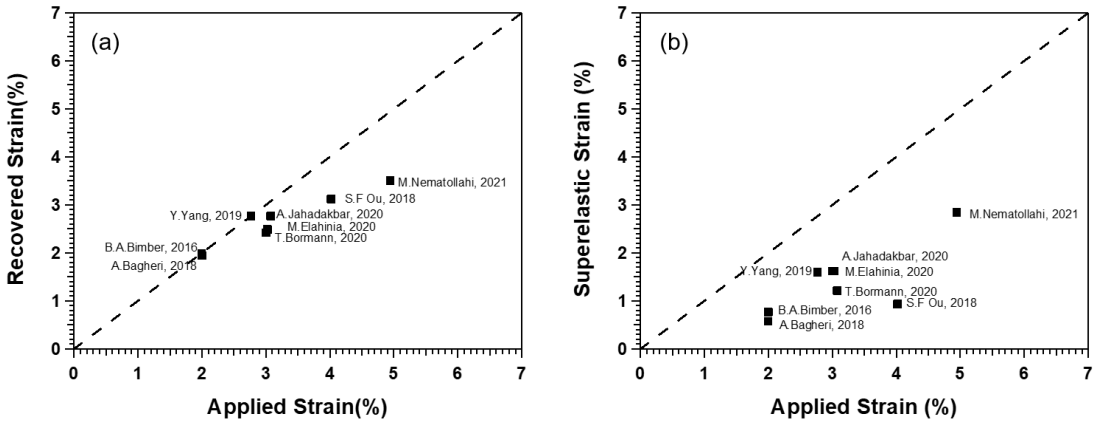

Figure 2.4 Summary of the tensile superelasticity results from existing literature on AM NiTi.

2.5 Crystallographic Texture and Microstructure

Control of the microstructure in AM NiTi is of paramount importance in order to improve the thermomechanical properties to a level close to those of NiTi fabricated by conventional ingot metallurgy. Texture has been known to greatly affect functional properties in single crystal and polycrystalline NiTi [52, 53], and studies have revealed the formation of preferred orientation in the direction of highest thermal gradient during the intrinsic epitaxial solidification in AM processes [12, 49, 54]. Utilizing a smaller hatch spacing value during printing has also been reported to result in a stronger texture and grain refinement [49]. In wrought Ni-rich NiTi, solution heat treatment to reach a matrix without secondary phases followed by aging heat treatment at 300 to 550 °C [55] is commonly used to modify the size and distribution of Ni-rich precipitates, strengthen the matrix against defect generation mechanisms and achieve SE. Although the effect of

aging effect on functional properties have been widely studied in NiTi fabricated using conventional ingot metallurgy [56-60], choosing the appropriate heat treatment parameters for AM NiTi is a challenging task, since the Ni content of the as-fabricated parts will usually be different than the starting powder and may vary depending on the selection of process parameters. In addition, AM NiTi parts are usually considered to be inhomogeneous due to the characteristic layer by layer fabrication in which different layers are aged and annealed for different times during printing. Post printing heat treatments have been successfully used for AM NiTi parts to grow Ni-rich precipitates [16] and improve SE [7, 61] of Ni-rich NiTi. However, regardless of the quality of the protective atmosphere, formation of oxides such as TiO_2 or $Ti_4Ni_2O_x$ is a critical problem during heat treatments at relatively high temperatures (e.g. solution heat treatment) that may impair shape memory behavior and durability. Hence, achieving good and stable SE in as-printed parts, without any post printing heat treatments is a technological challenge that must be overcome.

Hence, in order to demonstrate the above-mentioned challenges for AM NiTi, we have performed initial experiments on $Ni_{50.8}Ti_{49.2}$ powder. The morphology of single tracks and melt-pool dimensions have been analyzed for calibrating our Eagar-Tsai model. Printability map of process parameters has been generated to guide the printing process, and defect free samples have been fabricated and characterized.

CHAPTER III

CONTROLLING MARTENSITIC TRANSFORMATION CHARACTERISTICS IN DEFECT-FREE NITI SHAPE MEMORY ALLOYS FABRICATED FROM $NI_{51.1}TI_{48.9}$ (AT. %) AND $NI_{50.3}TI_{49.7}$ (AT. %) POWDER USING LASER POWDER BED FUSION AND A PROCESS OPTIMIZATION FRAMEWORK*

In this chapter, Laser Powder Bed Fusion (L-PBF) was utilized to fabricate fully dense, near-equiatomic ($Ni_{50.1}Ti_{49.9}$) and Ni-rich NiTi ($Ni_{50.8}Ti_{49.2}$) shape memory alloy (SMA) parts which exhibited tensile ductility up to 16%, shape memory strain of 6%, and tensile superelasticity up to 4%. Annealing heat treatments marginally improved the superelasticity of the as-fabricated Ni-rich NiTi parts due to the formation of a small volume fraction of Ni_4Ti_3 precipitates. The selection of optimum processing parameters that yielded fully dense parts was guided by a process optimization framework based on a computationally inexpensive analytical model used to predict the melt pool dimensions. The framework also included single-track experiments to validate the model predictions and a criterion for the maximum allowable hatch spacing to prevent the formation of lack of fusion porosity. This framework allowed for constructing L-PBF processing maps for the present NiTi SMAs and revealed that fully dense parts could be printed over a wide range of process parameters. By controlling the L-PBF process

---

*Reprinted with permission from "Controlling Martensitic Transformation Characteristics in Defect-Free NiTi Shape Memory Alloys Fabricated Using Laser Powder Bed Fusion and a Process Optimization Framework" by L. Xue, K. C. Atli, S. Picak, C. Zhang, B. Zhang, A. Elwany, R. Arroyave, and I. Karaman. Acta Materialia 215 (2021) 117017©2021 Elsevier Ltd

parameters, in particular laser power, laser scan speed, and volumetric energy density, in the processing space that result in fully dense parts, it was demonstrated systematically that the composition of the printed parts could be precisely changed by controlling the evaporation of Ni. The flexibility of parameter selection to print defect-free NiTi SMAs and composition control by preferential evaporation of Ni opens the possibility to print functional NiTi SMA parts or devices without post-processing.

The flowchart in Figure 3.1 presents an overview of the experimental and computational methodologies used for $Ni_{51.1}Ti_{48.9}$ (at. %) and $Ni_{50.3}Ti_{49.7}$ (at. %) powder, included here to summarize the majority of the work performed in this chapter. Detailed information for each step shown in this figure can be found in the following section.

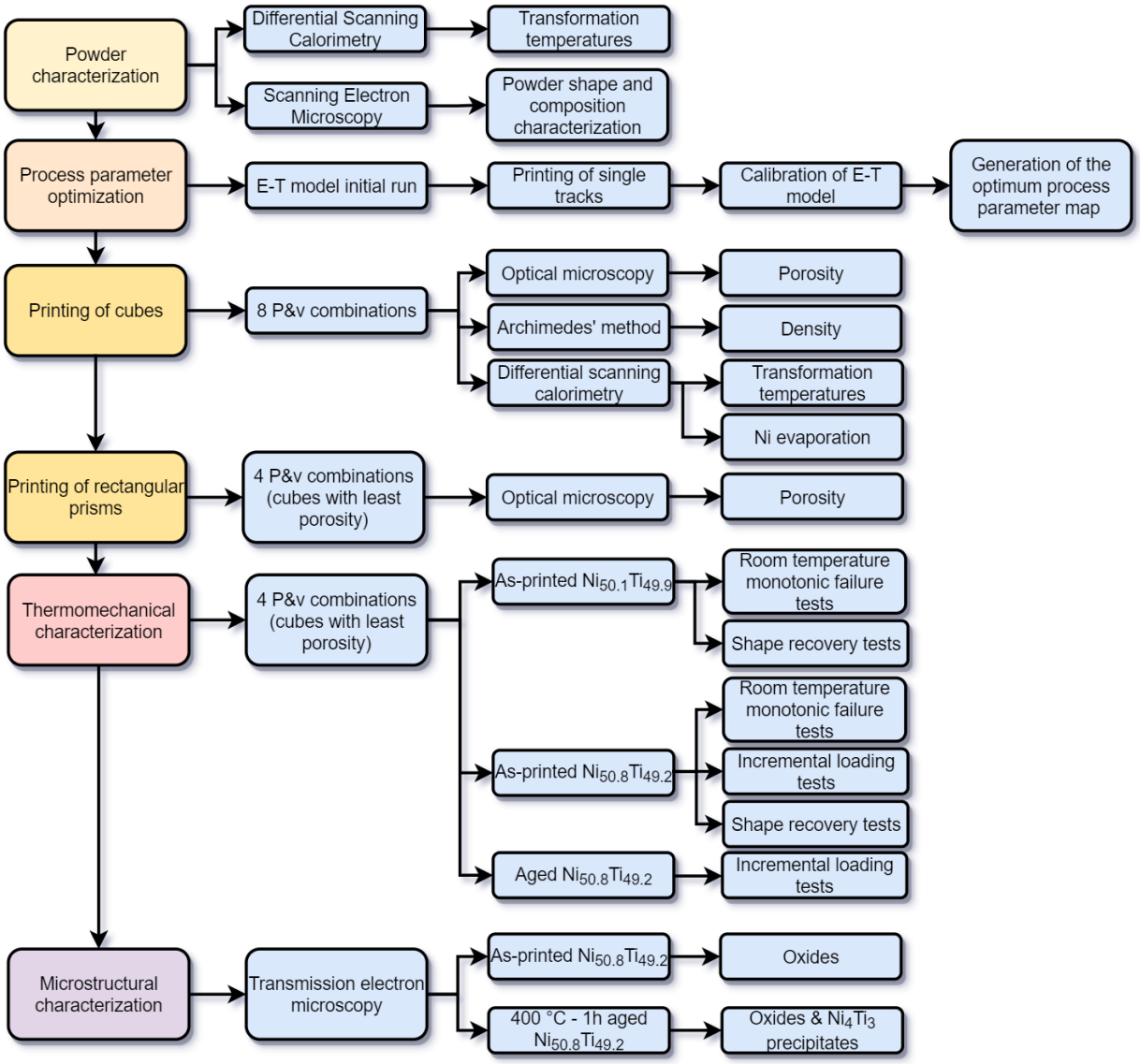

Figure 3.1 Summary of the experimental and computational methods utilized in the present study.

3.1 Materials and Experimental Methods

3.1.1 Powder Characterization

One batch of Ni-rich and one batch of near-equiatomic (named Ni-lean here) NiTi SMA powder (henceforth called NR for Ni-rich and NL for Ni-lean NiTi), both fabricated via the electrode induction-melting gas atomization (EIGA), was acquired from Carpenter Technology Corp. Powder compositions were measured as $Ni_{51.1}Ti_{48.9}$ (at. %) and $Ni_{50.3}Ti_{49.7}$ (at. %), respectively, through wavelength dispersive spectroscopy (WDS) with a Cameca SXFive electron microprobe analyzer (EPMA), by averaging the measurement results of 10 points taken from the cross-sections of random particles (Figures 3.2c and 3.2f). A FEI Quanta 600 FE scanning electron microscope (SEM) was used to investigate the morphology, size, and distribution of the powders. As shown in Figure 3.2, both powders have spherical particles with smooth surfaces devoid of satellite particles, and no hollow particles were observed. Powder size distribution was very similar in both powders with d_{10}, d_{50} and d_{80} values close to 16 μm, 29 μm and 40 μm, respectively, where d_{xx} denotes the cumulative size percentile of particles with diameters equal to the number provided.

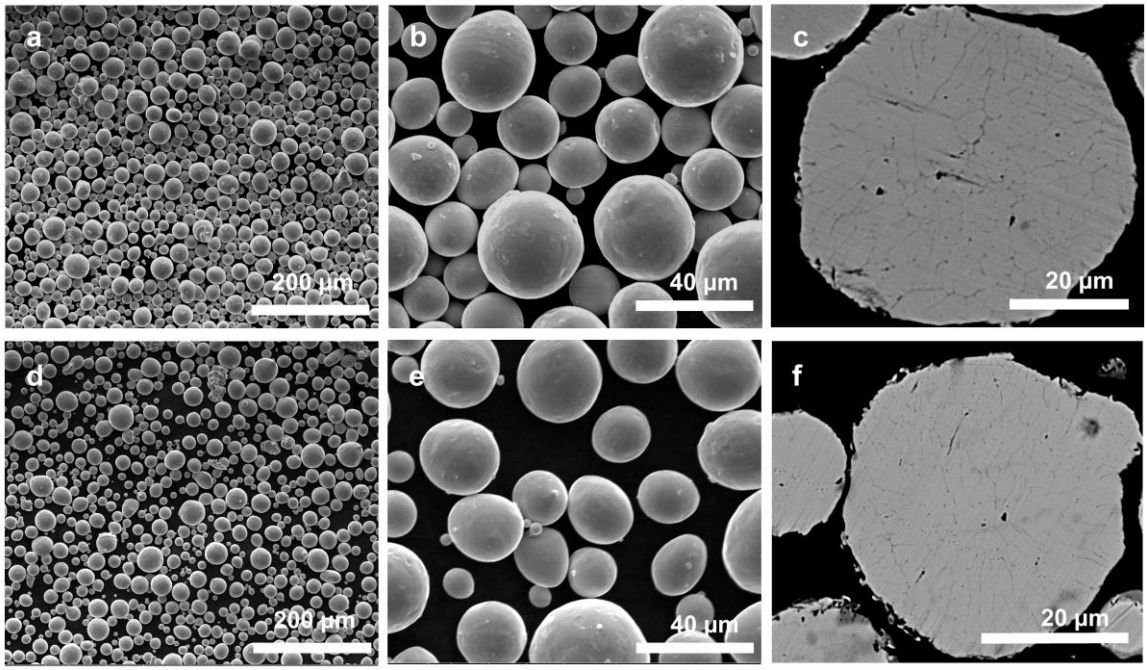

Figure 3.2 Scanning electron microscopy (SEM) and back-scattered electron (BSE) images of gas atomized NiTi powders. Low magnification images (a-b) and high magnification image (c) showing the powder size distribution and the cross-sections of random particles from Ni-rich (NR) powder, respectively. Similar images (d-f) for Ni-lean (NL) powder.

A TA Instruments Q2000 differential scanning calorimeter (DSC) was used to measure the transformation temperatures, i.e. martensite finish, M_f; martensite start, M_s; austenite start, A_s; austenite finish A_f, of the as-received powders. 2 thermal cycles were performed at a heating/cooling rate of 10 °C/min from -150 °C to 150 °C. Both as-received powders exhibit multiple transformation peaks at similar temperatures, although they have different nominal compositions (Figure 3.3a). This indicates that there might be compositional inhomogeneities within or among the particles in both powder types. In fact, the average Ni content as measured by WDS analyses from 10 random points on the NR and NL powder particles has standard deviation values of 0.4

and 0.5 %, respectively, which can significantly affect DSC transformation temperature results. In addition, a cellular structure with grain boundary segregation was observed for both powders, as seen in Figures 3.2c and 3.2f, supporting the presence of multiple transformation peaks seen in DSC results. To eliminate these inhomogeneities and better understand the average Ni content of each powder batch, powder samples were sealed in quartz tubes in a protective argon atmosphere and then solution heat-treated at 950 °C for 24 h followed by water quenching. It was observed that solution heat treatment of powders led to the homogenization of chemistry and the appearance of only single transformation peaks (Figure 3.3b). By using the tangent line intercept method according to ASTM F2004-17, M_s temperatures of the NR and NL powders were determined as -26.1 °C and 40.0 °C, respectively. Based on the study by Frenzel et al. [62] and the measured M_s temperatures of the solution heat-treated powders, the compositions of the NR and NL powders can be estimates as $Ni_{50.8}Ti_{49.2}$ (at.%) and $Ni_{50.1}Ti_{49.9}$ (at.%), respectively. These are slightly different from the WDS measured compositions of $Ni_{51.1}Ti_{48.9}$ (at. %) and $Ni_{50.3}Ti_{49.7}$ (at. %). Since WDS results are associated with errors that can reach 1% of the measured value (e.g., 0.5 % for 50 at.% Ni), the composition values predicted from the DSC results were used in the current study and believed to be more representative of the real composition.

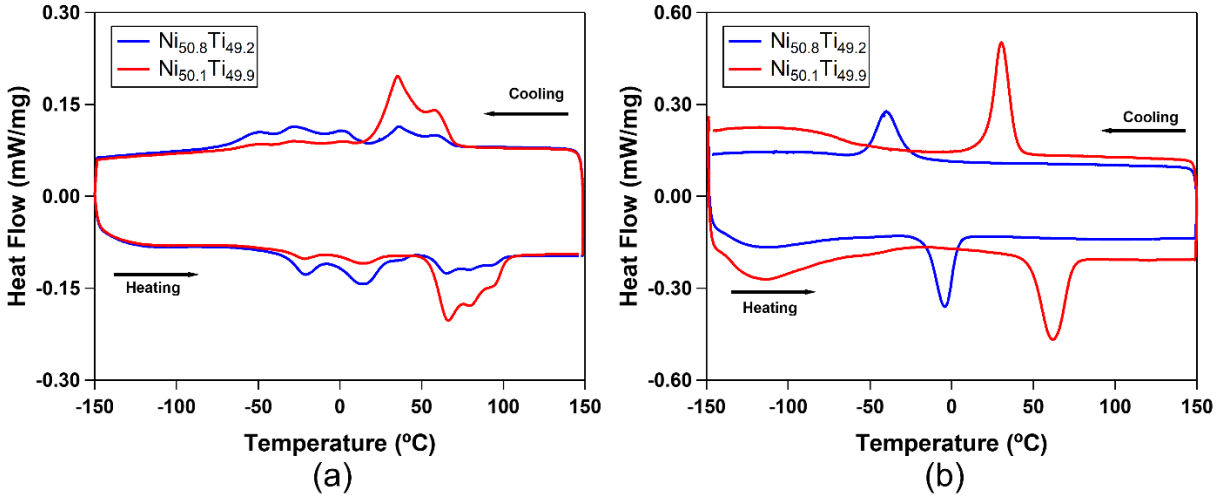

Figure 3.3 DSC results of NR ($Ni_{50.8}Ti_{49.2}$) and NL ($Ni_{50.1}Ti_{49.9}$) powders in (a) the as-received condition and (b) after solution heat treatment at 950 °C for 24h.

3.1.2 Optimization of Additive Manufacturing Process Parameters

Additive manufacturing of NiTi parts was performed using a 3D Systems ProX DMP 200 L-PBF system, which featured a fiber laser with a wavelength of 1040 nm and 80 μm beam size. The laser power and scanning speed have upper limits of 260 W (effective power delivered to the powder bed) and 2500 mm/s, respectively, in this AM system. Experiments were carried out under a protective atmosphere with an oxygen level lower than 500 ppm according to ASTM F2063-05 by flushing industrial-grade argon (99.99% purity) gas in the building chamber to minimize the oxidation and impurity pick-up.

3.1.3 Prediction of Melt Pool Dimensions and Temperature

Eagar-Tsai (E-T) model was employed to predict the geometry and temperature profile of

the melt pool during printing using material properties and processing parameters as inputs [63]. E-T model was originally developed to model the welding process, solving for the temperature profile and geometry of the weld pool created by a traveling distributed heat source on a semi-infinite plate. The model does not take into account convection heat transfer, the presence of metallic powder on the surface of the substrate, or vaporization-based processes such as keyhole mode melting, so when used for the simulation of AM processes, discrepancies between prediction and experimental results can be significant, especially at higher energy density levels [31]. The initial predictions of the E-T model were made based on the material properties of NiTi collected from literature and the processing parameters that were used in the printing process, i.e., laser power (P), scanning speed (v), and the size of the laser beam. The absorptivity value of NiTi was calculated as the weighted average of the absorptivity values of pure Ni and Ti powders for a Gaussian distribution with an average powder particle radius of 13.5 μm and 1 μm wavelength light (typical of AM systems) [64]. Thermal conductivity and specific heat capacity values of NiTi were calculated at a melting temperature of 1310 °C by extrapolating currently available data [65, 66]. A Bayesian statistical calibration described in [67] was subsequently employed to calibrate the E-T model with the experimental measurements of melt pool dimensions from the single-track experiments of both NR and NL powders. As the output of the E-T model, two sets of melt pool data were extracted: dimensions (width, length, and depth) and temperature profile. The reader is referred to the original paper for the mathematical equations defined in the E-T analytical model [63].

3.1.4 Single-track Experiments

The shape of the melt pool and its stability during printing greatly depend on processing parameters P and v. Therefore, knowledge of the melt pool geometry as a function of processing parameters is key for successfully printing 3D parts with minimal defects. Here we perform single track experiments to assess the melt pool dimensions and its continuity and to validate E-T model predictions as a function of process parameters. For printing single tracks of the NiTi SMA powders, an evenly spaced grid-based sampling strategy was chosen in the P-v space, with the total number of the tracks being 60. The minimum value of P was calculated using the E-T model as 25 W to melt a single layer of NiTi powder (using a layer thickness of 40 μm, which is the d_{80} value of the powder), assuming a nearly stationary laser beam with the scan speed of 0.0001 mm/s. The maximum value of P was taken as 260 W, which was the limit of the laser PBF (L-PBF) system used. Scanning speed varied between 50 mm/s and 2500 mm/s, where the latter is the maximum allowable speed of the L-PBF system, and the former is simply a very slow scanning speed that would result in very low build rates.

With the known thermophysical properties of NiTi, the printability map in the P-v space with boundary conditions can be established based on the E-T model, as shown in Figure 3.4. The description for each boundary line that defines a specific porosity formation mode (e.g., keyhole mode, lack of fusion (LOF), balling) or physical phenomena (e.g., melting) is also depicted in this figure. To ensure no keyholing porosity occurs in the printed parts, an aspect ratio of $D \geq W/2.2$ was used as an initial estimate following our experience with other materials [32, 68], where W stands for the melt pool width. $D \leq t$ was chosen as the LOF specification, where D is the depth of the

melt pool and t is the powder layer thickness. It is known that when the ratio of melt pool length (L) to W is high, the Plateau-Rayleigh instability [69] occurs, and the tracks are likely to break into droplets. An L/W ratio of 2 was chosen as the initial estimate for the balling defect criterion to generate the initial printability map. $T_{max} = T_{melt}$ boundary line corresponds to the condition that the maximum temperature at the melt pool (T_{max}) is equal to the melting temperature (T_{melt}) of the alloy.

Single tracks 10 mm long with 1 mm spacing between adjacent tracks were printed after a 40 μm thick layer of powder was applied on equiatomic NiTi substrates. NiTi substrates were used to minimize the effect of compositional gradients between the powder and substrate on the melt pool characteristics. Since single tracks have been reported to have an irregular shape at the start or the end of the tracks and they typically stabilize within 1 to 2 mm from the beginning of the track [70], top-view SEM images were taken from the middle of the tracks and width measurements were used to evaluate the continuity of the tracks such that the defects generated from LOF or balling region can be classified. Single-track cross-section samples were cut from the NiTi substrates using wire-EDM and were prepared using mechanical polishing with successively fine paper up to 1200 grit, followed by a final polishing step with colloidal silica solution. The samples were then etched with 1 part HF, 3 parts HNO_3, and 10 parts distilled water at room temperature to reveal the melt pool shapes. Optical microscopy (OM) was carried out using a Keyence VH- X digital microscope equipped with a VH-Z100 wide-range zoom lens, and the OM images were taken from each cross-section to measure melt pool depth.

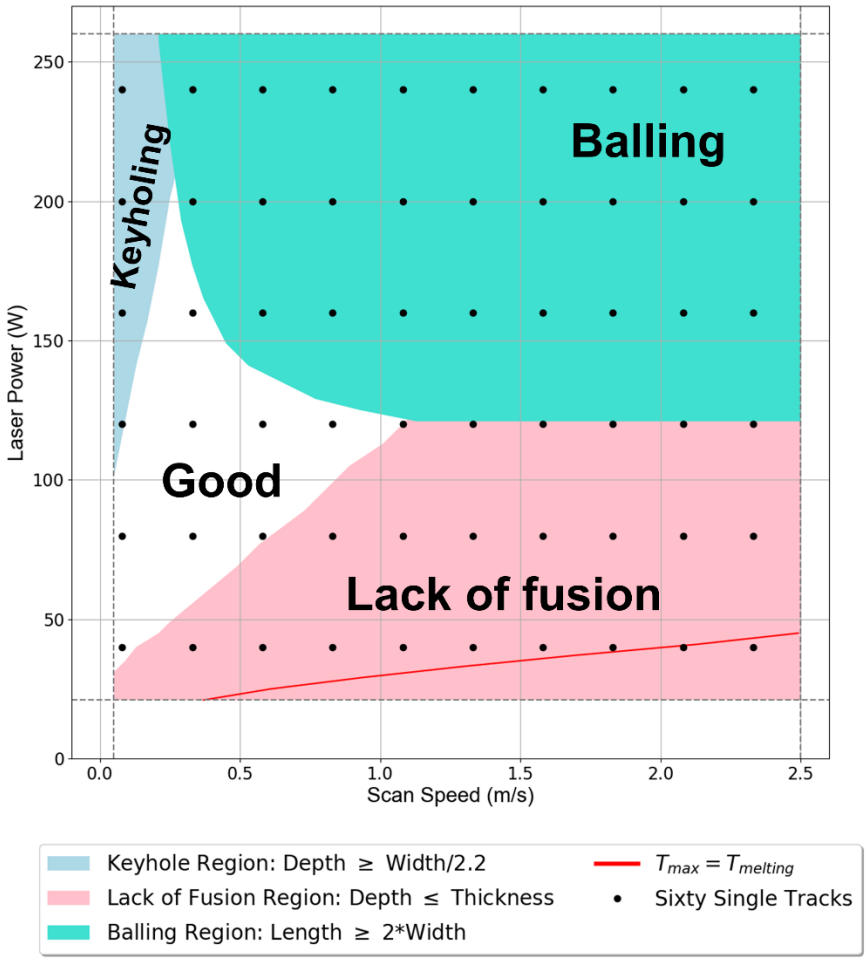

Figure 3.4 The initial AM process parameter map for NiTi SMAs predicted by the uncalibrated Eagar-Tsai (E-T) model with different defect criteria. Black dots indicate the process parameters (laser powder, *P* and scanning speed, *v*) selected for the single-track experiments.

3.1.5 Printing of Bulk Samples

Once the initial printability map predicted by the E-T model is calibrated (details of which will be introduced in the results section below) and the boundary conditions that will avoid defect formation mechanisms are refined, 8 sets of processing parameters

were selected from the good region to print 10 × 10 × 10 mm cubes from both NR and NL powders. The best 4 cases from these 8 sets, i.e., cases with the least porosity, were selected to print the 30 × 10 ×10 mm^3 rectangular prisms to be able to extract dog-bone shaped specimens for tensile testing. All prints were fabricated using a bi-directional scanning strategy with a 45° angle to the edge of the prints and a 90° rotation angle between the layers. It should be noted that this scanning strategy has been reported to generate large thermal gradients inside the printed parts [71] and therefore may cause warping problems in NiTi as a result of residual stresses. A few studies have reported the advantage of utilizing more complex scanning strategies during the fabrication of NiTi and obtained better mechanical properties such as increased ductility [25, 34, 72].

3.1.6 Density and Porosity Measurements

Archimedes method, following ASTM B962-17 standard, was employed to measure the density of the printed parts. A quantitative density comparison of the printed parts was also conducted by the analysis of optical microscopy images. For the image analysis, the cross-section samples (perpendicular and parallel to the build direction) cut from the cubes and rectangular prisms were prepared using mechanical grinding up to 1200 grit, and optical microscopy images were taken at 100X magnification at the locations that included the highest volume fraction of pores inspected visually. For the cross sections of cube prints perpendicular to the building direction, it was noticed that the porosity area density and morphology varied significantly as a function of build height, thus the images of the surfaces parallel to the building direction were taken into account. Images were processed using ImageJ software to quantify the porosity in the as-

printed samples.

3.1.7 Thermomechanical Characterization

Dog-bone shaped tensile specimens with gage section dimensions of 8 mm × 3 mm × 1 mm were cut from the printed rectangular prisms, with their width and length dimensions oriented perpendicular to the building direction. A servo-hydraulic MTS test frame with heating and cooling capability was used to perform the tests. An MTS high-temperature extensometer was attached to the gage section of the samples to monitor the tensile strain. Three kinds of thermomechanical tests were performed:

Monotonic tensile failure tests at a nominal strain rate of 5×10^{-4} s^{-1} were performed to verify the room temperature ductility of the as-printed parts.

Shape recovery tests were performed to characterize the shape memory effect as a function of applied strain. In these tests, the samples were loaded at M_f - 50 °C by increments of 2 % strain, unloaded to 0 MPa, and then heated above A_f + 50 °C to quantify the recovered and irrecoverable deformation levels. Loading at increasing strain levels continued until the failure of the sample.

Incremental loading tests were performed to characterize the superelasticity as a function of deformation. Samples were loaded with 0.5% tensile strain increments up to 5% applied strain, and 1% increments beyond 5% applied strain at A_f + 5 °C and unloaded, recording the superelastic strain at the end of the cycle. Loading continued until failure occurred.

While these tests were performed on as-printed samples, additional incremental loading tests were performed on samples fabricated from NR ($Ni_{50.8}Ti_{49.2}$) powder that

underwent post-printing annealing heat treatment at 400 °C for 1h followed by quenching to room temperature. The primary purpose of these tests was to see if superelasticity could be improved through the formation of coherent Ni_4Ti_3 precipitates.

3.1.8 Microstructural Characterization

Transmission electron microscopy (TEM) experiments were conducted on selected as-fabricated and aged samples fabricated from NR powder to observe any possible oxide inclusions and precipitate formation that might affect the mechanical and shape memory properties of the printed parts. A Titan Themis^3 300 scanning transmission electron microscope (STEM) providing high-resolution imaging was used at an accelerating voltage of 300kV. Energy-dispersive X-ray spectroscopy (EDXS) was also used to detect the chemical composition of the precipitates. TEM foils were prepared by initially mechanical grinding of slices wire EDM-cut from rectangular prisms down to 50 µm, followed by punching of foils with a diameter of 3 mm. Foils were finally twin-jet electropolished using 20 vol. % HNO_3 in a methanol solution at -20ºC.

3.2 Single Track Analysis

The quality of the single-tracks can be classified as either good or defective with the keyholing, balling, and LOF defects specified based on the track morphology and melt pool dimensions. Figure 3.5 illustrates the top-view SEM images and the corresponding cross-section OM images of single tracks printed using the NR powder, describing how different defects were classified.

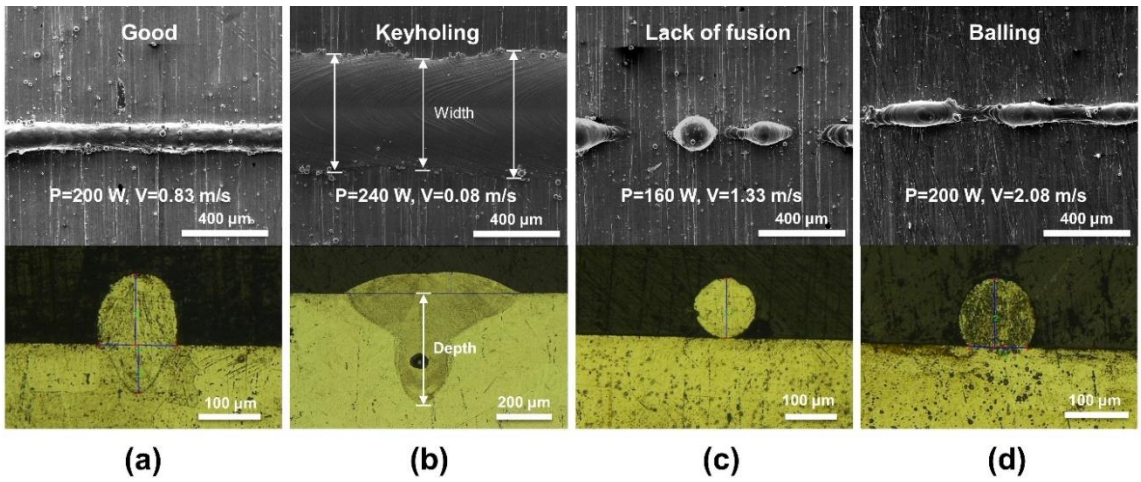

Figure 3.5 Top-view SEM images (top row) and optical micrographs of the cross-sections of single-tracks (bottom row) fabricated from NR powder classified as (a) good quality and with (b) keyholing, (c) LOF, and (d) balling defects. Figure (b) also includes a schematic of how melt pool widths (*W*) and depths (*D*) are measured. W is calculated as the average of three measurements.

At relatively high linear energy density (LED, calculated as P/v) values, heat transfer mode inside the melt pool changes from conduction to the so-called keyholing mode with increased recoil pressure and melt pool penetration as a result of excessive evaporation. Although this defect cannot be observed in top-view SEM images of the single tracks, it can be seen in the optical micrographs of the cross-sections and is often characterized by porosities resulting from entrapped metallic vapor during printing. The single tracks which show keyhole porosity generally exhibited larger melt pool dimensions, especially the depth, due to the excessive energy input (Figure 5b).

In contrast, LOF is encountered in tracks printed at low LED levels. LOF results in either no tracks or large gaps of discontinuity on the tracks without leaving evidence of melting of the substrate (Figure 5c). The energy input is not sufficient to melt the

powder layer completely. Unlike keyholing porosity, LOF defects generally follow a geometrical pattern defined by the scanning strategy [73]. The pores are usually sharp-edged and thus more likely to have a more pronounced effect on the ductility of 3D printed parts. To ensure full interlayer fusion and enough remelting of the sub-layer to promote the bonding between successive layers, uniform or continuous single tracks with melt pool depth smaller than the layer thickness (40 μm) were also classified as LOF.

Balling is a phenomenon caused by melt pool instabilities and is observed when both *P* and *v* are high. The continuity of the single-tracks is compromised when balling occurs during fabrication, and the printed parts will typically exhibit poor surface roughness, porosity, and even delamination [74]. Morphologically, the balling tracks are not uniform in width and sometimes show discontinuities, but unlike the LOF defect, the track is mostly present with the laser penetrating the substrate (Figure 3.5d).

Tracks that can be classified as good are the uniform tracks with a depth larger than the layer thickness, and the corresponding LED is between those for tracks that exhibited keyholing and LOF. For good tracks, it is observed that *P* and *v* values are in the intermediate range. Based on single track observations, it can be assumed that keyholing and balling will result in unwanted porosity within the builds during layer by layer printing, and LOF will leave unmolten powder, hence, pores.

Since all three aforementioned defect-generation schemes lead to detrimental defects in the builds and therefore need to be avoided, it is important to validate their respective boundaries on the printability map to obtain the precise good printable region,

i.e., *P*-*v* range for the L-PBF processing of NiTi. As shown previously in Figure 3.4, the regions on the printability map can be defined based on the predictions of the melt pool dimensions from the uncalibrated E-T model. A similar method has previously been adopted in the work of Haberland et al. [75] with success for L-PBF of NiTi, but only the single tracks' width was considered in that study. From the SEM and OM images of single tracks illustrated in Figure 3.5, the melt pool width (*W*) and depth (*D*) of 60 single tracks were measured and plotted as a function of LED for both NR and NL powders (Figure 3.6). It is observed that both *W* and *D* increase with increasing LED from 0 to 500 J/m. The sudden drop of the depth values at LED values higher than 500 J/m is due to the heat loss from the Ni evaporation due to the abundant energy input and the poor thermal conductivity of the trapped vapor. Similar depth drops have also been observed in other materials due to the transition to the keyholing mode [32, 68]. Figure 3.6 shows that the melt pool dimensions of NR and NL powders are very similar. The smaller difference can be explained by the experimental error, the repeatability of the printing, and the small difference of the material properties from the compositional difference. Compared to other studies that employed single tracks for optimizing processing parameters [70, 75], this study systematically investigated the single tracks over a much wider *P*-*v* space to explore the full potential of fabricating NiTi through L-PBF.

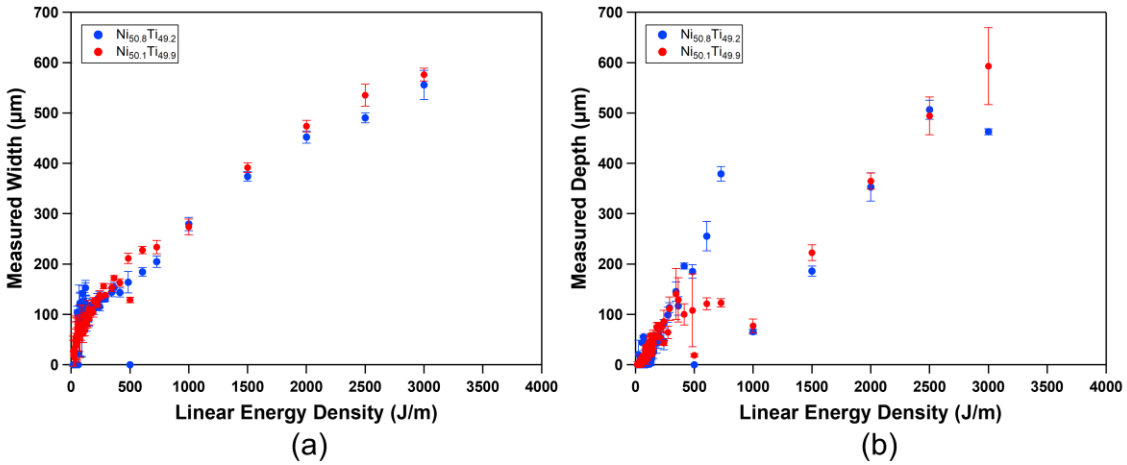

Figure 3.6 (a) Melt pool width (average of 6 measurements) of 60 single tracks as measured from the top-view SEM images, and (b) melt pool depth (average of 3 measurements)as measured from the cross-section optical microscopy images, as a function of linear energy density for the two NiTi SMA powder compositions used in the present study.

3.3 Generation of the Calibrated Printability Map

After being calibrated with the experimentally measured melt pool dimensions from the single-track experiments using a Bayesian statistical calibration [32, 68] the E-T model predicted the melt pool dimensions more accurately for both NR and NL powders as a function of processing parameters. As shown in Figure 3.7, the predictions match well with the experimental data. The calibrated E-T model was then used to generate the two regions in the *P-v* space for keyholing and LOF defects using specific criteria for each defect mode. The balling region was constructed using a classification method based on the single-track observations (Figure 3.8). The region bounded by these three defect regions is identified as the good region for the *P-v* combination that should prevent these three defect types.

In the calibrated printability maps, the keyholing region was extended to be more conservative, including *W/D* ratios from 2.0 down to 1.2. The balling area was constructed using a support vector machine (SVM) classifier, similar to what was reported in [32]. The SVM classifier with a polynomial kernel that matches the best of the characterized balling tracks was used. To ensure full fusion between tracks and layers, the maximum value of hatch spacing, *h*, was then calculated using the melt pool depth and width and a geometric criterion that assumes a parabolic shape of the melt pool as defined in [32]. Based on the melt pool dimensions predicted by the calibrated E-T model, the maximum value of *h* can be used as guidance to ensure sufficient overlapping of consecutive melt pools for different *P* and *v* combinations. With the addition of maximum *h* contours, the finalized printability maps for NR and NL powders are plotted in Figure 3.8.

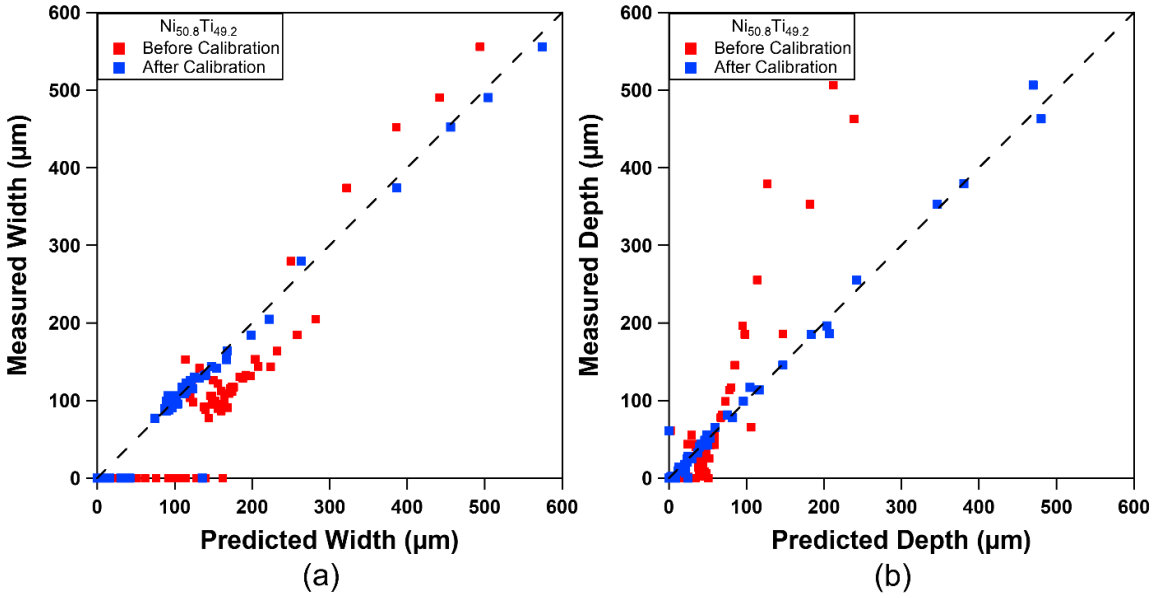

Figure 3.7 Measured average (a) width and (b) depth vs. predicted (a) width and (b) depth values for single tracks of NR powder, predicted using the calibrated E-T model.

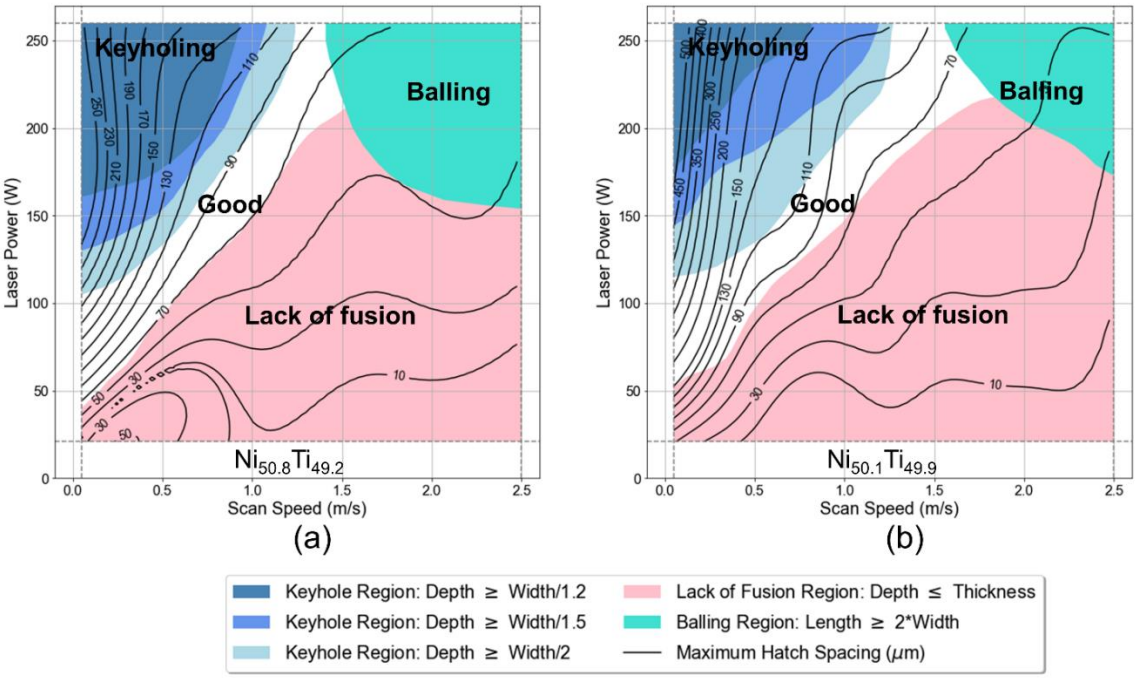

Figure 3.8 Process parameter map with different keyholing criteria ($W/D \leq 1.2$, 1.5, 2.0) and a LOF criterion ($D \leq t$) predicted using the calibrated E-T model for (a) NR

($Ni_{50.8}Ti_{49.2}$) and (b) NL ($Ni_{50.1}Ti_{49.9}$) powders. Contours indicate the maximum value of hatch spacing, *h*, that will not cause LOF defects.

By selecting processing parameters following the maximum hatch spacing criteria, the pores introduced by the unmolten powder should be avoided. Selecting processing parameters within the good region can prevent the porosity generated by trapped gas (keyholing), not melting the powder layer completely (LOF), and rough surface (balling). It should be noted here that during the printing of layers for the construction of selected cubes (see Section 3.3), occasional spatters were observed ejecting from the molten pool by the pressure of the metallic vapor, and it was also noticed that projection of the spattered particles might travel long enough to reach the neighboring building part. Nevertheless, the defects caused by the spatter cannot be predicted using the current framework. Capturing real-time images during printing may help identify the process parameters that generate the spatter. This can be performed with test prints of a few layers in future studies. Similarly, although the keyholing criterion has been extended in the printability map down to $W/D = 1.2$, it should be noted that in the good region close to the keyholing boundary, keyholing porosity may still be observed due to the accumulated heat during the printing process, causing the selected *P-v* combination to turn into one that causes keyholing with less energy input. Therefore, the appropriate keyholing criterion should be fine-tuned for each material based on the bulk sample prints, which will be discussed in the next section.

3.4 Fabrication and Analysis of Bulk Cube Prints

From the calibrated printability maps in Figure 3.8, eight sets of processing parameters were selected from the good regions of the printability maps of NR and NL powders to print 10 × 10 × 10 mm^3 cubes. Hatch spacing values were kept slightly smaller than the calculated maximum hatch spacing values to further minimize porosity formation by ensuring sufficient overlap between successive tracks (Table 3.1).

Table 3.1 Processing parameters for printing 10 × 10 × 10 mm^3 cubes and corresponding density values determined using the Archimedes' method, the area fraction of porosity observed, and transformation temperatures. *P*: Laser power, *v*: laser speed, *h*: hatch spacing.

Parameter Set #	**Processing parameters**				**Archimedes density (%)**		**Porosity (%) (from the cross-sectional images)**		**Transformation Temperatures (°C)**			
									$Ni_{50.8}Ti_{49.2}$		$Ni_{50.1}Ti_{49.9}$	
	v **(m/s)**	***P*** **(W)**	***h*** **(μm)**	VED (J/mm^3)	$Ni_{50.8}Ti_{49.2}$	$Ni_{50.1}Ti_{49.9}$	$Ni_{50.8}Ti_{49.2}$	$Ni_{50.1}Ti_{49.9}$	M_s	A_f	M_s	A_f
1	0.330	80	80	75.76	99.07	98.25	1.27	0.96	26.0	54.7	58.7	89.9
2	0.830	160	80	60.24	100.00	99.25	0.08	0.19	1.9	25.6	44.8	76.7
3	1.080	160	70	52.91	99.86	97.49	0.02	0.01	2.2	27.8	45.7	77.2
4	1.330	240	80	56.39	98.58	99.33	0.03	0.02	1.6	29.1	46.6	77.3
5	0.330	120	130	69.93	94.28	96.13	2.84	2.20	17.8	47.2	55.0	89.4
6	0.580	160	110	62.70	96.97	97.04	1.50	1.22	1.6	20.7	47.1	78.6
7	0.830	200	100	60.24	98.42	99.26	0.19	0.17	-3.7	23.1	46.2	76.3
8	1.080	200	80	57.87	98.44	100.00	0.00	0.00	-2.8	24.4	45.6	77.5

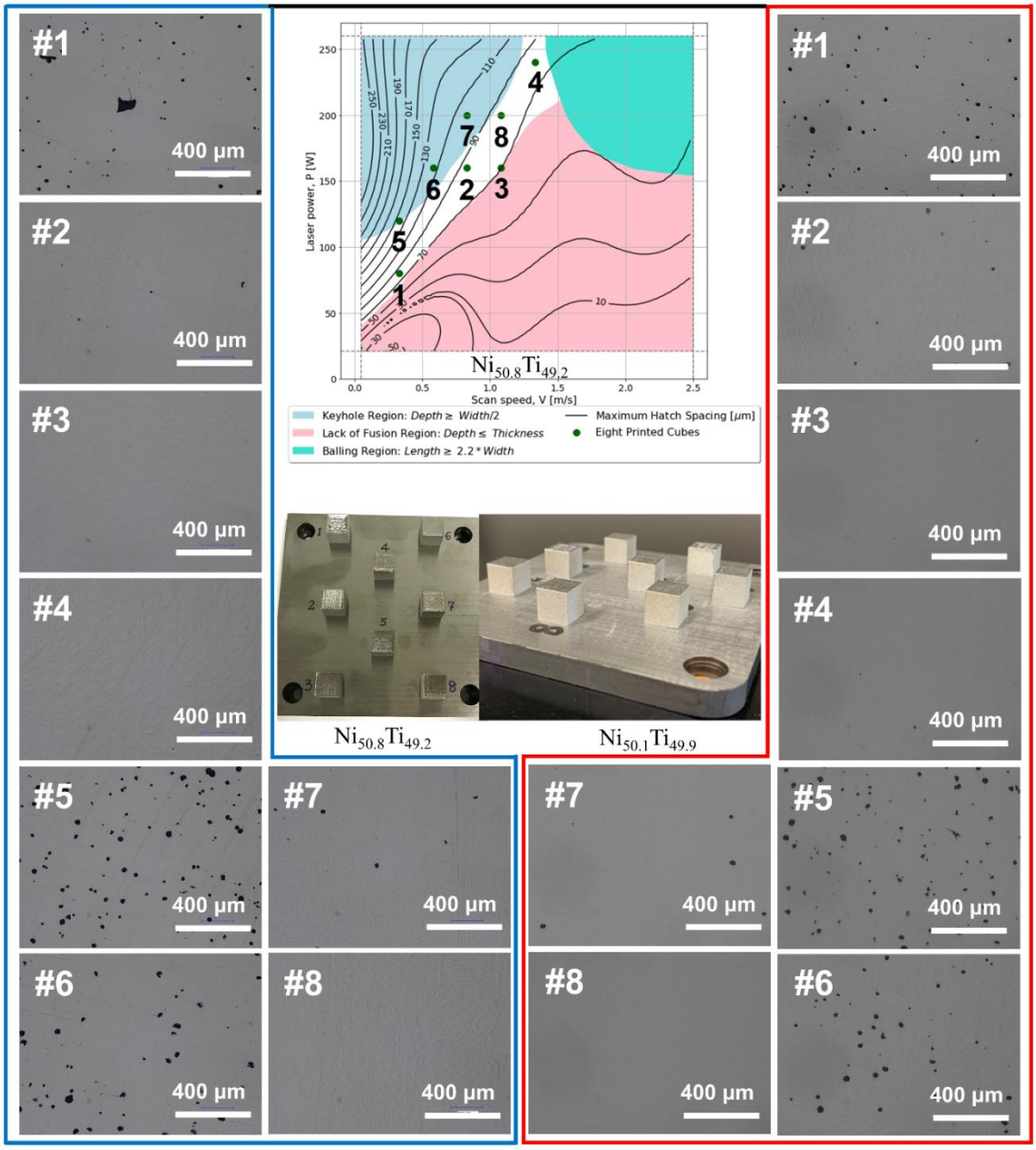

Figure 3.9 (Top-middle) Finalized process parameter map for the NR ($Ni_{50.8}Ti_{49.2}$) powder illustrating the selection of processing parameters for the cubes marked with dots. The same processing parameters were used for printing cubes with the NL ($Ni_{50.1}Ti_{49.9}$) powder. The printability map for the NL ($Ni_{50.1}Ti_{49.9}$) powder is not shown here but can be seen in Figure 3.8b. **(Middle)** Cubes printed from both powders on NiTi substrates. Optical micrographs of the polished cross sections (parallel to the building direction) of the cubes printed using NR powder **(Left two columns)** and NL powder

(Right two columns), displaying the porosity. The reader is referred to Table 3.1 for the processing parameters used during printing.

Based on Archimedes' density measurements, all cubes except Cubes #5 and #6 exhibited high-density values (>98%) relative to the theoretical value (from the bulk samples used to make the powder). As seen in the optical microscopy images of cross-sections parallel to the build direction (Figure 3.9), Cubes #2, #3, #4, and #8 of NR powder have almost no porosity, and those parameter sets were used to print larger rectangular prisms to be able to extract dog bone specimens for tensile testing. The same sets of process parameters also yielded the least porosity levels in parts built from NL powder as observed from optical microscopy images. In addition, based on these porosity results, the keyholing criterion of $W/D = 2.0$ was concluded to be the most conservative keyholing boundary condition for these compositions.

Cubes #1 printed using both NR and NL powders showed sharp and irregular shaped pores, which might be an indication of the LOF defect due to the relatively low energy input during the printing since the P and v combination for Cube #1 is near the LOF region in the printability map. Smaller and spherical pores were observed in Cubes #5 and #6, which are likely to be caused by the trapped vapor due to heat accumulation at relatively high energy densities. These two parameter sets are close to the keyholing region on the printability map. Larger prints may experience higher temperatures overall due to heat accumulation during printing as compared with the single-track experiments printed on a cold substrate. Other than these 3 parameter sets that resulted in parts with relatively higher defect density, the remaining 5 parameter sets were successful in

building near porosity-free cubes from both NR and NL powders. Based on literature data, volumetric energy density (VED, which is equal to P/vht) values smaller than 200 J/mm^3 are typically utilized to print NiTi parts with relative densities above 99% [75, 76]. VED values used to print the cubes, and rectangular prism in the present study are between 50 to 200 J/mm^3.

Figure 3.10 illustrates the unique microstructure of AM NiTi SMAs, with chessboard-like grain structure perpendicular (Figure 3.10a) and columnar grains parallel to the building direction (Figure 3.10b). Similar microstructures in L-PBF NiTi have already been reported [77]. The width of the square grains in Figure 3.10b is close to the hatch spacing value used during printing, which is 80 µm for Cube #2 printed using the NR powder.

Figure 3.11 shows the DSC thermograms of the samples extracted from the middle of the cubes printed using the NR and NL powders in as-printed and in the solution heat-treated conditions. Figure 3.11 also presents the DSC thermograms of the corresponding starting powders in solution heat-treated condition (at 950 °C for 24h). The VED values for each printing condition was also included in the figure for each DSC response. Solid lines indicate the responses of the as-printed samples; dashed lines represent the behavior of the samples that were solution heat-treated at 800 °C for 1h. The solution heat treatment was performed to dissolve any precipitates, or annihilate the dislocations, which may have formed during printing, and relieve internal stresses such that the effect of compositional differences on the martensitic transformation characteristics can be deconvoluted among the printed cubes. At first glance, single

transformation peaks are observed for all as-printed and solution heat-treated samples during both forward and reverse transformation, indicating a relatively homogeneous microstructure without discrete compositional differences or extensive precipitation. It is well known that in Ni-rich NiTi, local inhomogeneities in matrix composition and the precipitation of Ni_4Ti_3 type coherent precipitates lead to the appearance of multi-stage transformations from B2 to B19' as well as to the appearance of the R-phase [78, 79]. For the as-printed cubes fabricated from NR powder, the highest M_s temperature was recorded in Cube #1 as 26.0 °C, while the lowest was recorded in Cube #7 as -3.7 °C.

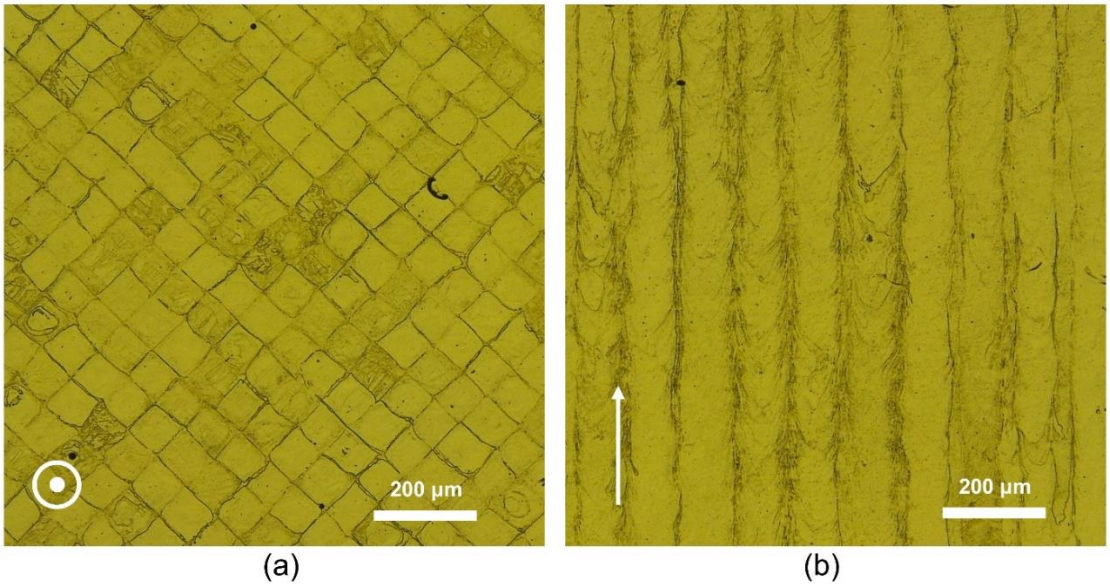

Figure 3.10 Optical microscopy images of the cross-sections (a) perpendicular and (b) parallel to the beam or building direction. Images belong to Cube #2 printed using the NR powder.

A trend of increasing M_s and A_f temperatures with increasing VED was observed for both as-fabricated and the solution heat-treated samples fabricated from the NR powder (Figure 3.11 a, Figures 3.12a and b). This trend can be primarily attributed to

different Ni evaporation levels at different energy inputs during the printing process due to the higher vapor pressure of Ni compared to Ti. It should be noted that to better reveal this trend, thirteen additional cubes (Table 3.2), with process parameters different than those for the eight cubes in Table 3.1, were printed using new processing parameters from the good region in the printability map (Figure 3.8), corresponding to VED levels ranging from 80 to 235 J/mm^3. Considering the fact that NR and NL powders have similar Ni content within 1 at. % difference, the percentage of evaporated Ni from both powders is expected to be similar when the same processing parameters are used.

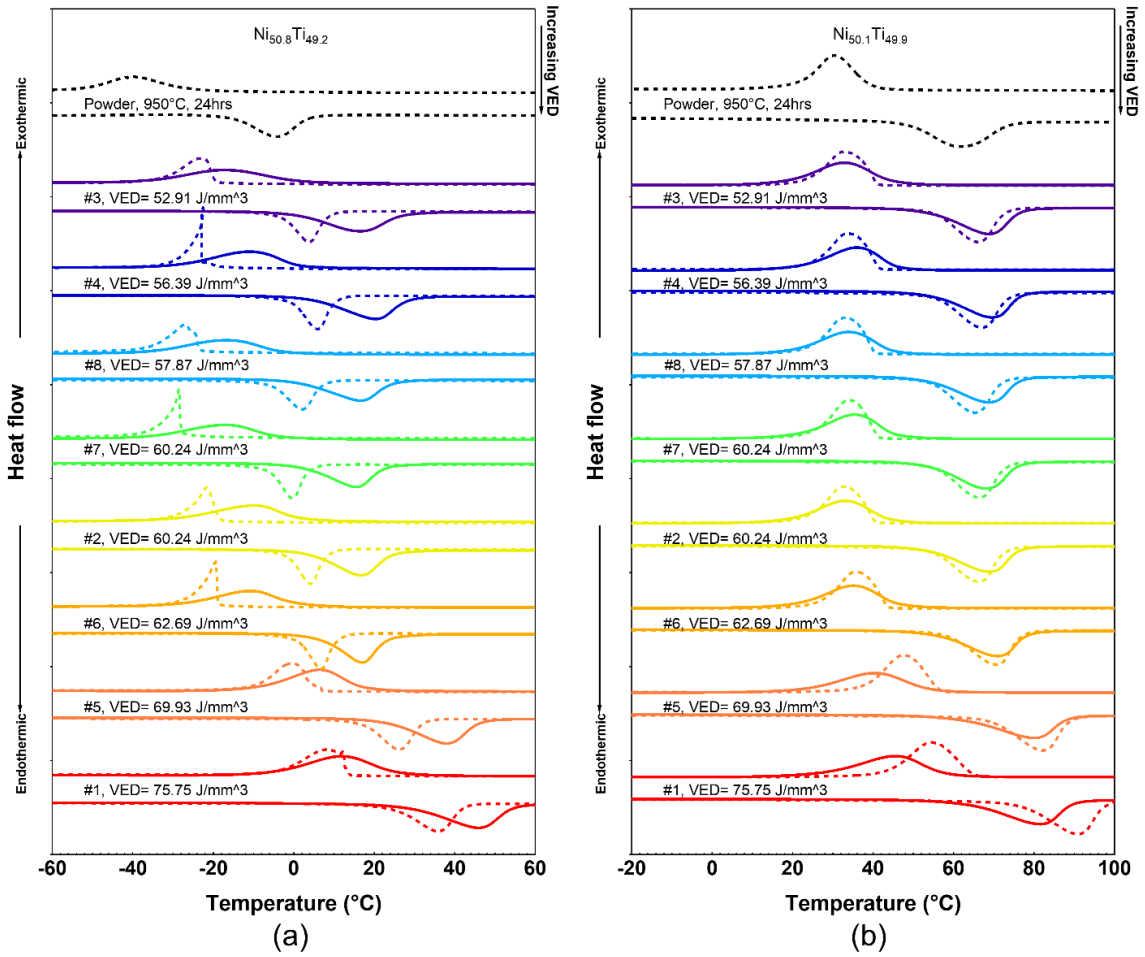

Figure 3.11 DSC thermograms of the NR and NL powders solution heat-treated at 950°C for 24h, as fabricated and solution heat-treated (at 800°C for 1h) cube prints of (a) $Ni_{50.8}Ti_{49.2}$ (NR) and (b) $Ni_{50.1}Ti_{49.9}$ (NL), using the parameters listed in Table 3.1. Solid lines: As-printed samples, Dashed lines: Solution heat-treated samples.

It can also be seen in Figure 3.11 that the transformation peaks of as-fabricated samples are broader compared to those of the solution heat-treated materials, indicating a higher energy barrier against martensitic transformation, possibly as a result of a microstructure with relatively higher defect density due to the rapid cooling during L-PBF. The decrease in the M_s and A_f temperatures of the as-fabricated NR samples (with

only minor changes in M_f and A_s temperatures) after solution heat treatment could either be attributed to the relaxation of oriented internal stress fields that may result from the directional solidification inherent to the layer-by-layer manufacturing process [16] or the dissolution of Ni-rich precipitates that may form during the printing process. As it will be shown in Section 3.6, TEM analysis of the samples cut from the as-printed Case #8 rectangular block did not reveal the existence of Ni_4Ti_3 precipitates in the foils investigated. Despite this may not mean that the precipitates do not exist since TEM is a local method, their volume fraction must be very low, and they must only be forming locally if they exist at all. Based on the assumption that M_s temperature is controlled by matrix Ni content only and its change as a function of Ni content is expressed as in [62], the volume fraction of the Ni_4Ti_3 precipitates that would dissolve in the matrix after solution heat treatment should be approximately 2.75% to achieve a 21°C (for Case #8) shift in the M_s temperature. Such volume fraction levels were not observed in the TEM images of the as-fabricated sample. Therefore, the dissolution of Ni rich precipitates cannot be the only reason for the reduction in the M_s and A_f temperatures after solution heat treatment. The relaxation of oriented internal stress fields must also play a notable role.

Table 3.2 Processing parameters for printing additional 13 cubes of 10 × 10 × 10 mm^3 size in the good printability region (Figure 3.8) for the NR powder. *P*: Laser power, *v*: laser speed, *h*: hatch spacing.

Parameters Set #	Processing parameters				As-fabricated		Solution Heat Treated	
	***P* (W)**	***v* (m/s)**	***h* (μm)**	**VED(J/mm^3)**	**M_s (°C)**	**A_f (°C)**	**M_s (°C)**	**A_f (°C)**
9	65	0.297	100	54.7	29.4	54.0	11.2	41.4
10	96	0.297	100	80.8	27.4	54.0	15.1	44.4
11	65	0.200	100	81.3	36.0	65.1	27.4	57.3
12	96	0.350	80	85.7	27.9	57.7	21.9	50.3
13	60	0.160	100	93.8	45.8	74.9	38.6	70.2
14	96	0.250	100	96.0	30.3	63.8	21.0	51.2
15	96	0.297	80	101.0	24.4	46.6	21.4	51.1
16	96	0.200	100	120.0	40.0	72.4	32.6	62.6
17	60	0.120	100	125.0	57.0	85.3	54.4	86.5
18	72	0.120	120	125.0	52.8	82.5	47.6	79.4
19	60	0.080	120	156.3	64.1	93.4	66.8	99.8
20	65	0.080	120	169.3	63.7	95.1	70.0	102.8
21	60	0.080	80	234.4	65.7	96.1	70.8	106.3

The DSC results of the samples printed using the NL powder did not show much variation in transformation temperatures as a function of processing parameters (Table 3.1 and Figures 3.11b, 12a, and 12b) due to the relatively lower starting Ni concentration of the powder (i.e., 50.1 at.%). Consequently, the transformation temperatures do not increase even if Ni might be evaporating during the laser melting process since they are more or less independent of the matrix Ni content and stay constant for Ni concentrations below 50.0 at. %.

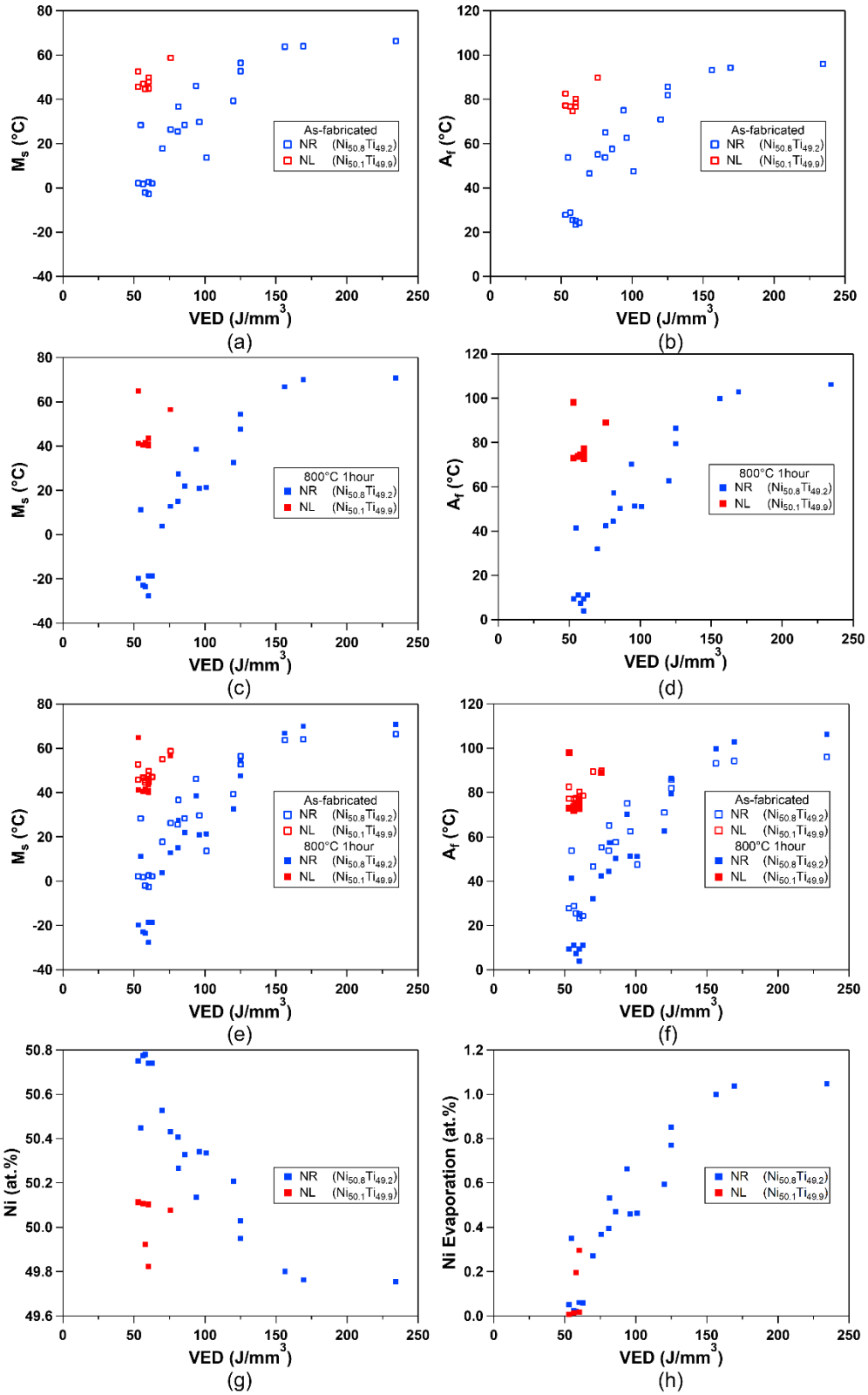
Ms (°C)
VED (J/mm3)
(a)
As-fabricated
NR (Ni50.8Ti49.2)
NL (Ni50.1Ti49.9)
Af (°C)
VED (J/mm3)
(b)
As-fabricated
NR (Ni50.8Ti49.2)
NL (Ni50.1Ti49.9)
Ms (°C)
VED (J/mm3)
(c)
800°C 1hour
NR (Ni50.8Ti49.2)
NL (Ni50.1Ti49.9)
Af (°C)
VED (J/mm3)
(d)
800°C 1hour
NR (Ni50.8Ti49.2)
NL (Ni50.1Ti49.9)
Ms (°C)
VED (J/mm3)
(e)
As-fabricated
NR (Ni50.8Ti49.2)
NL (Ni50.1Ti49.9)
800°C 1hour
NR (Ni50.8Ti49.2)
NL (Ni50.1Ti49.9)
Af (°C)
VED (J/mm3)
(f)
As-fabricated
NR (Ni50.8Ti49.2)
NL (Ni50.1Ti49.9)
800°C 1hour
NR (Ni50.8Ti49.2)
NL (Ni50.1Ti49.9)
Ni (at.%)
VED (J/mm3)
(g)
NR (Ni50.8Ti49.2)
NL (Ni50.1Ti49.9)
Ni Evaporation (at.%)
VED (J/mm3)
(h)
NR (Ni50.8Ti49.2)
NL (Ni50.1Ti49.9)

Figure 3.12 Influence of the volumetric energy density (VED) on the (a), (c), (e) M_s temperature, (b), (d), (f) A_f temperature, (g) the calculated Ni (at. %) content and (h) Ni evaporation (at. %) of the NiTi cubes printed using $Ni_{50.8}Ti_{49.2}$ and $Ni_{50.1}Ti_{49.9}$ powders.

It has also been noticed the cubes printed using the NR powder had warping and delamination problems at the bottom surfaces, which made contact with the NiTi substrate, while the cubes printed using the NL powder did not have this issue. It is hypothesized that in the cubes printed from the NL powder, the material may completely transform to martensite at the end of each layer's printing. The martensitic transformation and the reorientation of martensite variants can partly relax the internal stress. However, due to the presence of austenite at room temperature in parts built from the NR powder, the internal stresses are not relaxed and reached higher values with increasing build height, causing warping and delamination. The relatively larger internal stresses in cubes printed from the NR powder are also deemed responsible for the larger shifts in the transformation temperatures after solution heat treatment (Figure 3.11).

Interestingly, two cubes printed from the NL powder (Cases #1 and #5 in Figure 3.11b, with the highest VED parameters) and three cubes printed from the NR powder with VED larger than 150 J/mm^3 (Figure 3.12e) displayed higher transformation temperatures in solution heat-treated condition. The reason for this trend is not entirely known. However, it might be related to the formation of randomly distributed dislocation structures in the as-printed conditions (as opposed to oriented dislocation structures leading to oriented internal stresses at lower VEDs). Randomly distributed

dislocations suppress martensitic transformation temperatures. The annihilation of these dislocations upon solution heat treatment increases the transformation temperatures.

The trends seen in the evolution of M_s and A_f transformation temperatures of the cubes printed from the NR powder, as a function of the VED level (Figure 3.12), clearly indicates the tailorability of the transformation characteristics of AM NiTi through the control of the processing parameters, in particular VED. Using the measured M_s temperatures and the fact that the M_s temperature is controlled primarily by the Ni content in the solution heat-treated condition, it is possible to calculate the Ni content and the amount of Ni evaporation in the solution heat-treated AM samples, both as a function of the VED level (Figures 3.12g and h), using the well-known relationship between the Ni content and Ms temperatures of Ni-rich NiTi SMAs [62]. Impressively, there is a strong correlation between the amount of Ni evaporated and the VED level for the samples printed using the NR powder.

It should be noted, however, that for the similar values of VED, two printed parts might still have different transformation temperatures for some cases (e.g., Cases #4 and #9 for parts printed using the NR powder) as a result of different combinations of P, v, and h. In addition, it is also likely to obtain slightly different transformation temperatures in two parts printed with exactly the same processing parameters but with different part sizes. In this case, the difference in build times and, therefore, the duration that the part is exposed to laser beam may induce different levels of elemental evaporation. Although this study did not investigate in detail the influence of a specific processing parameter on the transformation characteristics of NiTi, Figure 3.12 still clearly presents that it is

indeed possible to tailor the Ni evaporation and the transformation temperatures of L-PBF Ni-rich NiTi parts based on the VED change.

It is also worth noting that the cubes listed in Table 3.1 were printed using the maximum hatch spacing predicted using our process optimization framework. However, the Ni concentration can be further controlled using smaller hatch spacing under the same *P* and *v* parameters. For the selected values of *P* and *v*, decreasing the hatch spacing value is expected to cause an increase in transformation temperatures (see parameter sets #19 and #21 in Table 3.2). Our previous study on AM of $Ni_{50.9}Ti_{49.1}$ (at. %) SMA reported that smaller hatch spacing values might also improve the functional properties through possible nano-precipitation hardening [37]. With the knowledge of the printability map and the VED dependence of transformation temperatures, printing functionally graded and porosity-free NiTi parts with location-specific properties would be simpler and more precise, presenting several opportunities for custom actuator applications.

3.5 Analysis of The Tension Coupon Prints

3.5.1 Fabrication and Density Evaluation

The process parameters used for printing Cubes #2, #3, #4, and #8 with the least porosity were also used to print 30 × 10 × 10 mm^3 rectangular prisms. All parts were printed in the same orientation, with their 30 × 10 mm top surface normal to the build direction. Dog-bone shaped tensile coupons were extracted from the prisms using wire-EDM, and the six porosity samples were also cut, as shown in Figure 3.13. To avoid

potential surface defects, tensile coupons were cut from the interior of the rectangular prisms by leaving 1 mm distance from each side of the prisms. Since the volume of rectangular prisms is larger than the cubes printed and presented in the previous section, the microstructure was evaluated at six different locations in case there might be compositional or microstructural inhomogeneities. The OM images of both horizontal and vertical surfaces confirmed that the rectangular prisms are almost fully dense, with density values greater than 99.9%, which is comparable to the results of the cube prints. Note that the densities in this context were calculated by subtracting the measured area fractions of porosity from 1. In addition, similar porosity values have been observed on all 6 surfaces of each rectangular prism, as shown in Figure 3.13a and b. Hence the porosity, and thus the density, results based on the image analysis should be representative for the entire part.

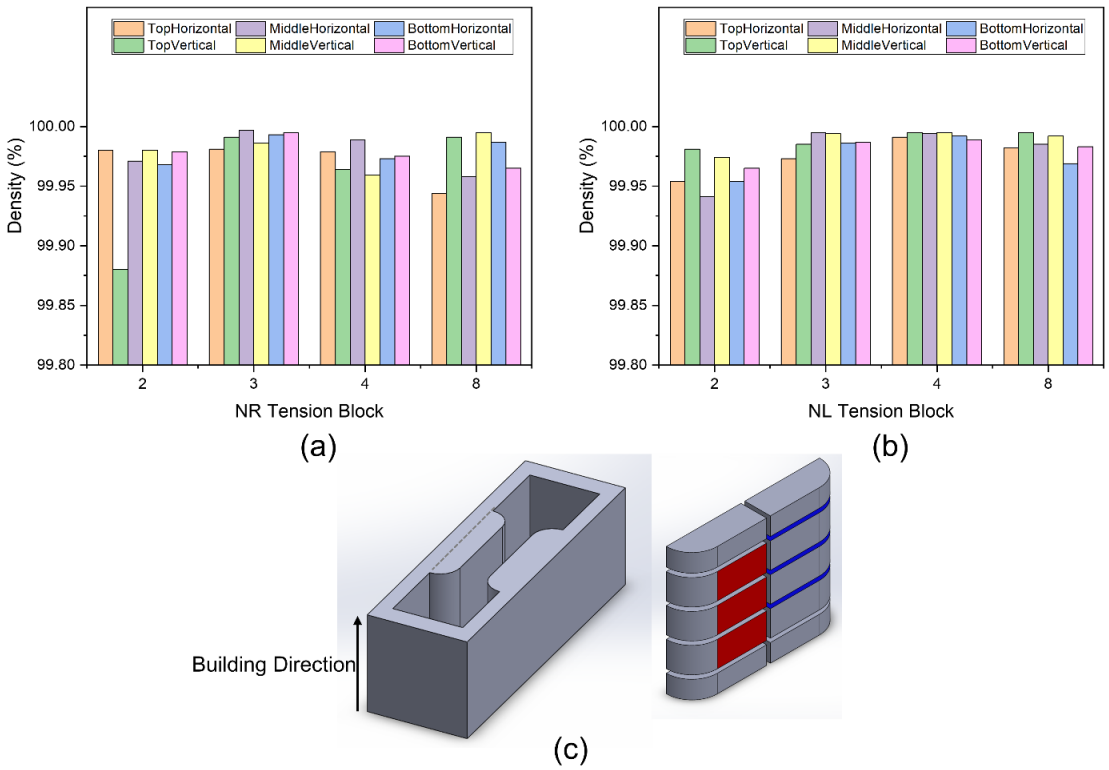

Figure 3.13 Density measured by the area analysis of the images (cross-section surfaces) for 30 × 10 × 10 mm^3 rectangular prisms fabricated using (a) NR ($Ni_{50.8}Ti_{49.2}$) and (b) NL ($Ni_{50.1}Ti_{49.9}$**)** powder. (c) 3D CAD models illustrating the preparation of dog-bone tension specimens and surfaces for porosity analysis. Three surfaces were cut parallel (shown in red), and three surfaces were cut normal to the build direction (shown in blue). The numbers in the x-axes of (a) and (b) indicate the process parameter sets in Table 3.1.

3.5.2 Thermomechanical Testing

Room temperature monotonic tensile failure tests were conducted for tensile coupons extracted from the rectangular prisms printed from NR and NL powders. DSC results indicate that samples cut from rectangular prisms have slightly higher transformation temperatures compared to the cubes fabricated with the same processing parameters (Figures 3.14a and b). Possible reasons for this difference might be the

precipitation of Ni-rich precipitates or increased Ni evaporation due to slight differences in the thermal history due to the part dimensions as discussed earlier. From these tests, mechanical properties such as the yield strength, ultimate tensile strength, and elongation to failure were extracted and summarized in Table 3.3.

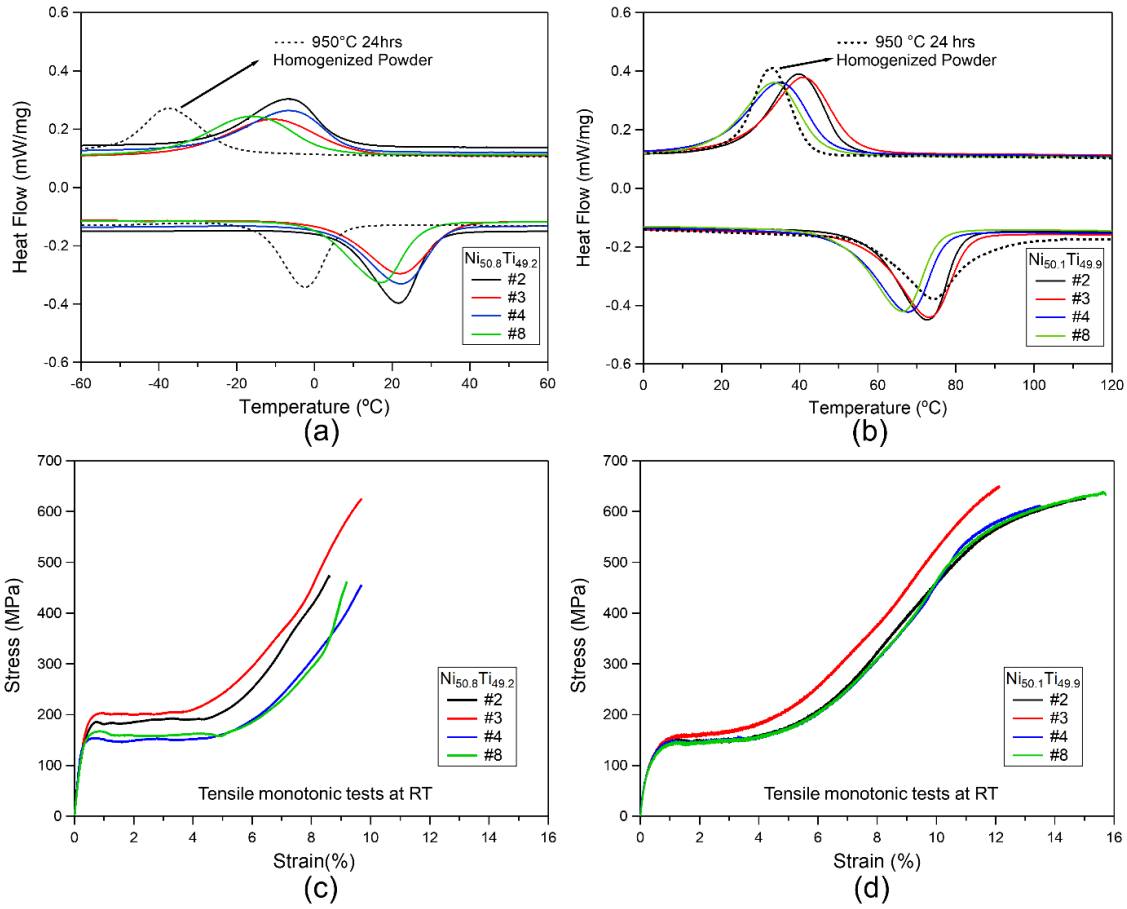

Figure 3.14 DSC results and room temperature isothermal monotonic tensile failure results for coupons printed from (a) NR ($Ni_{50.8}Ti_{49.2}$) and (b) NL ($Ni_{50.1}Ti_{49.9}$) powders using the Parameter sets #2, #3, #4, and #8 in Table 3.1.

Samples printed from NR powder are mostly austenitic at room temperature due to their low M_s temperatures. They exhibited a stress plateau region between 150 to 200

MPa, and the deformation mechanism should be a mixture of stress-induced martensitic transformation and martensite reorientation/detwinning (Figure 3.14c). Slight differences in the plateau stress levels result from the differences in transformation temperatures and the amount of austenite and martensite phases co-existing at room temperature. It is observed that, regardless of the plateau stress levels, all samples exhibit similar ductility levels around 9% (Figure 3.14c).

On the other hand, all specimens printed from NL powder exhibit a plateau region around 150 MPa, and the deformation was driven by the reorientation/detwinning of the self-accommodated martensite variants since the samples are martensitic at room temperature. The specimens fabricated from NL powder showed better ductility up to 16% (Figure 3.14d), which is relatively high compared to literature results for the AM NiTi parts fabricated using simple scanning strategies. As a comparison, two studies have reported similar [34] or better [25] ductility values on AM NiTi parts by employing a strip pattern scanning strategy and lower oxygen level at 25 ppm in the building chamber to minimize any possible oxide formation inside the built parts.

Table 3.3 Process parameters, transformation temperatures, and the monotonic tensile test results of the coupons extracted from 30 ×10 × 10 mm^3 tension blocks printed using NR and NL powders.

Powder	Process Parameters	P (W)	v (m/s)	h (μm)	M_s (°C)	A_f (°C)	Ultimate Tensile Strength (MPa)	Elongation to Failure (%)	Reorientation / Transformation Stress (MPa)
NR ($Ni_{50.8}Ti_{49.2}$)	**#2**	160	0.83	80	7.2	31.7	471	8.6	187
	#3	160	1.08	80	10.4	36.5	623	9.7	202
	#4	240	1.33	80	9.4	34.1	454	9.7	150
	#8	160	1.08	70	3.1	28.8	461	9.2	161
NL ($Ni_{50.1}Ti_{49.9}$)	**#2**	160	0.83	80	49.6	80.4	627	15.0	158
	#3	160	1.08	80	52.5	82.5	649	12.1	148
	#4	240	1.33	80	46.4	76.6	605	13.5	148
	#8	160	1.08	70	48.0	79.5	632	15.7	146

It is well known that superelasticity can be observed in NiTi in either Ni-rich compositions with the precipitation of coherent Ni_4Ti_3 nanoprecipitates or Ni-lean compositions, usually, after cold-deformation processes that strengthen the austenite matrix against dislocation plasticity [80]. In this study, since no post-printing heat treatments or deformation processes were intended initially, tension specimens printed from the NR powder were tested for superelasticity and shape memory effect, whereas specimens fabricated from the NL powder were tested only for the shape memory effect.

Incremental loading tests were conducted on all 4 cases of NR samples. Results of this test for Case #8 is presented in Figure 3.15a, where the material was loaded incrementally at 5°C higher than ©$_f$ temperature (A_f + 5 °C). Samples from other cases were tested in a similar fashion. Figure 3.15c summarizes these tests showing the

recovered strain as a function of total and incrementally applied strain levels (defined in Figure 3.15b). It is seen that the superelastic behavior of all 4 samples are similar, with Case #8 outperforming the others with a slightly increased recovered strain. Perfect superelasticity could not be achieved in any of the as-printed samples due to a lack of sufficient coherent Ni_4Ti_3 precipitation.

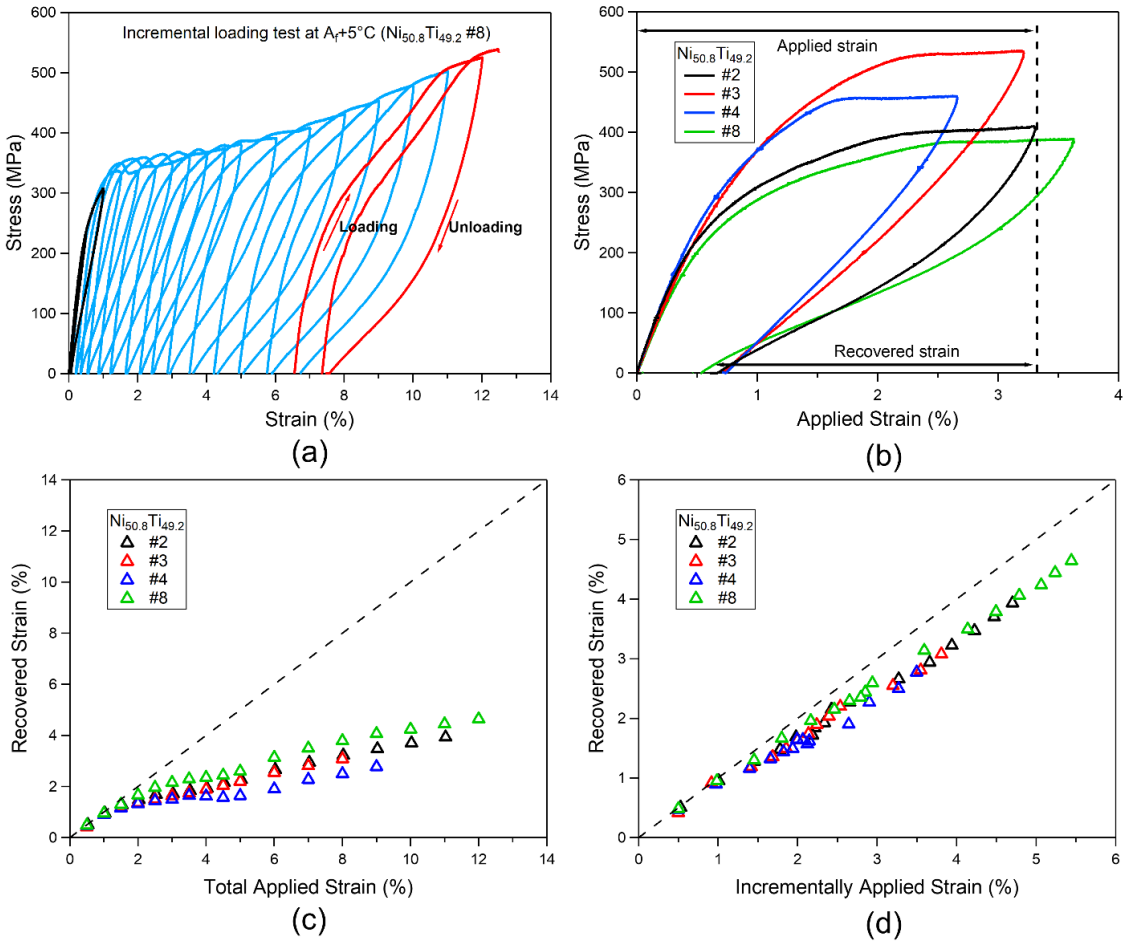

Figure 3.15 (a) Incremental loading test results performed at A_f + 5 °C (34 ± 2 °C) for the Case #8 sample fabricated using the NR ($Ni_{50.8}Ti_{49.2}$) powder. (b) The results of the cycles with 6% total applied strain for all four cases. Summaries of (c) recovered strain vs. total applied strain and (d) recovered strain vs. applied strain at each loading/unloading cycle of all cases fabricated using the NR powder extracted from

incremental loading test results.

Similar results were obtained during shape memory tests, with samples printed using the NL powder, showed up to 4 % recoverable strain after 6% deformation. Case #4 of NR powder was also tested for shape memory effect, and interestingly this sample could withstand 8% deformation and exhibit a recoverable strain of 6% (Figure 3.16a). Figure 3.16b summarizes the shape recovery capability of all specimens fabricated and tested in this study. As frequently observed in Ni-lean, precipitation free or solution annealed NiTi SMAs, even at small deformations such as 2%, some of the applied strain could not be recovered due to the insufficient strength of the matrix against defect generation. The highest recoverability was seen in Case #4 of NR powder at around 6 % strain, similar to the values recorded for conventionally fabricated Ni-lean NiTi alloys [81].

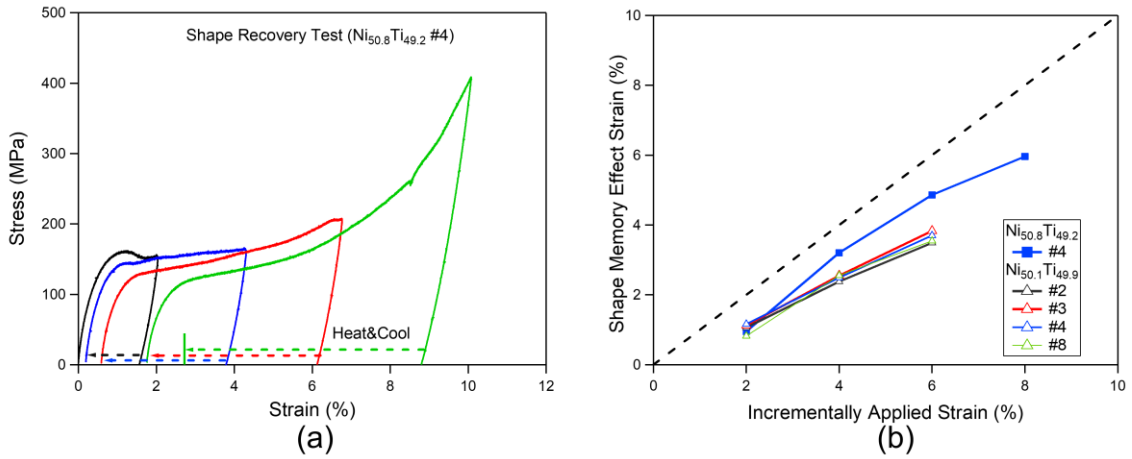

Figure 3.16 (a) Stress-strain behavior and shape recovery behavior of Case #4 sample fabricated using the NR ($Ni_{50.8}Ti_{49.2}$) powder. Sample was deformed in martensite at M_f – 50 °C at 2% increments and subsequently heated to A_f + 50 °C to recover the deformation (b) a summary of recovered strain vs. incrementally applied strain (at each cycle) for all 4 cases fabricated using the NL powder plus Case #4 of NR powder.

3.5.3 Post-fabrication Heat Treatment

To improve the superelasticity observed in the samples printed from NR powder, post-fabrication aging heat treatments were performed on the Case #8 sample at temperatures ranging from 300 to 500 °C for 1 to 3h. Corresponding DSC results of solution heat treated and aged Case #8 samples are summarized in Figure 3.17a. It is seen that solution heat treatment at 800 °C for 1h sharpened the transformation peaks and lowered the transformation temperatures of the as-printed Case #8 part. However, the transformation enthalpy, measured as the area under the peaks, did not change due to solution heat treatment, indicating that the transforming volume of the material remained essentially unchanged. For aged samples, no solution heat treatment was executed prior to aging, first to avoid any possible impurity pick up at a relatively high temperature of 800 °C, and second for practical purposes, i.e., directly annealing samples in air without going through difficult vacuum heat treatment procedures. All aged samples showed multi-stage and/or R-phase transformation during cooling and exhibited higher reverse transformation temperatures (Figure 3.17a). Two broad peaks during forward transformation in the DSC curves of the 400 °C – 1h aged sample (Figure 3.17a) are likely to indicate the inhomogeneity caused by the formation of Ni_4Ti_3 precipitates, similar to what is observed in bulk samples [79]. Coherent Ni_4Ti_3 precipitates, which act as barriers to dislocation slip, can improve the strength of NiTi depending on their size and inter-particle distance [78]. The aged samples were further tested to characterize the superelasticity. As seen in Figures 3.17b and e, the specimen aged at 400 °C for 1h

showed slightly better superelasticity than as-printed specimens and other aging conditions, with larger recovered strain. However, none of the aged specimens could display perfect superelasticity due to the insufficient amount of Ni available in the matrix and, thus, the formation of an insufficient fraction of Ni_4Ti_3 precipitates, as explained below.

Figure 3.17c presents the DSC results of the bulk NiTi with the same composition of the NR powder (before printing) and after different aging conditions (same conditions with the post-fabrication heat treatments applied to the as-printed NR samples) for comparison purposes. The bulk material exhibits two widely separated peaks during the forward transformation in the as-received (vacuum induction melted and hot-rolled at 900 °C) condition. The peak at high temperature corresponds to the B2 to R phase transformation. This indicates that slow cooling after hot rolling must have led to the formation of Ni_4Ti_3 precipitates resulting in the appearance of R-phase transformation. Solution heat treatment of the as-received bulk material at 800 °C for 1h leads to the disappearance of the R-phase, and the material exhibits a single-step transformation with an M_s temperature around -20 °C. Aging of the solution heat-treated bulk material results in multi-stage and/or R-phase transformation, with some cases (e.g.500 °C 1h) exhibiting 3 stage transformation. In 800 °C for 1h solution heat-treated condition, the bulk material showed partial superelasticity similar to AM NiTi. Still, when the solution heat treatment is followed by aging at 400 °C for 1h, the material exhibited almost perfect superelasticity up to 7% applied strain (Figure 3.17d).

The reason for the substantial difference between the superelastic responses of the AM NR NiTi and the bulk NiTi with the same initial Ni contents is the evaporation of Ni during printing and lack of sufficient Ni to allow the formation of a desirable level of Ni_4Ti_3 precipitates in the printed samples. During the printing process in L-PBF, the sub-layers are reheated while the top-most layer goes through melting and solidification. Hence aging may be promoted in the sub-layers depending on the temperature these layers are exposed to and the duration of the exposure. The tension blocks that the superelastic tests were performed were printed with the maximum hatch spacing value predicted by the hatch spacing criterion mentioned above. By reducing the hatch spacing, one can argue that the samples should undergo aging heat treatment for a longer period of time, and the process of forming Ni_4Ti_3 precipitates may be extended. On the other hand, more Ni will be evaporated due to the increased VED due to decreasing the hatch spacing. Consequently, the remaining Ni content in the samples may not be sufficient to form Ni_4Ti_3 precipitates. Therefore, to achieve better superelasticity than what is reported here in as-printed samples, it is necessary to use NiTi powders with a higher Ni/Ti ratio than what is used here, which should allow smaller hatch spacing (longer printing time) to form enough Ni_4Ti_3 precipitates in the as-printed samples.

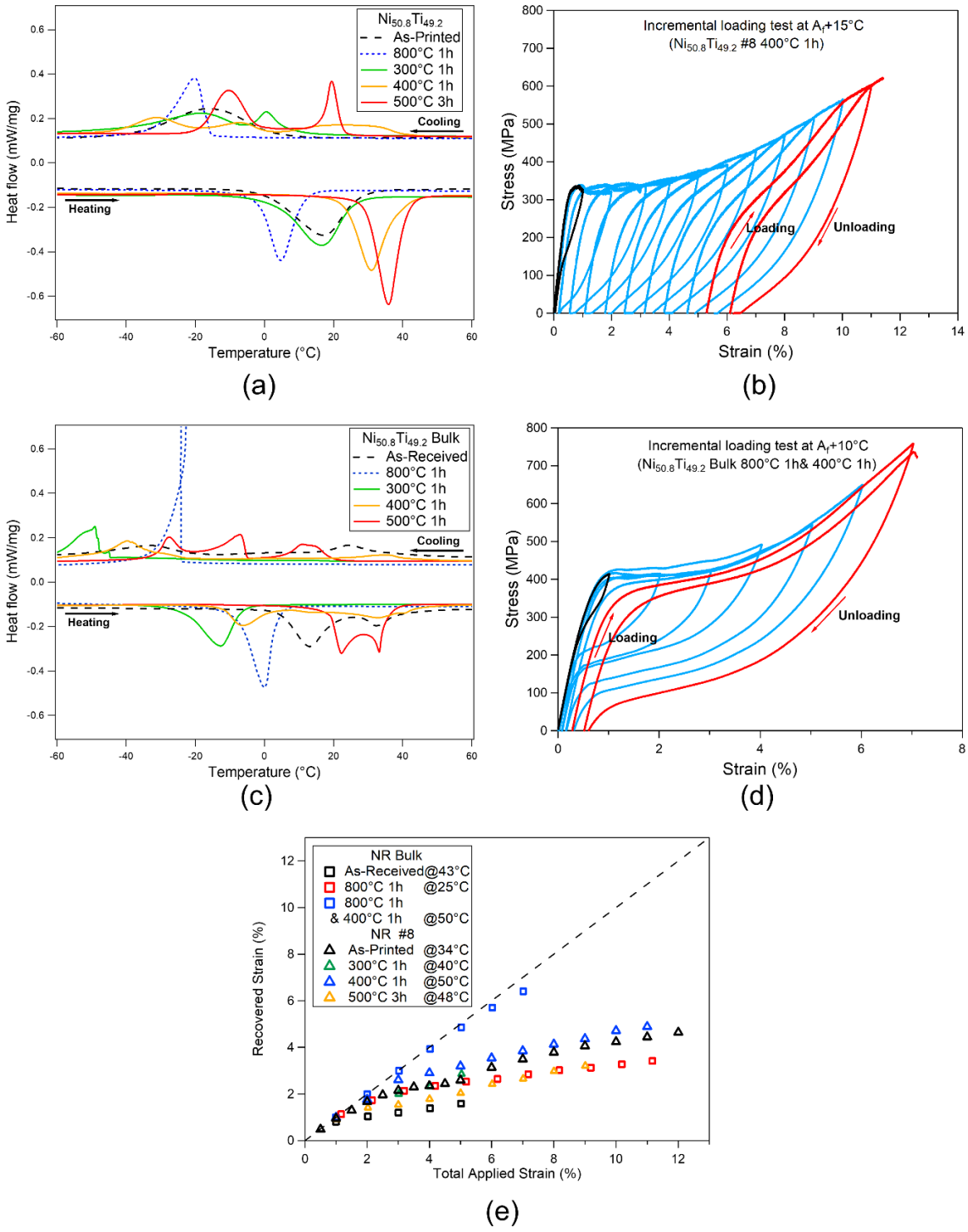

Figure 3.17 (a), (c) DSC results and (b), (d) incremental loading test results for the Case #8 sample fabricated using the NR ($Ni_{50.8}Ti_{49.2}$) powder and the corresponding bulk sample having the same composition as the NR powder. DSC results include the measurements on the as-

printed (a) or as-received (c) samples and after solution heat treatment and various aging heat treatments. Incremental loading tests were performed after aging treatment at 400 °C for 1 h for both the printed and bulk samples. (e) Summary of recovered strain vs. total applied strain levels extracted from the cases the incremental loading tests were conducted on.

3.5.4 Microstructure Evolution (Transmission Electron Microscopy)

To elucidate whether Ni_4Ti_3 precipitates form in as-printed and as-printed plus aged conditions, TEM study was performed on the Case#8 sample fabricated using the NR powder in both as-printed and 400 °C - 1h aged conditions. Figure 3.18a is a low magnification bright-field (BF) image of the as-printed sample showing the existence of particles with different contrasts and a wide size range from a few nanometers up to 80 nm. Based on the EDX results, two types of particles, bright needle-shaped (Figure 3.18b) and dark spherical (Figure 3.18c) particles, exist in the matrix. Elemental EDX maps in Figures 3.18d to f indicate that the bright particles are rich in Ti and O, while they are lean in Ni. Therefore, it is concluded that these particles are TiO_x type oxides. The spherical particles included the same amount of Ni as the matrix, and Ti amount was almost twice the Ni content in the particle. Thus, it is likely that these particles are $Ti_4Ni_2O_X$ type oxides. It has been reported that the oxides may form at high temperature around 1000 °C even under Ar protection [25, 82], and the presence of the oxides may compromise the ductility and structural stability of the printed part. However, neither bright field images nor various diffraction patterns in the two different TEM foils of the as-printed samples reveal any sign of Ni_4Ti_3 precipitates.

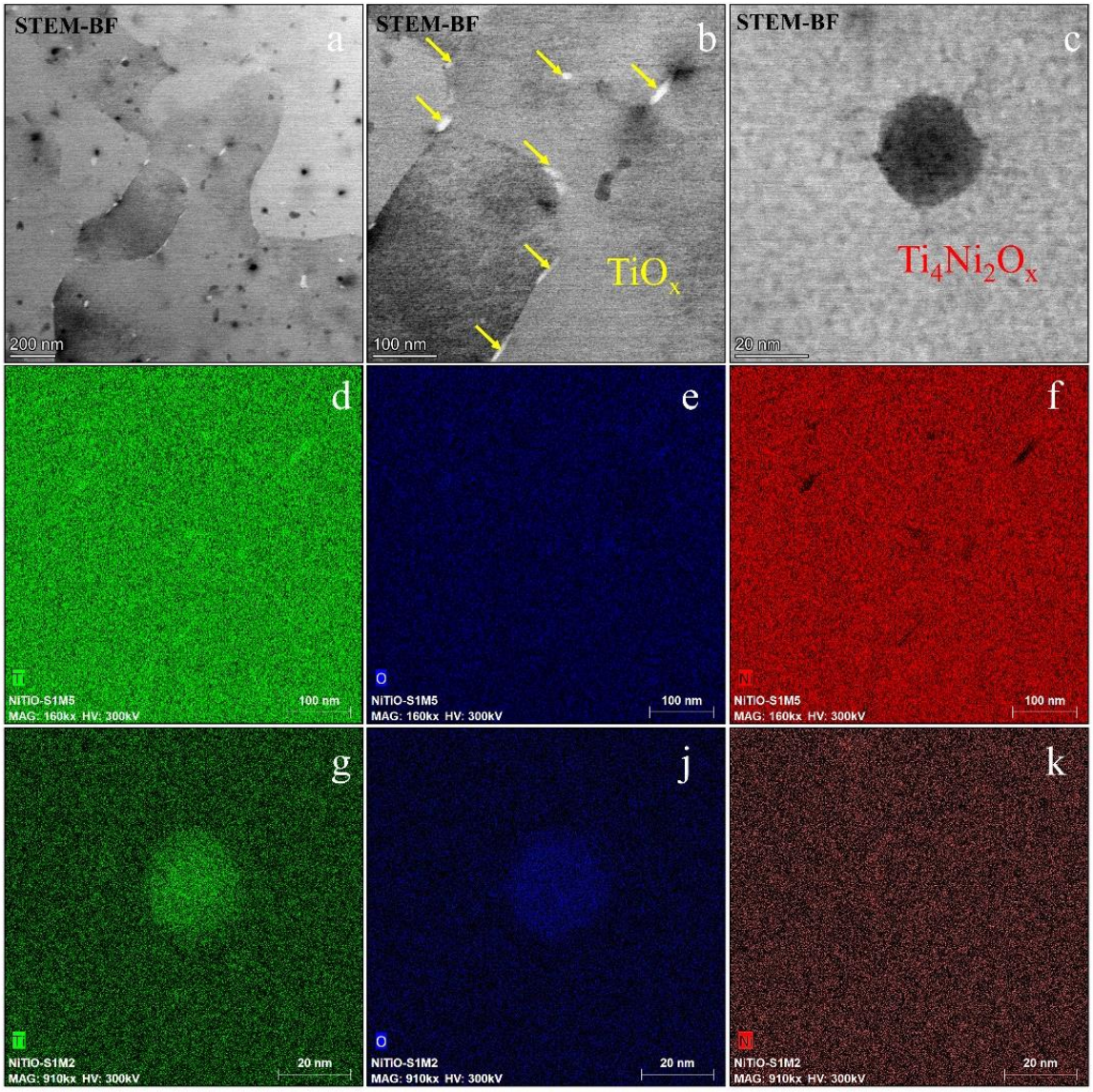

Figure 3.18 Transmission electron microscopy images of the as-printed Case #8 material of the NR powder, a) lower magnification bright-field TEM image showing different types of second phase particles, (b) higher magnification of (a) displaying the preferential formation of TiO_x particles along grain boundaries, (c) higher magnification of (a) presenting spherical $Ti_4Ni_2O_x$ oxide with a diameter of 20 nm. EDX maps exhibit the chemical distribution for the particles in (b) and (c) through (d-f) and (g-k), respectively.

TEM analysis has also been performed on the 400 °C -1h aged Case #8 sample. In addition to the oxide particles observed in the as-printed sample, the R-phase regions and Ni_4Ti_3 precipitates were detected (Figures 3.19a and b) in the aged samples. The diffraction pattern in Fig.19c displays the existing phases in the matrix. Based on the selected area electron diffraction pattern (SADP) (Figures 3.19c and d), with the zone axis of $[210]_{B2}$, 1/3 <120> reflections indicate the presence of the R-phase [83, 84]. Moreover, the 1/7 <321> reflections in Figure 3.19c prove the existence of Ni_4Ti_3 precipitates, also clearly observed in the STEM and High-angle annular dark-field (HAADF) images in Figures 3.19a and b. The size of Ni_4Ti_3 particles ranges from 25 to 35 nm (Figure 3.19a and b).

Considering the transformation temperature difference (Figure 3.11, Figure 3.20a and Figure 3.20b) before and after solution heat treatment in the NiTi prints, the microstructure in the as-printed condition may vary with their composition or corresponding VED. Figure 3.20c and Figure 3.20d show the change of transformation based on the estimated Ni (at. %) calculated from the solution heat treated DSC results. At Ni content (at. %) above 50%, transformation temperatures are higher in as-printed condition as the potential formation of Ni-rich precipitates, which are not confirmed by the TEM study, will decrease the Ni content in the matrix. While due to the residual stress from the large thermal gradient during the printing process or dislocation formation, the transformation temperatures are lower in the as-printed condition when Ni content (at. %) is lower than 50%.

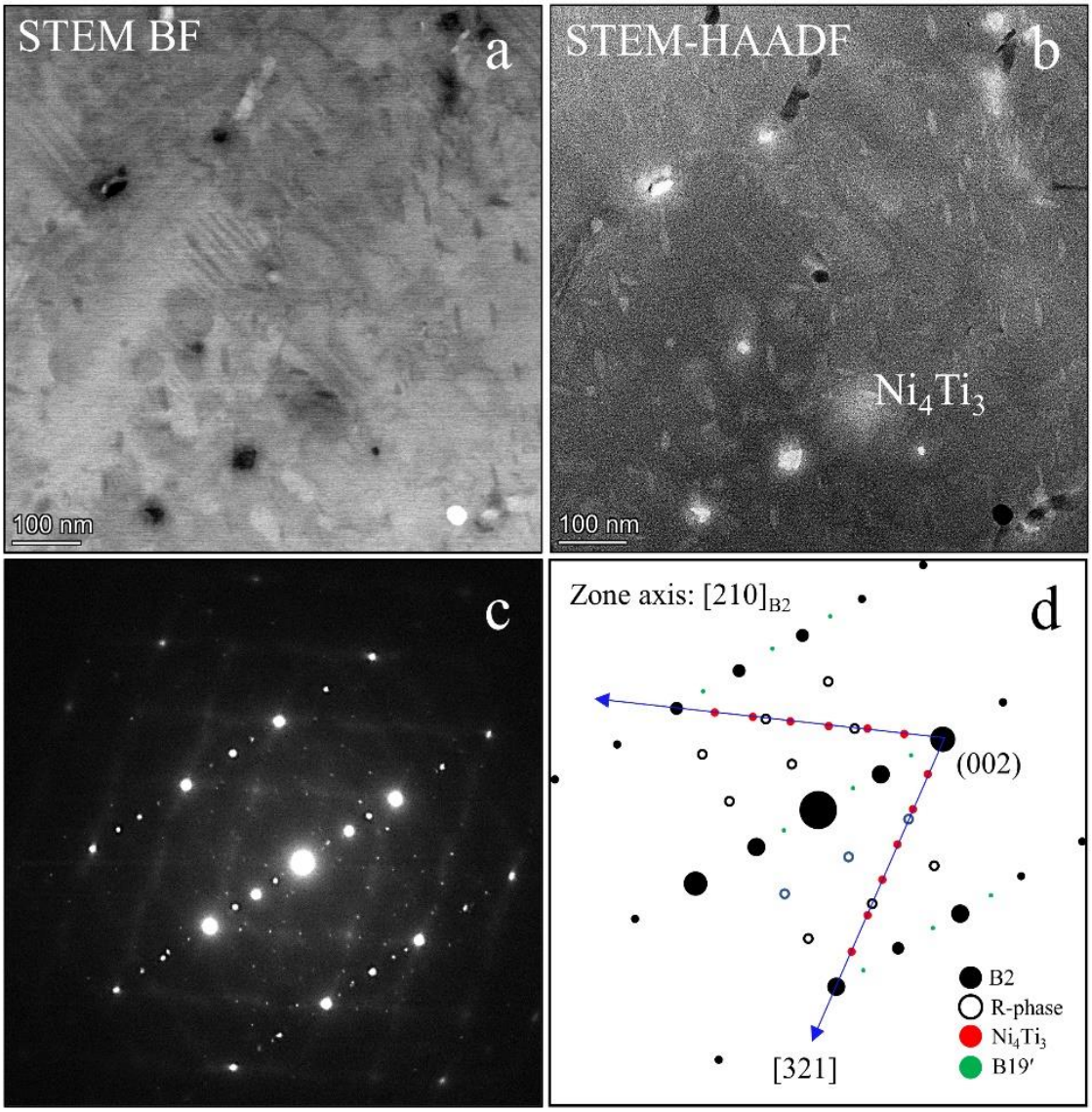

Figure 3.19 Transmission electron microscopy investigation of the as-printed Case #8 sample of the NR powder after aging at 400 ^{o}C for 1 h, a) bright-filed STEM images b) angular, dark field images of (a), (c) selected area electron diffraction pattern (SADP) in the $[210]_{B2}$ zone axis, d) schematic presentation of SADP in (c).

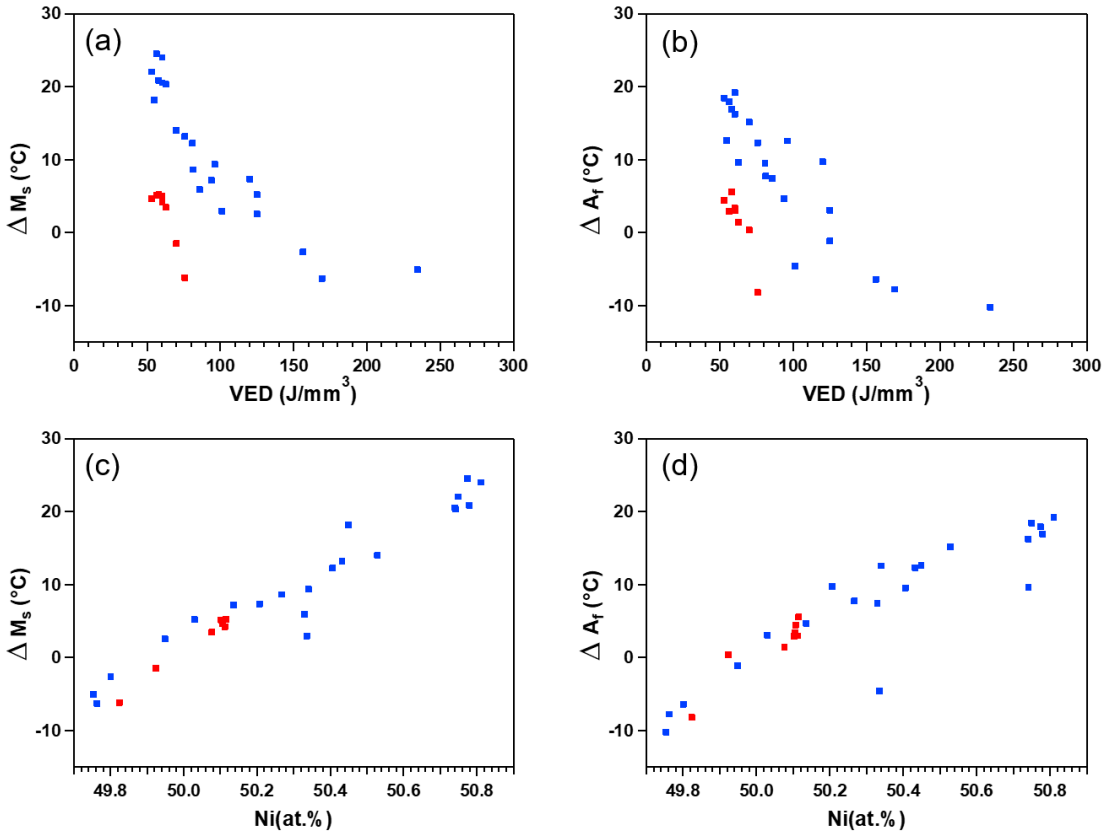

Figure 3.20 (a) ΔM_s vs. VED, (b) ΔA_f vs. VED, (c) ΔM_s vs. Ni(at.%), and (d) ΔA_f vs. Ni(at.%). ΔMs and ΔAf reprensent the transformation temperature(TT) changes after solution heat treatment ($\Delta TT = TT_{As\text{-}printed} - TT_{SHT}$).

3.6 Summary

In this chapter, a process optimization guided methodology based on a computationally inexpensive analytical thermal model was used to construct a near-optimal printability map for printing fully dense parts of NiTi shape memory alloys (SMAs) with two different compositions via Laser Powder Bed Fusion (L-PBF). One of the compositions was near-equiatomic $Ni_{50.1}Ti_{49.9,}$ and the other one was Ni-rich NiTi ($Ni_{50.8}Ti_{49.2}$). It was concluded that the Ni content of the starting powder should be

slightly higher than the one used in this chapter to be able to form a sufficient fraction of Ni_4Ti_3 precipitates and to achieve lower transformation temperatures in the as-printed parts, such that higher superelastic strains and possibly complete superelasticity can be achieved in 3-D printed Ni-rich NiTi SMAs.

CHAPTER IV

LASER POWDER BED FUSION OF DEFECT-FREE NITI SHAPE MEMORY ALLOY PARTS WITH SUPERIOR TENSILE SUPERELASTICITY FROM $NI_{51.2}TI_{48.8}$ (AT. %) POWDER

Few additively manufactured NiTi parts have been reported to exhibit superelasticity under tension in the as-printed condition, without a post-fabrication heat treatment, due to either persistent porosity formation or brittleness from oxidation during printing, or both. In this Chapter, NiTi parts were fabricated from $Ni_{51.2}Ti_{48.8}$ (at. %) powder using L-PBF and consistently exhibited room temperature tensile superelasticity up to 6% in the as-printed condition, almost twice the maximum reported value in the literature. In addition to the framework explained in the previous Chapter, this was achieved by eliminating porosity and cracks through the use of optimized processing parameters, carefully tailoring the evaporation of Ni from a Ni-rich NiTi powder feedstock, and controlling the printing chamber oxygen content. Crystallographic texture analysis demonstrated that the as-printed NiTi parts had a strong preferential texture for superelasticity, a factor that needs to be carefully considered when complex shaped parts are to be subjected to combined loadings. Transmission electron microscopy investigations revealed the presence of nano-sized oxide particles and Ni-rich precipitates in the as-printed parts, which play a role in the improved SE by suppressing inelastic accommodation mechanisms for martensitic transformation.

Figure 4.1 below shows a flowchart summarizing the experimental methods utilized in this chapter.

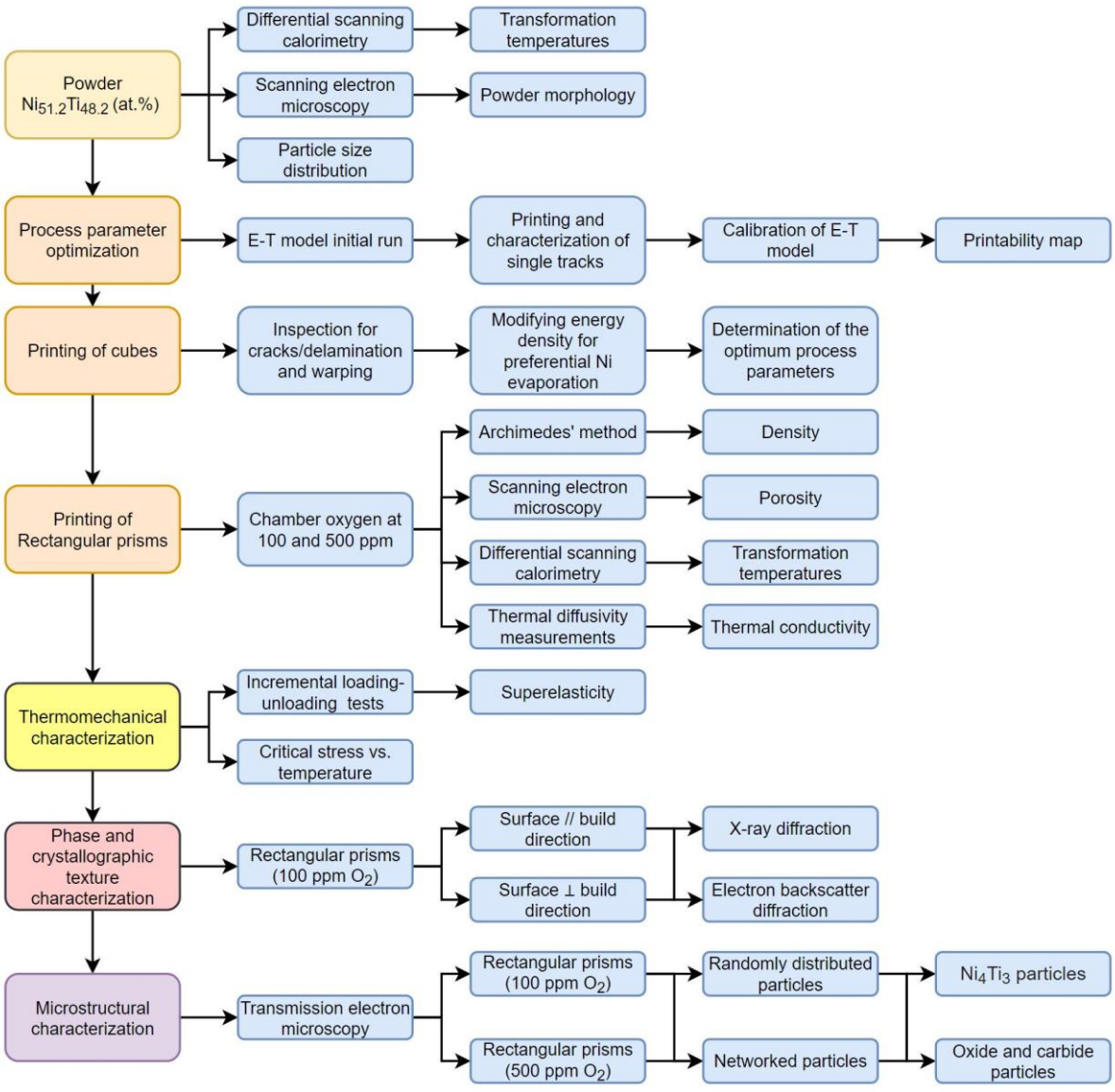

Figure 4.1 Flowchart summarizing the experimental methods used and properties/features measured/detected in this study.

4.1 Materials and Experimental Methods

4.1.1 Powder Characterization

A NiTi shape memory alloy ingot with a nominal composition of $Ni_{51.2}Ti_{48.8}$ (at. %) was acquired from Fort Wayne Metals and then gas-atomized by Nanoval GmbH & Co. KG. Solution heat treatment of powder samples was performed at 950 °C for 24 h in quartz tubes with protective argon atmosphere followed by quenching and breaking the tubes in water at room temperature to homogenize the powder and thus, determine the transformation temperatures. A TA instruments Q2000 differential scanning calorimeter (DSC) was used to measure the transformation temperatures of the as-received and solutionized powders. Two thermal cycles were run between -150 °C and 150 °C at a heating/cooling rate of 10 °C/min. Transformation temperatures were determined from the second cycle results using the tangent line interception method following ASTM F2004-17 [53]. A FEI Quanta 600 FE scanning electron microscope (SEM) operated at 20 kV was used to investigate the morphology and size distribution of the powder particles.

Based on SEM observations, as-received NiTi powder has mostly spherical particles with sizes ranging from 5 μm to 70 μm (Figures 4.2a and b). d_{50} and d_{80} values are 20 μm and 32 μm, respectively (Figure 4.2c). DSC results indicate that the as-received powder exhibits a broad peak during reverse transformation around -10 °C (Figure 4.2d). After solutionizing at 900 °C for 1h in a protective argon atmosphere, no transformation peaks were observed down to -150 °C, indicating the Ni content in this

powder would be at least 51 at. % based on the M_s temperature prediction with respect to Ni content [40].

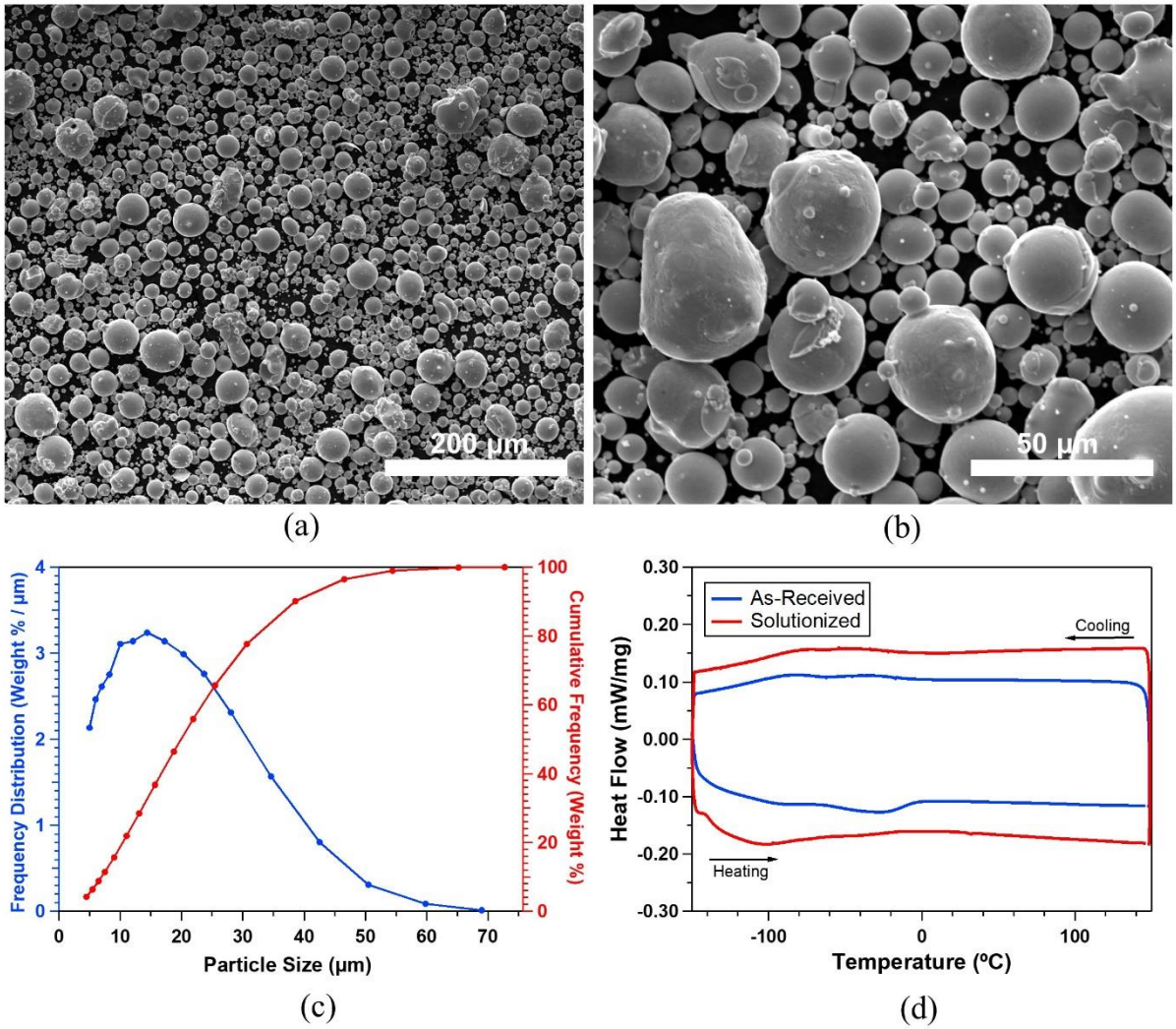

Figure 4.2 (a) Low-magnification and (b) higher magnification SEM images of the as-received $Ni_{51.2}Ti_{48.8}$ powder. (c) Particle size distribution (PSD) of the powder and (d) differential scanning calorimetry (DSC) results of both as-received powder and powder after a solution heat treatment at 950 °C for 24h.

4.1.2 Single Track Experiments and The Printability Map

A 3D Systems ProX DMP 200 L-PBF system with a fibre laser of 1070 nm wavelength and beam diameter of 80 μm was used to fabricate the NiTi parts. Equiatomic NiTi (i.e., $Ni_{50}Ti_{50}$ (at. %)) plates were used as substrates for the prints and were sandblasted with 50 μm aluminum oxide prior to printing in order to achieve better powder spreading and coverage of the substrate. Layer thickness (t) was set to 32 μm during printing of single tracks, cubes, and rectangular prisms to have at least 80% of the powder within the layer based on the particle size distribution (PSD) information.

10 mm long single tracks (Figure 4.2) with 1 mm intervals were printed on an equiatomic NiTi substrate using 66 different P and v combinations, with a range of (P,v) = (40-240 W : 0.08-2.33 m/s). Top-view SEM images were taken from the middle of each single track and six width measurements were conducted to assess the continuity of the tracks. Cross-section samples of the single tracks were prepared using wire electrical discharge machining (wire-EDM) and then grinding with up to 1200 grit sandpaper followed by a final polishing with water based colloidal silica (0.25 μm) suspension. The polished surfaces were then etched with an etchant of 1 part HF, 2 parts HNO_3 and 10 parts distilled water for 15s to reveal the grains and the melt pool shapes. Optical microscopy images of the single-track cross-sections were taken using a Keyence VH-X digital microscope and d was calculated as the average of three different cross-section measurements.

Melt pool depth (d) and width (w) values showed an increasing trend with increasing linear energy density (LED = P/v) (Figures 4.4Figure 4.4a and b). In general, for the combinations resulting in relatively low levels of LED, the laser was not able to

melt the entire powder layer and left no tracks on the substrate or resulted in tracks with non-uniform width and discontinuity, causing the lack of fusion phenomenon (Figures 4.3d). On the other hand, when the LED was relatively high, vaporization of elemental constituents resulted in trapped gases within the melt pools, leading to the keyholing defect (Figures 4.3d). It is also observed that the melt pool becomes unstable when P and v are both high, and the single tracks break into discontinuous droplets on the substrate, causing the balling phenomenon (Figures 4.3c).

The reader is referred to chapter 3 for details on the selection of different material properties used in the E-T model. With the measured melt pool dimensions from the single-track experiments, the model was calibrated in order to more precisely predict the melt pool dimensions corresponding to different P and v values. The printability map (Figure 4.4c) could then be constructed taking into consideration the different regions.

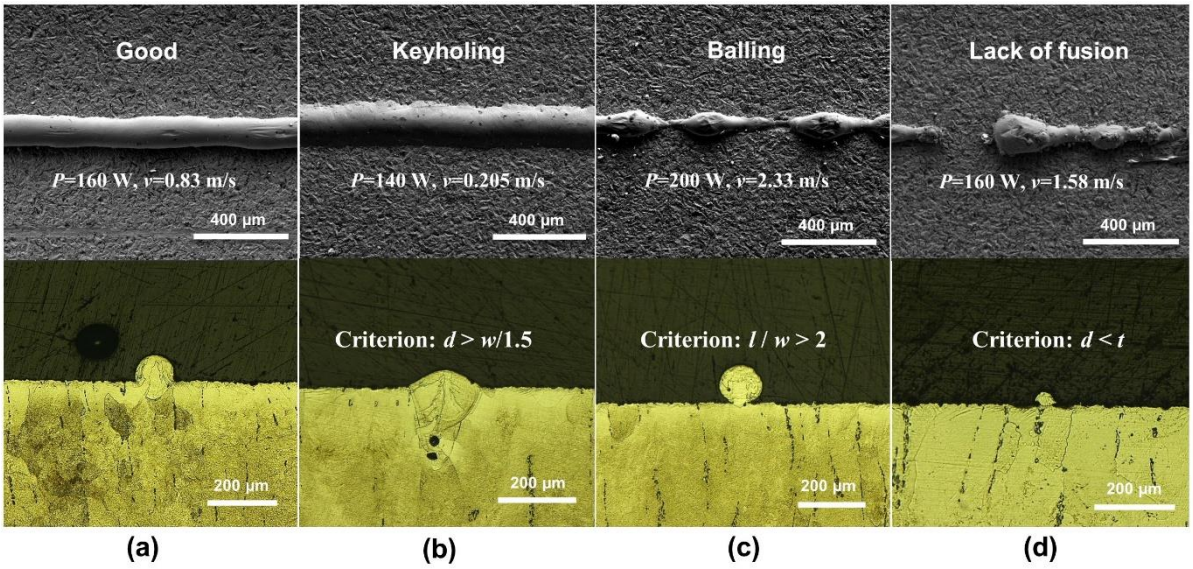

Figure 4.3 Single track top-view SEM images and cross-sectional optical microscopy (OM) images displaying the examples of the single tracks with (a) good print quality, (b) keyholing defect, (c) balling defect and (d) lack of fusion defect.

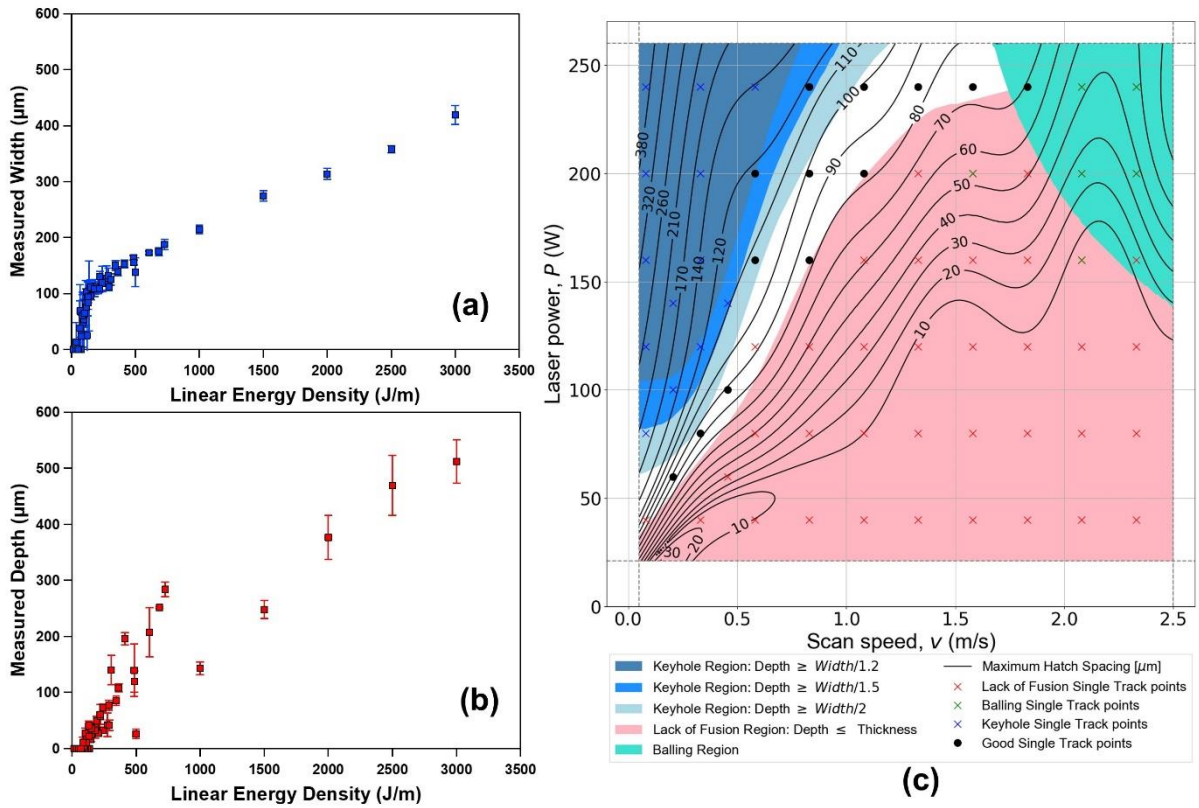

Figure 4.4 Variation of melt pool measured (a) width and (b) depth as a function of linear energy density (*P/v*) in printed single tracks. (c) Calibrated printability map of the as-received $Ni_{51.2}Ti_{48.8}$ (at. %) powder.

4.1.3. Density and Porosity Measurements

Density of the as-printed rectangular prisms was measured using Archimedes' method following ASTM B962-17 [85]. A quantitative density comparison of the as-printed parts was also conducted by the porosity analysis of SEM images, taken from the cross-sectional surfaces parallel to the build direction. These images were then processed using ImageJ software to calculate the porosity amount.

4.1.4 Thermal Properties and Thermomechanical Characterization

3 mm diameter x 1 mm thick DSC samples were wire-EDM cut from the as-printed rectangular prisms. DSC samples were initially used to find the transformation

temperatures of as-printed parts. 2 thermal cycles were run between -150 °C and 150 °C at a heating/cooling rate of 10 °C/min. The samples were subsequently solutionized at 800 °C for 1 h to dissolve any possible secondary phases and retested for 2 more thermal cycles in an effort to indirectly determine the matrix Ni content based on the martensite start (M_s) temperatures as outlined in [62] due to the difficulties associated with detecting small changes in Ni content through conventional chemical analysis. Thermomechanical testing was performed using a servo hydraulic MTS test frame with heating and cooling capability. Incremental loading-unloading tests were conducted on dog-bone tension specimens with gage dimensions of 8 mm × 3 mm × 1 mm at a nominal strain rate of 5×10^{-4} s^{-1} and at different temperatures above the A_f temperature for characterizing the SE of the as-printed parts. Specimens were initially loaded to 0.5% strain, unloaded and the loading-unloading cycles continued with 1% increments until failure occurred. To characterize the transformation stress as a function of temperature, specimens were loaded at different temperatures to 1% strain, unloaded and heated up to 100 °C for full recovery, a temperature well above the A_f temperature.

4.1.5 Phase Analysis and Crystallographic Texture Study

Two cross-sectional samples (perpendicular to and along the build direction) wire-EDM cut from the rectangular prisms were mechanically ground and polished using the same procedure used to prepare optical microscopy samples. Polished samples were then heated to 100°C and cooled down to RT to recover any residual martensite before running the X-ray diffraction (XRD) and EBSD analyses. Phase analysis was conducted using a Bruker D8 Discover X-ray Diffractometer equipped with a Vantec 500 detector and Cu K_α (0.15406 nm) X-ray source. The texture and microstructure of these surfaces were investigated utilizing a TESCAN FERA SEM with EBSD detector from Oxford Instruments. Large sample areas were analysed using step size of 1.3 μm whereas a detailed analysis of smaller areas was performed using a step size of 0.1 μm with a tilt angle of 70°. The EBSD raw data was processed using Aztec Crystal software to plot inverse pole figure maps, pole figures, and kernel average misorientation (KAM) maps. For the evaluation, misorientations greater than 15° were defined as high-angle grain

boundaries whereas those greater than 2° but less than 15° were defined as low-angle grain boundaries. KAM was calculated using the 3rd order neighbors (kernel size) and maximum misorientation angle of 5°.

4.1.6 Transmission Electron Microscopy (TEM)

TEM experiments were performed on the cross-section surfaces (both perpendicular and parallel to the build direction) from rectangular prisms to investigate any possible oxide inclusions and precipitate formation that may affect the thermomechanical properties of the printed parts. TEM foils were prepared by initially mechanical grinding of slices wire EDM-cut from the rectangular prisms down to 50 µm, followed by punching of foils with a diameter of 3 mm. Foils were finally ion milled using a Gatan PIPS II at -165 ºC. A JEOL ARM200F scanning transmission electron microscope (STEM) was used at an accelerating voltage of 200 kV. STEM energy-dispersive X-ray spectroscopy (EDS) was also used to detect the chemical composition of the precipitates.

4.1.7 Thermal diffusivity measurements

Thermal diffusivity measurements were performed on 1 mm thick, 10 x10 mm square cross sections which were wire-EDM cut from the rectangular prisms. From each prism, seven samples were cut normal to the build direction from varying build heights with 0.33 mm between samples. Additionally, three samples with faces parallel to the build direction were cut from each prism. It should be noted that since thermal diffusivity is measured through the thickness of the specimen, when a surface normal to the build direction is characterized, the measured diffusivity is parallel to the build direction. All samples underwent thermal diffusivity measurement using a TA Instruments DXF 200 high-speed Xenon-pulse delivery source and solid-state PIN detector. Measurements were taken at approximately 50 ºC temperature intervals as the samples were heated from -150 ºC to 150 ºC. The measurements were repeated during cooling from 150 ºC to -150 ºC. Specific heat capacity values were obtained from the respective DSC curves via the sapphire standard method. Thermal conductivity was then calculated according to the equation: $k = \alpha \cdot \rho \cdot c_p$, where k is thermal conductivity, α is thermal diffusivity, ρ is density, and c_p is specific heat capacity.

4.2 Fabrication of Bulk Cube Prints

Once the calibrated printability map (Figure 4.4c) was obtained based on the measured single tracks following the methodology summarized in [32, 86, 87], four *P* and *v* combinations (Table 4.1) were selected from the "Good" region (Figure 4.4) that yielded continuous tracks with reasonable penetration to the substrate (e.g. deeper than the layer thickness, *t*). The maximum value of the hatch spacing between adjacent laser tracks was calculated using the formula $h_{max} = w\sqrt{1 - \frac{t}{(t+d)}}$ [32] to ensure sufficient overlap between adjacent tracks and provide integrity to the single layer.

Table 4.1 Processing parameters used for printing 10 x 10 x 10 mm^3 cubes and 30 x 10 x 10 mm^3 rectangular prisms. Layer thickness, *t* was set to 32 µm for all prints, which is the d_{80} of the powder used.

Print ID	Power, *P* (W)	Scan Speed, *v* (m/s)	Hatch spacing, *h* (µm)	Volumetric energy density, VED (J/mm^3)	O_2 level (ppm)
Cube #1	240	1.83	65	63	500
Cube #2	240	1.58	70	68	500
Cube #3	160	1.08	60	77	500
Cube #4	60	0.205	85	108	500
Cube #5	60	0.205	61	149	500
Cube #6	240	1.58	24	198	500
Prism #1	240	1.58	24	198	500
Prism #2	240	1.58	24	198	100

At first inspection of Cubes #1 to #4 (Figure 4.5), macroscopic defects such as delamination from the substrate, cracks and warping were found to be too severe, although the processing parameters were selected from the "Good" region on the printability map. The severity of the defects was also found to decrease with increasing

VED values. It should be noted that these defects were not observed in parts printed with a less Ni-rich, i.e. $Ni_{50.8}Ti_{49.2}$ (at. %) powder using the same process optimization framework in a previous study, even at lower VED values [86]. Possible reasons for the overall inferior quality of prints with the $Ni_{51.2}Ti_{48.8}$ (at. %) powder of the present study will be discussed in Section 4.1. In an effort to mitigate these macroscopic defects, two more cubes (Cubes #5 and #6) were printed using the same processing parameters of the Cubes #4 and #2, but with smaller hatch spacing (*h*) values to reach higher VED values of 150 and 198 J/mm^3, respectively. By using this method, warping and delamination issues were dramatically reduced (Figure 4.5) and Cube #6 was found to have the overall best print quality.

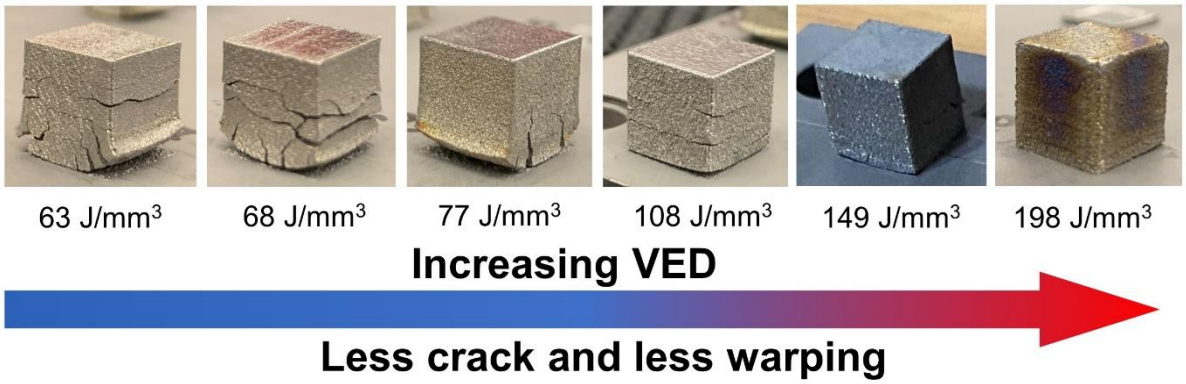

Figure 4.5 As-printed cubic $Ni_{51.2}Ti_{48.8}$ parts showing diminishing grades of macroscopic defects such as cracks, warping and delamination, with increasing volumetric energy density (VED).

Since Cube #6, fabricated at a VED value of 198 J/mm^3, displayed the best print quality among other cubes, the *P*-*v* combination used to print Cube #6 was utilized to

print two rectangular prisms to be able extract dog-bone tension specimens and perform mechanical testing. The 30 x 10 x 10 mm^3 as-printed rectangular prisms were found to be mainly austenitic microstructure under ambient conditions based on the DSC results (Figure 4.6) with an A_f temperature ~ 26 °C. During the incremental loading-unloading test performed both at room temperature (25 °C) (Figure 4.6) and slightly above the A_f temperature (30 °C) (Figure 4.6), the tensile specimen extracted from one of the as-printed rectangular prisms showed early failure. The sample exhibited very low ductility, failing at 1% without a distinct stress plateau indicative of the martensitic transformation. As evident from the oxide layer on the fabricated samples (Figure 4.7), the early failure may be attributed to the severe oxidation that took place under the high VED of 198 J/mm^3.

In an effort to increase the ductility of the as-printed NiTi parts, O_2 level in the printer chamber was lowered from 500 ppm to 100 ppm by purging more argon through the system and another rectangular prism was fabricated using the same set of parameters. The rectangular prism printed at a 100 ppm build chamber O_2 content (referred to as S100 hereafter) is noticeably less oxidized based on the colour differences when compared with the rectangular prism fabricated under 500 ppm O_2 (referred to as S500 hereafter) (Figure 4.7b). Unlike S500, S100 material showed enhanced tensile superelasticity both at 25 °C and 35 °C (about 10 °C above the A_f temperature), recovering about 4% and 6% strain, respectively. The stresses required to initiate martensitic transformation were determined as 300 MPa and 400 Mpa at 25 °C and 35 °C, respectively. To the best of the authors' knowledge, this is the first time in SMA

literature that an AM NiTi SMA reaches the end of the stress plateau during tensile loading up to 5% and continues with the elastic deformation of the detwinned martensite up to 6% strain.

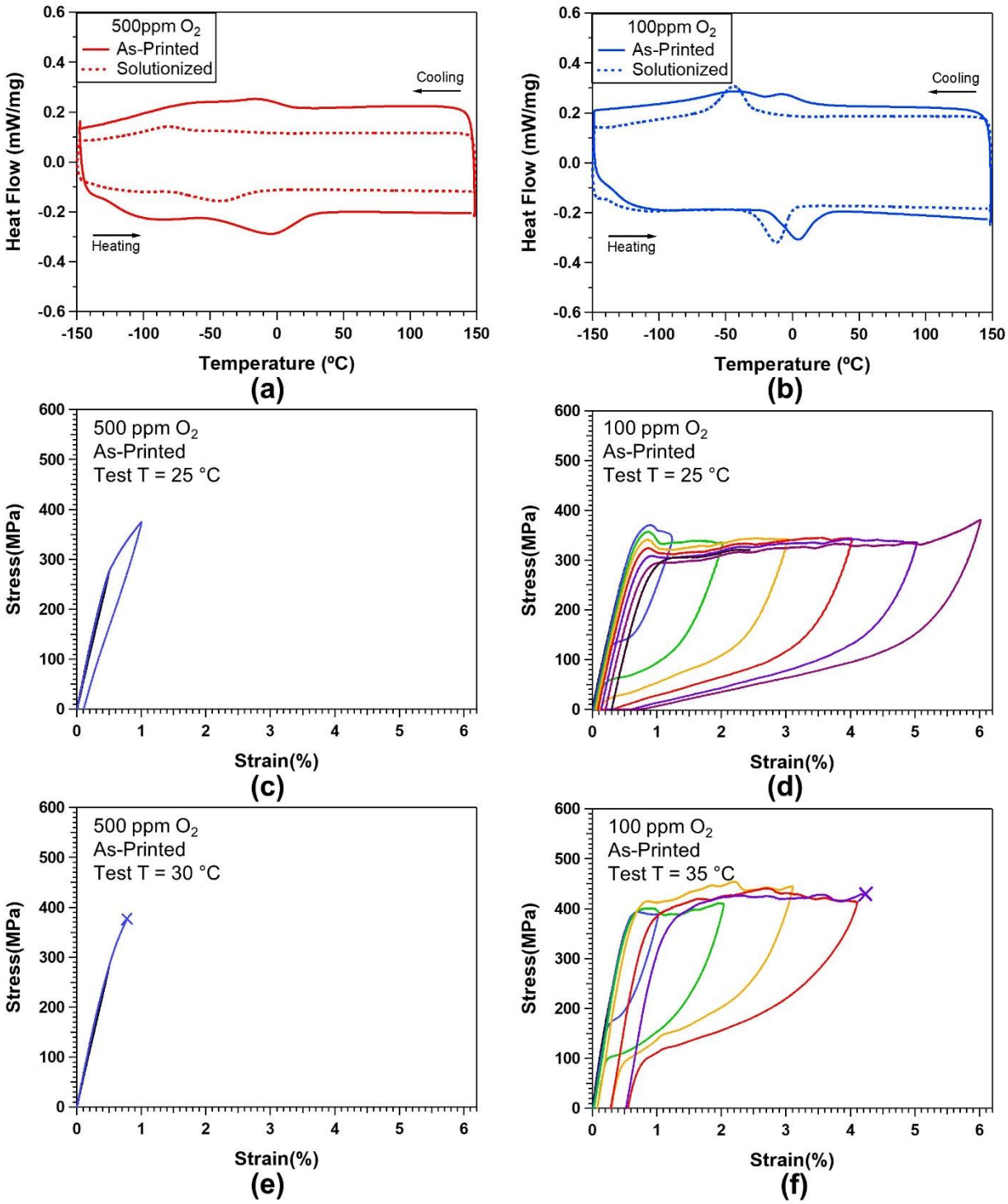

Figure 4.6 DSC thermograms of $Ni_{51.2}Ti_{48.8}$ samples extracted from rectangular prisms printed with the processing parameters (P,v,h) = (240W, 1.58m/s, 24µm) at (a) 500 ppm and (b) 100 ppm build chamber O_2 concentration. Incremental loading-unloading test

results of the tensile specimens extracted from the prism printed at 500 ppm, test conducted at (c) 25 °C and € 30 °C. Incremental loading-unloading test results of the specimens extracted from the prism printed at 100 ppm, test conducted at (d) 25 °C and (f) 35 °C.

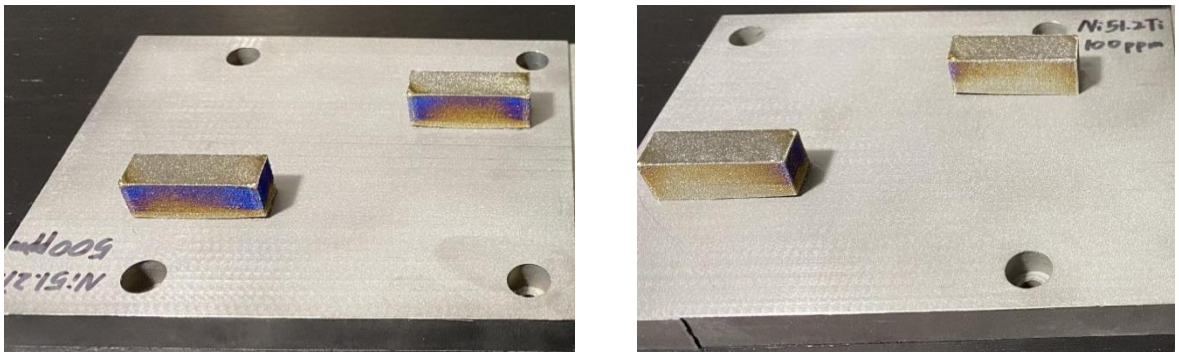

(a) **(b)**

Figure 4.7 (a) Rectangular prisms (Prism #1) of $Ni_{51.2}Ti_{48.8}$ samples printed with the processing parameters (P,v,h) = (240W, 1.58m/s, 24μm) in a build chamber with 500 ppm. (b) Same processing parameters were used to print another set of prisms (Prism #2) at a build chamber O_2 content of 100 ppm.

Based on the stress-strain response of S100 material at different temperatures (Figure 4.8a), the temperature dependence of the critical stress to induce martensitic transformation was calculated as 9.3 MPa/°C (Figure 4.8b). It should be noted that the sample failed before reaching 1% strain when tested at 50 °C, after undergoing 4 loading cycles to 1% strain at lower temperatures.

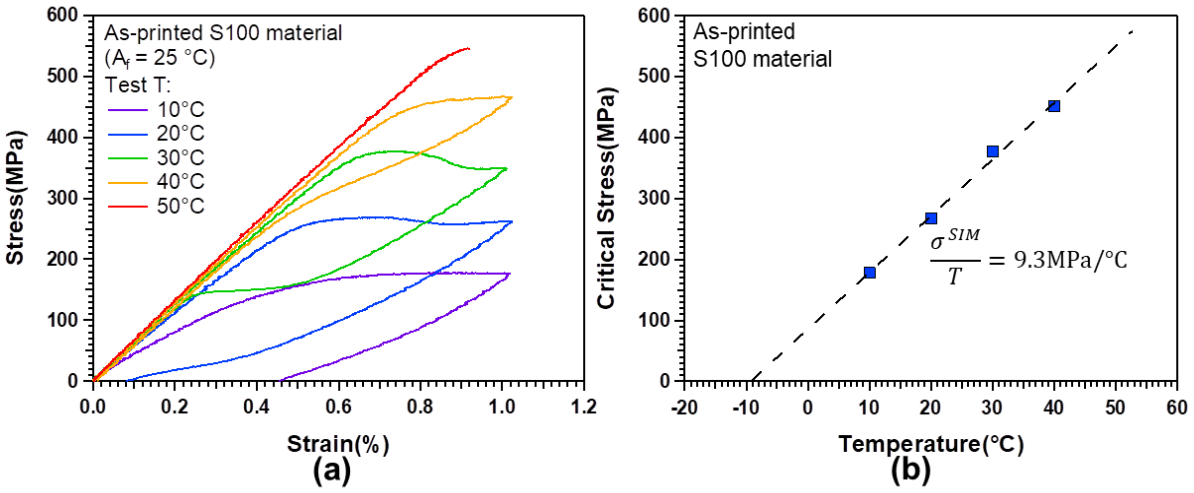

Figure 4.8 a) Tensile stress-strain responses of the $Ni_{51.2}Ti_{48.8}$ specimens printed at 100 ppm build chamber O_2 concentration (S100) upon loading to 1% strain and unloading at different testing temperatures. b) Temperature dependence of the critical stress to induce martensitic transformation was determined as 9.3 MPa/°C.

Based on Archimedes' density analyses, the measured densities are 6.452 g/cm^3 and 6.453 g/cm^3 for S100 and S500 materials, respectively, which are about 99.5% of the theoretical density (6.4816 g/cm^3) of $Ni_{51.2}Ti_{48.8}$ calculated based on an austenite lattice parameter of a_0 = 3.0127 Å from XRD results in Section 3.4. $Ni_{51.2}Ti_{48.8}$ nominal matrix composition was predicted from the transformation temperatures of the solutionized S100 material (Figure 4.6b) using the M_s dependence of transformation temperatures on Ni content as described in [62]. As shown in Figure 4.9, the SEM images of the cross-sections parallel to the build direction also indicate that both S100 and S500 parts are almost fully dense. The small number of observed pores (Figure 4.9c) have diameters smaller than 10 μm, and these pores could be a result of hollow particles

in the as-received powder, that have been previously reported in NiTi powder fabricated using gas atomization [44].

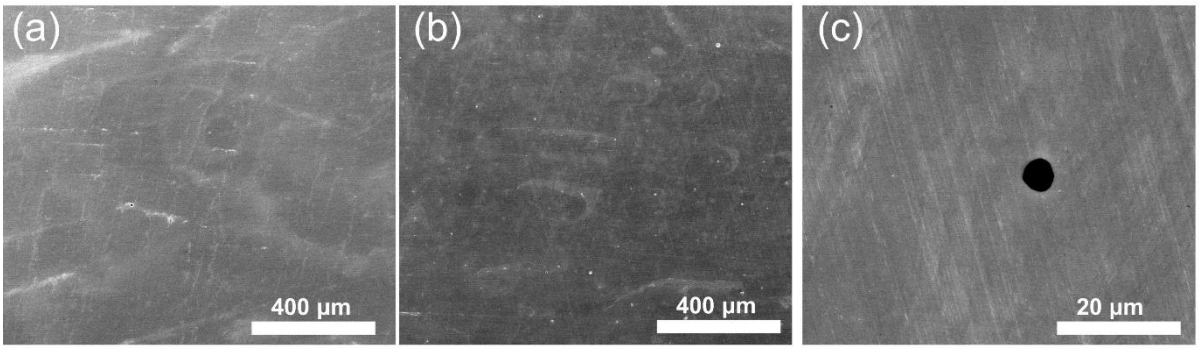

Figure 4.9. SEM images of the cross-sectional surfaces of the $Ni_{51.2}Ti_{48.8}$ specimens cut parallel to the build direction in (a) S500 and (b) S100 samples. (c) A pore with a diameter less than 10 µm detected in the S100 material, possibly resulting from the hollow particles in the as-received powder.

Processing parameters *P* and *v* were systematically varied based on a previously developed process-optimization framework [32, 86, 87] and *h* was selected based on a maximum hatch spacing criterion for the fabrication of defect-free parts from a Ni-rich NiTi SMA powder feedstock [86]. 66 single tracks were printed to be able to select the optimal single track parameters that will yield a continuous melt pool with desired depth and ideally avoid porosity resulting from keyholing, lack of fusion and balling phenomena. It is well known that the selection of a sufficiently small *h* can ensure the overlap and remelting of the adjacent tracks, while energy input, i.e. the volumetric energy density (VED), controls the extent of Ni evaporation from the molten powder [86], hence the transformation temperatures of the printed part. As illustrated in Figure 4, optimal *P*-*v* combinations based on single tracks

along with *h* values determined from the maximum hatch spacing criterion was not able to avoid the macroscopic cracks in the printed parts and their delamination from the build surface of the substrate. It is possible that these defects stem from the high Ni content of the starting powder since, as mentioned previously, none of these defects were encountered when a less Ni-rich powder was used in a previous study [86]. However, in the same study, only partial superelasticity could be obtained in the printed parts due to the lack of strengthening mechanisms such as coherent Ni-rich precipitates and solid solution hardening from higher Ni contents. Therefore, a more Ni-rich powder was selected with the aim of forming Ni-rich precipitates and taking advantage of higher Ni contents towards solid solution hardening to strengthen the matrix and ultimately achieve superior superelasticity in the printed parts with a large recoverable strain. Smaller *h* values were utilized to increase VED and evaporate just enough Ni to achieve superelasticity near room temperature and to suppress macroscopic defects. It was shown that the cracks and delamination from the substrate were noticeably mitigated at higher VED values (Figure 4.5). Listed below are the possible reasons that the as-printed parts were not able to be fabricated defect-free without a necessary reduction in *h* values:

a. The gas atomization method used to fabricate the specific powder feedstock used in this study was reported to have notable internal pores within the powder particles [88] and this explains some spherical porosity observed in the final NiTi prints. Additionally, carbon contamination from the graphite crucible during the gas atomization process may limit the ductility and make the prints more prone to cracks and delamination.

b. The bidirectional scanning pattern with a 45° angle employed in this study may generate a large thermal gradient during printing and result in excessive residual stress [71, 89] within the NiTi parts.

c. At low VED values, the resulting matrix is more Ni-rich with the chances of precipitating out strengthening second phases and ending up with increased strength at the expense of ductility. In addition, it is well known for NiTi SMAs that the higher the Ni content, more brittle the material becomes [90]. The initiation of cracks from defects like pores or inclusions will most likely be easier, especially in the presence of residual stresses.

d. Increasing transformation temperatures were observed with increasing VED due to increased Ni evaporation, similar to the results presented in [86]. Even if the transformation temperatures of the parts printed at high VED values were slightly below room temperature, each layer of these parts may be able to transform back to the martensite under potentially graded residual stress during cooling and before the subsequent layer is printed. Martensitic transformation may help the relaxation of the residual stress introduced by the thermal gradient during the laser melting process. In contrast, in the absence of martensitic transformation, e.g. in parts built with lower VED values, residual stresses might cause cracks, warping and delamination problems.

O_2 level in the build chamber was shown to be critical for controlling the high temperature oxidation during the printing process, especially at elevated VED levels. O_2 control has already been reported to be critical for the mechanical properties for AM NiTi

and a lower chamber atmosphere O_2 content of 25 ppm, which is much lower than the 500 ppm required by ASTM F2063-05, was suggested by Wang et. al. [25] for improved tensile ductility. In the current study, tensile ductility was shown to dramatically increase and superelastic recovery could be achieved by solely decreasing the O_2 level in the chamber from 500 ppm to 100 ppm. TEM observations revealed that the size and volume fraction of oxide particles were smaller in parts built at a chamber O_2 content of 100 ppm compared to 500 ppm. Hence was the necessity to limit the chamber O_2 content at high VED levels for improved ductility. Depending on the capability of different L-PBF systems, O_2 content may be decreased even further, e.g. as low as 25 ppm as shown in the work of Wang et al. [25].

At high VEDs, not just the oxidation but also the residual stresses are expected to be higher due to larger thermal gradients inside the printed part. Warping may accumulate during the layer-by-layer building process under the residual stress, but the resulting strains may be accommodated via the martensitic transformation as discussed above. It is also likely that high VEDs increase the temperature of the currently printed layer and may help relieve the residual stresses stored in the previously built layers. As an alternative to increasing VED through a decrease in *h* values, it may also be possible to eliminate cracks and delamination in Ni-rich NiTi through using a more complex scanning pattern than the 45° bidirectional pattern used in the present study or employing a pre-heated substrate that will result in smaller thermal gradients.

It should be noted that the determination of the "good" printable region in the printability map in Figure 4.4c is, to some extent, conservative. During printing, the temperature of the region in the vicinity of the current single track may increase due to

thermal conduction, and the energy required to form a melt pool with a given depth might decrease. Therefore, the minimum requirement of $d > t$ (layer thickness) may be slightly relaxed, and it is indeed possible that fully dense NiTi parts can be fabricated in the "lack of fusion" region that is close to its upper boundary near the "good" printable region, especially with the selection of smaller hatch spacing values.

Unlike the conventional fabrication methods typically used for the fabrication of NiTi, e.g., vacuum induction melting, oxygen pickup during the layer-by-layer fabrication in L-PBF processes is much more critical as each of the many layers that comprise the part is prone to oxidation during printing depending on the atmospheric cleanliness of the printer chamber. Therefore, in addition to Ni evaporation, possible precipitation reactions and the unique AM defect structure as a result of rapid cooling, oxidation may also play a role in the evolution of transformation temperatures of AM NiTi based on different types of oxide particles observed in the TEM study. As most of these oxides, if not all, are Ti-rich due to the higher affinity of Ti towards oxygen, Ti is depleted from the matrix, tending to decrease the transformation temperatures at relatively higher VED values, countering the effect of Ni evaporation. The solutionized $Ni_{51.2}Ti_{48.8}$ (at. %) powder showed no sign of martensitic transformation within a temperature range of -150 °C to 150 °C (Figure 4.2d). During printing of rectangular prisms, the evaporation of Ni with the selection of appropriate processing parameters resulted in the appearance of transformation peaks within the same temperature range (Figure 4.6a and Figure 4.6b). When the DSC results of the solutionized rectangular prisms printed at 100 and 500 ppm O_2 are compared, it is observed that S100 material exhibits slightly higher transformation temperatures. This correlates well with the

assumption that increased oxidation leeches more Ti from the matrix, decreasing the transformation temperatures and TEM images in Section 3.6 indeed show a qualitative trend of increased area fraction and size of the oxide particles.

4.3 Phase Identification and Crystallographic Texture Analysis

S100 material was found to be mainly austenitic based on room temperature XRD analyses (Figure 4.10) confirming the DSC results. Although the M_s temperature of this material was below room temperature, low intensity peaks detected at $2\theta = 39.6°$ and 44.2°, which correspond to $(002)_{B19'}$ and $(020)_{B19'}$, respectively, may indicate the presence of small amount of martensite. It is observed from peak intensities of different crystallographic planes on surfaces extracted parallel and perpendicular to the build direction (Figure 4.10) that there is a strong texture in the as-printed part, which is actually expected and typical for AM NiTi [12].

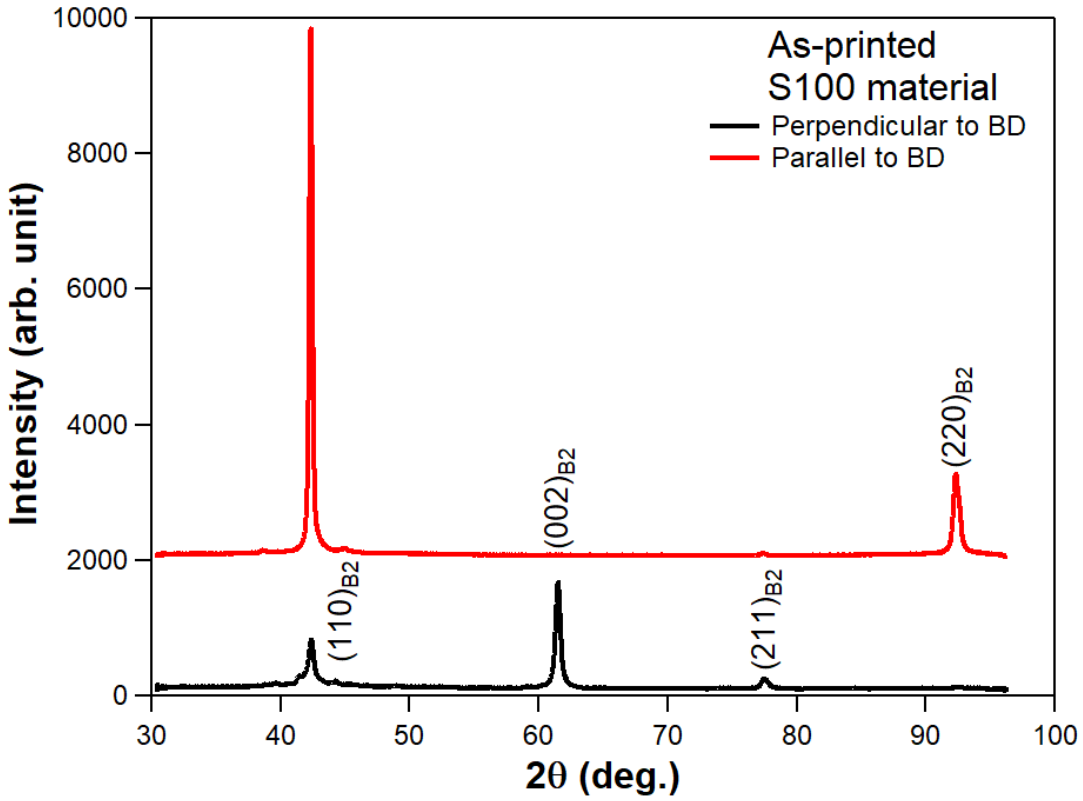

Figure 4.10 X-ray diffraction (XRD) patterns of the $Ni_{51.2}Ti_{48.8}$ rectangular prisms fabricated at 100 ppm build chamber O_2 content. Results are for the surfaces parallel and perpendicular to the build direction (BD).

As a detailed texture analysis at the microstructural level, EBSD analysis was performed on the S100 samples. Figure 4.11a shows an inverse pole-figure map constructed from the EBSD results for the plane perpendicular to the build direction (BD) with colors corresponding to the Z direction in the sample reference frame (IPF-Z). In this plane, a majority of the grains exhibit a <100> orientation perpendicular to the build direction (BD) in agreement with the XRD data in Figure 4.10. Figure 4.11b shows the IPF-Z map from a surface parallel to the BD. In agreement with the XRD results

shown in Figure 4.10, nearly all of the grains share a <110> orientation parallel to the BD. Formation of columnar grains along the BD is observed. The band contrast map in Figure 4.11c partially reveals the melt pools, and the elongated grains extend through several melt pool boundaries. The corresponding pole figures are shown in Figure 4.11d and Figure 4.11e for the samples with surfaces perpendicular and parallel to the BD, respectively. It is observed that the high-angle grain boundaries are wavy and a high fraction of low-angle grain boundaries is present. Higher magnification IPF maps along with KAM maps shown in Figure 4.12a and Figure 4.12b, respectively, allow one to investigate the local misorientation and geometrically necessary dislocation density. They reveal the high density of sub-structures in the NiTi sample.

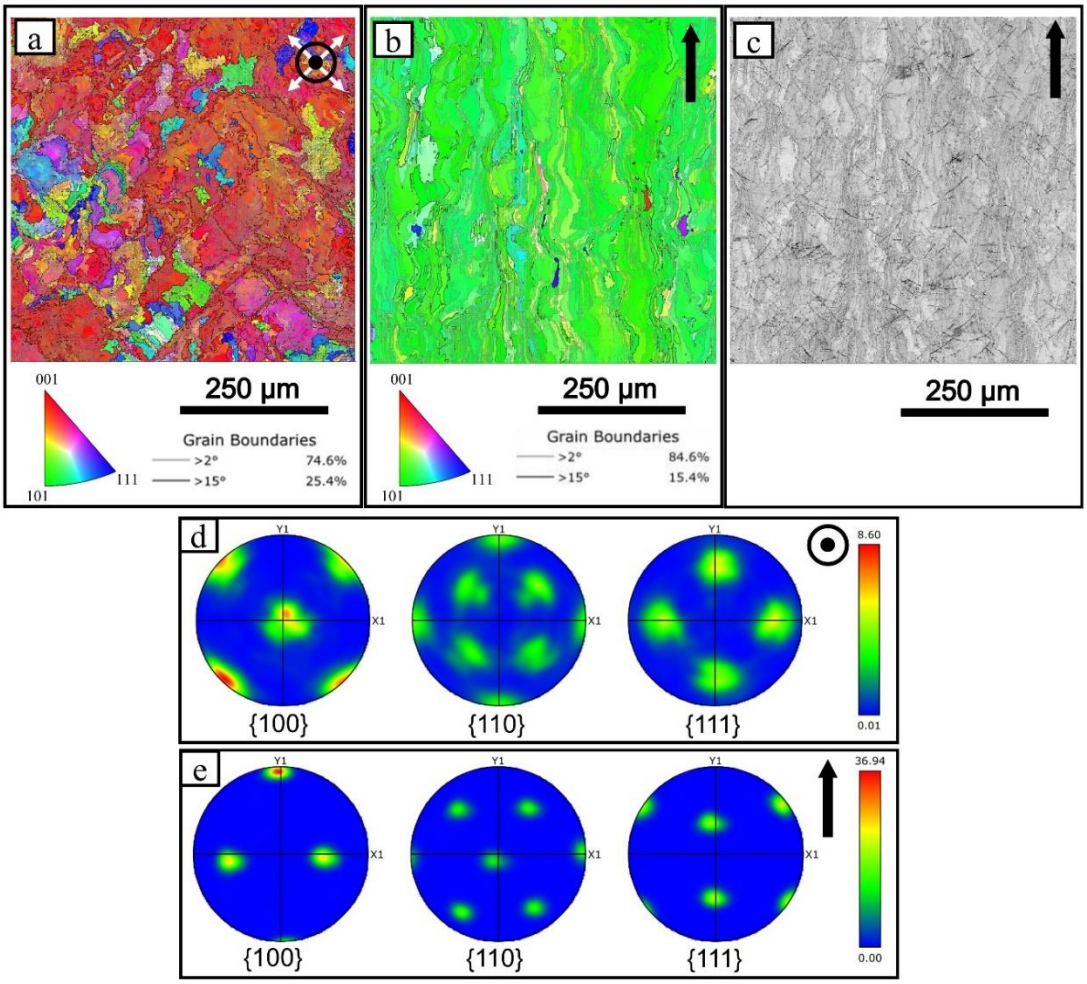

Figure 4.11 Large area electron backscatter diffraction (EBSD) orientation and inverse pole figure (IPF) maps (black lines show grain boundary (GB) misalignment larger than 15° and gray lines show GB misalignment larger than 2°) and corresponding pole figures for the cross-sections (a) (d) perpendicular and (b) (e) parallel to the build direction in the S100 samples of AM $Ni_{51.2}Ti_{48.8}$. (c) Band contrast map of the cross-section parallel to build direction partially revealing the melt pools. Black and white arrows represent the build direction and the scanning direction, respectively.

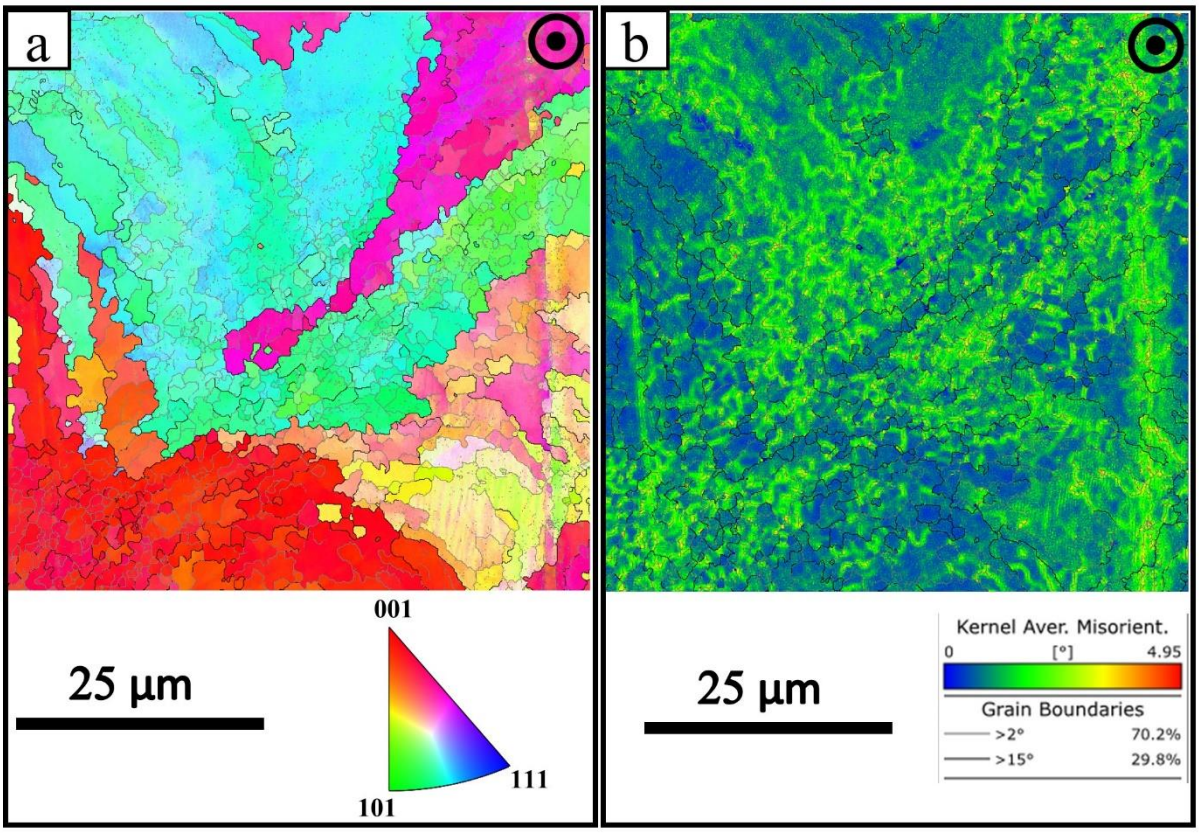

Figure 4.12 (a) Small area EBSD orientation and IPF map and (b) KAM map of the S100 material of AM $Ni_{51.2}Ti_{48.8}$ with the build direction out of the plane. 3 nearest neighbors are considered for the KAM map.

Crystallographic texture of the S100 material has been investigated and a strong <110> orientation has been observed along the loading axis of the dog-bone tension specimens extracted from the rectangular prisms (Figure 4.11e). Another notable observation is the formation of near pseudo single crystals in the printed NiTi samples (Figure 4.11). Due to the epitaxial growth in the layer-by-layer fabrication process, the columnar grains with similar orientations form a microstructure resembling a single crystal. In this section, we will discuss the effects of the process parameters selected

here, in particular the linear energy density (LED) which changes the melt pool shape, hatch spacing, and rotation angle of the laser tracks between the successive layers, on these two observed phenomena.

In the S100 samples, the [001] direction is aligned parallel to the build direction whereas the [100] and [010] directions are aligned parallel/perpendicular to the laser scanning directions (Figure 4.11d, Figure 4.11e, Figure 4.13a and Figure 4.13b). This texture and the loading direction of the tensile samples are some of the reasons why good tensile superelasticity was achieved in these samples, which is better than what is reported in the literature so far. It is well known that texture plays a major role on the thermomechanical response of NiTi SMAs. Gall et al. [91-93] have reported the mechanical properties of Ni-rich NiTi single crystals tested along different crystallographic orientations. The single crystals with <001> orientation along the loading axis exhibit higher critical stresses to induce martensitic transformation during tensile testing and premature fracture (at <2% strain), while the <110> orientations result in a high recoverable strains (>5%) with the martensitic transformation triggered at relatively lower tensile stresses (under the same aging conditions and test temperatures). Considering the premature fracture of the NiTi single crystals along the <001> orientation in tension [92, 93], the AM NiTi parts, especially the ones with higher Ni contents than equiatomic composition, should not have a strong <001> texture along the tensile axis for good superelastic performance.

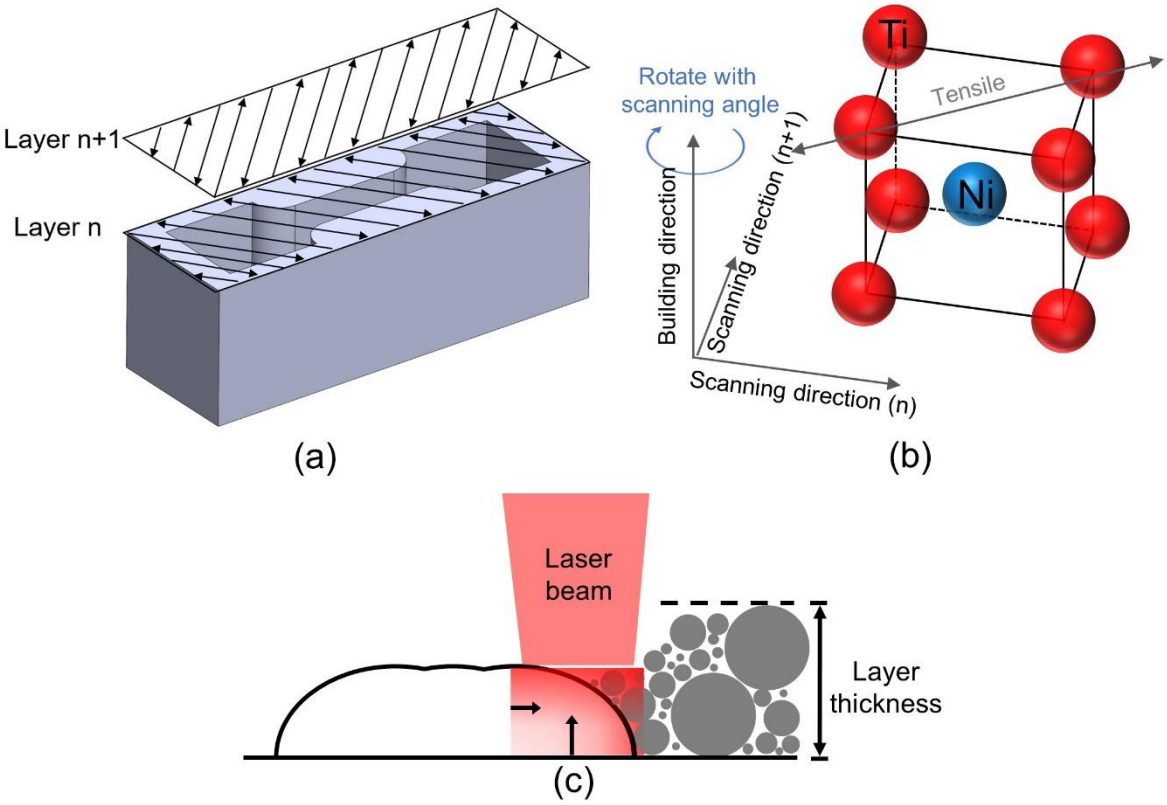

Figure 4.13 Schematic drawings of (a) scanning patterns and tensile specimen orientation in the AM $Ni_{51.2}Ti_{48.8}$ rectangular prisms in the present study, (b) B2 austenite lattice orientation with respect to the build direction and scanning directions in the AM samples based on the measured texture in Figure 4.11, (c) thermal gradient directions in the molten layer during the laser scan.

The <001> direction is the fastest crystal growth direction [94] along the highest thermal gradient during solidification of cubic materials, and the <001> growth textures have been reported in AM NiTi samples [12, 54, 95]. At first glance, the <001> texture along the build direction may seem to result from the high thermal gradient between the molten layer and the substrate or the previously printed layer (Figure 4.13c). However, considering the melting and solidification processes during the laser scanning process, there is also a large thermal gradient between the current laser track and the adjacent

previously solidified track. For example, it has been reported that hatch spacing (*h*) between the laser tracks affects crystallographic texture strength, smaller *h* values induce stronger textures in AM NiTi by increasing the number of remelting and solidification cycles, hence favouring the grain growth (forming pseudo single crystal structure) and better alignment of <001> orientation with the build direction [95, 96]. However, <011> orientation along the build direction has been reported in some other AM cubic materials (e.g., 316L stainless steel [97-99]) by using a rotation angle of 0° or 180° between the successive layers. Therefore, it is important to understand the underlying mechanisms of texture evolution during AM processes and utilize it as guidance to achieve desired textures in SMAs in order to accomplish near perfect superelasticity along different directions of the built parts. Yet, the texture studies on AM NiTi SMAs are limited [54, 95, 96, 100]. This is because of the difficulty of measuring the austenite texture (which is the relevant texture for the superelastic behavior) above room temperature which necessitates studying Ni-rich compositions with the austenite phase at room temperature. In addition, many of the earlier AM NiTi works were not able to achieve pseudo single crystals in Ni-rich NiTi compositions.

4.3.1. Effects of laser power and scan speed on crystallographic texture evolution. The shape of the melt pool may play an important role in the texture evolution during AM as it affects the direction of the local thermal gradient. As previously demonstrated with single track prints in Section 3.2, the melt pool geometry can change from a keyhole mode (Figure 4.14a) under a relatively high LED value (thus, high laser power or low scan speed) to a shallow shape (Figure 4.14b and Figure 4.14c) under low

LED values. At low LED values, the melt pool has a flatter bottom and is more likely to develop a <001> texture along the build direction as the thermal gradient is larger along the build direction. In our process optimization framework, the "good" tracks are defined conservatively with the criteria of $d<w/2$ for avoiding possible keyholing porosity (Figure 4.3c) and thus, they are likely to result in the development of <001> texture along the build direction.

Sun et al. [99] have reported that <011> orientation was aligned with the build direction in AM 316L steel. Their melt pool shape (as a result of the high LED values they used) can be defined as the keyhole type based on the process optimization framework presented above. Figure 4.14a schematically illustrates the melt pool shapes that Sun et. al. [99] observed when they achieved <011> texture along the build direction. This schematic also explains the mechanism proposed to rationalize the growth of <001> oriented grains 45° to the build direction due to the highest local thermal gradient direction perpendicular to the solid-liquid interfaces of the keyhole melt pools shown in the schematic. Figure 4.14b and Figure 4.14c also illustrate potential texture evolution mechanisms for low LED melt pool shapes. In short, Figure 4.14 explains a potential mechanism to control the texture during AM process based on the melt pool shapes through the control of LED value, and thus, laser power and scan speed.

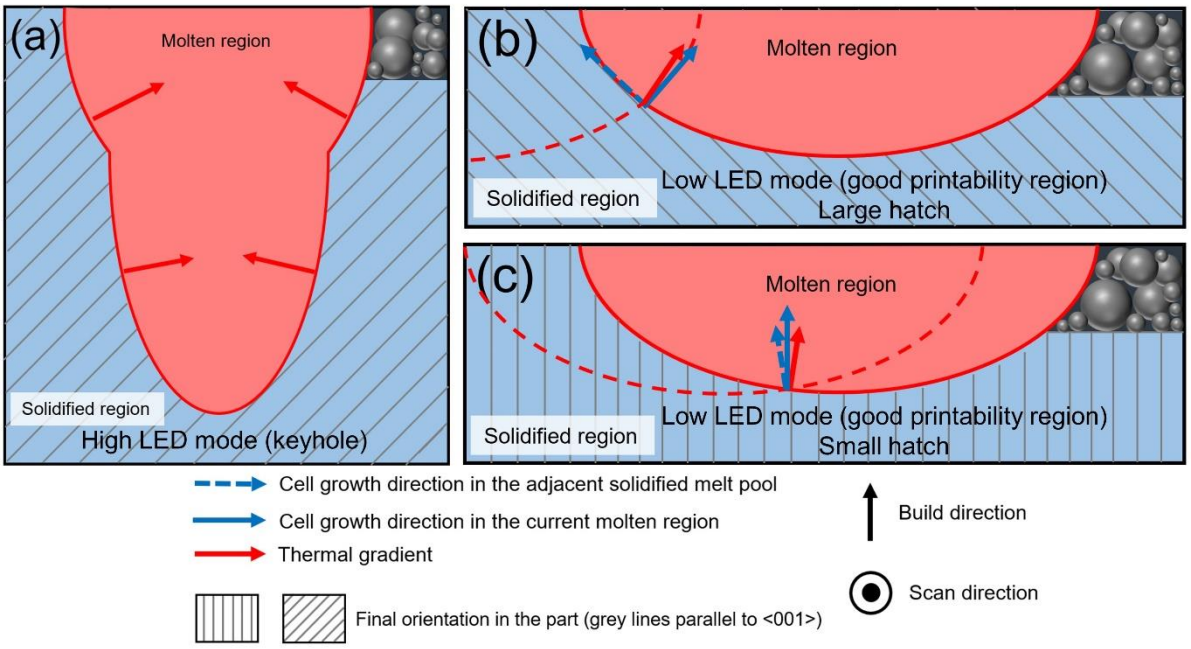

Figure 4.14 Schematic illustration depicting the thermal gradient and solidification direction under (a) high linear energy density (LED) (keyholing mode) [99], (b) lower LED (good print region in Figure 4.3) with large hatch spacing, and (c) lower LED (good print region) with small hatch spacing as used in the present study. The melt pool becomes shallower and flatter under lower LED, so the thermal gradient and solidification direction are mostly along the build direction in the present case with small hatch spacing, which results in the <001> texture formation in (c). Cell growth direction from the solid-liquid interface indicates <001> orientation formation since it is the fastest crystal growth direction for cubic materials. The schematics were constructed for the rotation angle cases of 0° or 180° between the successive layers.

4.3.2. Effects of hatch spacing on crystallographic texture evolution.

The value of *h* may also affect the texture in AM NiTi parts. Andreau et al. [97] proposed a mechanism for forming <011> texture along the build direction in 316L steel taking the effect of *h* into account. Based on this mechanism, the epitaxial growth at the overlap of the molten region with the previously printed track will favour the crystallographic orientation that has less misalignment for lowering the nucleation

energy of new nuclei, and the growth direction may have a small angular difference with the local thermal gradient (Figure 4.14b). As printing takes place, this orientation will gradually dominate the others. However, *h* used in our NiTi parts is very small (24 μm, a quarter of the melt pool width, Figure 4.14c), so the epitaxial growth can start from a flatter region in the mid-bottom of the melt pool. At the mid-bottom region of the previously (or the first) printed track will have a <001> orientation along the build direction, which is aligned with the thermal gradient during its solidification. As more tracks are printed, this orientation may be inherited and dominate others.

4.3.3. Effects of rotation angle between successive print layers on the crystallographic texture evolution.

The rotation angle of the scan directions between successive layers may also influence the resulting texture. As shown in Figure 4.15a, both <001> and <011> orientations along the build direction could be possible during a single layer scan depending on the melt pool shape and *h* value, as described in Figure 4.14. However, if a rotation angle of 90° is imposed between layers (Figure 4.15b), the <001> orientation would be preferred along the build direction since this orientation would perfectly match between the layers and have minimum misalignment. In addition, this orientation preference is more likely to be inherited from the previous layer during cell growth since the <011> orientation parallel to the build direction will have a large angular deviation of 90°. Several studies [98, 101, 102] have shown successful control of the texture orientation in the AM parts in materials other than NiTi with different rotation angles. Therefore, a similar texture control should be possible in AM NiTi parts as well.

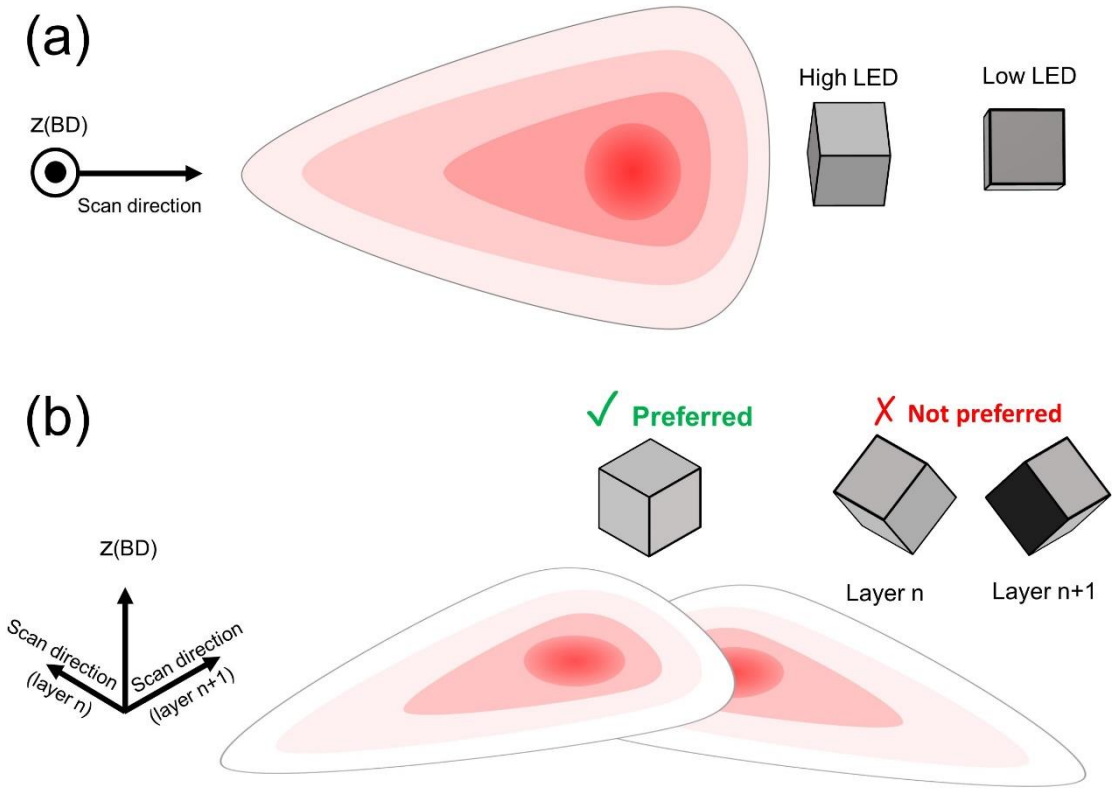

Figure 4.15 Schematic of the orientation selection/growth mechanism during (a) single-layer scanning (lattice cells were slightly rotated for better view) and (b) multi-layer scanning with a 90° rotation angle of scan directions. Both orientations would be possible for single-layer, but only the <001> would be favoured due to its less misalignment with the previous sintered layer for the multi-layer situation.

Evidently, the pseudo single crystal AM NiTi samples in the present study resulted from a combination of a shallow melt pool, a relatively small *h* value, and a 90° rotation angle between layers. Knowing the orientation selection/growth mechanism shall expand the scope of texture engineering in additively manufactured NiTi based SMAs as well as other materials with cubic crystal structure.

4.4 Microstructural Evolution

As shown with superelastic testing results in Figure 4.6, S100 material exhibited enhanced superelasticity, with the highest recoverable strain recorded in literature so far. On the other hand, S500 material failed in a brittle manner without showing any sign of superelasticity. TEM was performed to reveal the role of microstructural features, especially the presence of different types of non-metallic inclusions and precipitates, on the observed differences in the mechanical behavior of the as-printed NiTi samples.

TEM imaging revealed that both the S500 (Figure 4.16) and S100 (Figure 4.18) materials have qualitatively similar microstructures consisting of highly irregular grains with curved, wavy grain boundaries and a large amount of low angle grain boundaries. In addition, both conditions had a very high density of secondary phase particles. The microstructure of the S500 sample was inhomogeneous, with the distinct distributions of secondary particles varying from one area to the next. As shown in Figure 4.16a there were regions of the specimen containing 20-50 nm spherical particles that had no clear preferred orientation relative to the surrounding matrix. The background filtered high resolution TEM (HRTEM) image and corresponding fast Fourier transform (FFT) shown in Figure 4.16c and Figure 4.16d are representative of these particles.

In addition, there were large regions of the S500 specimen that contained networks of < 20 nm particles that appeared similar to subgrain networks, as shown in Figure 4.16b. The HRTEM and selected area electron diffraction (SAED) shown in Figure 4.16e and Figure 4.16f reveal a clear orientation relationship between these

particles and the matrix. However, the d-spacings observed do not match well with any of the known secondary phases in NiTi including pure and mixed oxides. STEM - High-angle annular dark-field imaging (HAADF) and STEM-EDS (Figure 4.17) indicate that both types of particles contain oxygen and are poor in Ni relative to the matrix.

Similar to the S500 specimens, the S100 samples also contained two distinct distributions of secondary phase particles. As shown in Figure 4.18a and Figure 4.18b, some areas of the specimen contained randomly distributed spherical particles, while other regions showed a network of particles. HRTEM revealed that there were very fine (<15 nm), randomly distributed coherent particles present in addition to the larger particles shown in Figure 4.18a. A representative particle and the corresponding FFT are shown in Figure 4.18c and Figure 4.18d, respectively. The d-spacings observed in Figure 4.18d do not match well with any of the expected secondary phases, but HAADF imaging of this region indicates that these nm-scale precipitates are Ni-rich, as shown in the STEM-HAADF image in Figure 4.19a. Unlike in the S500 specimen, as shown in Figure 4.18e and Figure 4.18f, the networked particles do not have a clear preferred orientation. As shown in Figure 4.19, STEM-HAADF and STEM-EDS confirm that both the networked particles and the larger, spherical particles are Ti-rich oxides, similar to what was observed in the S500 specimen.

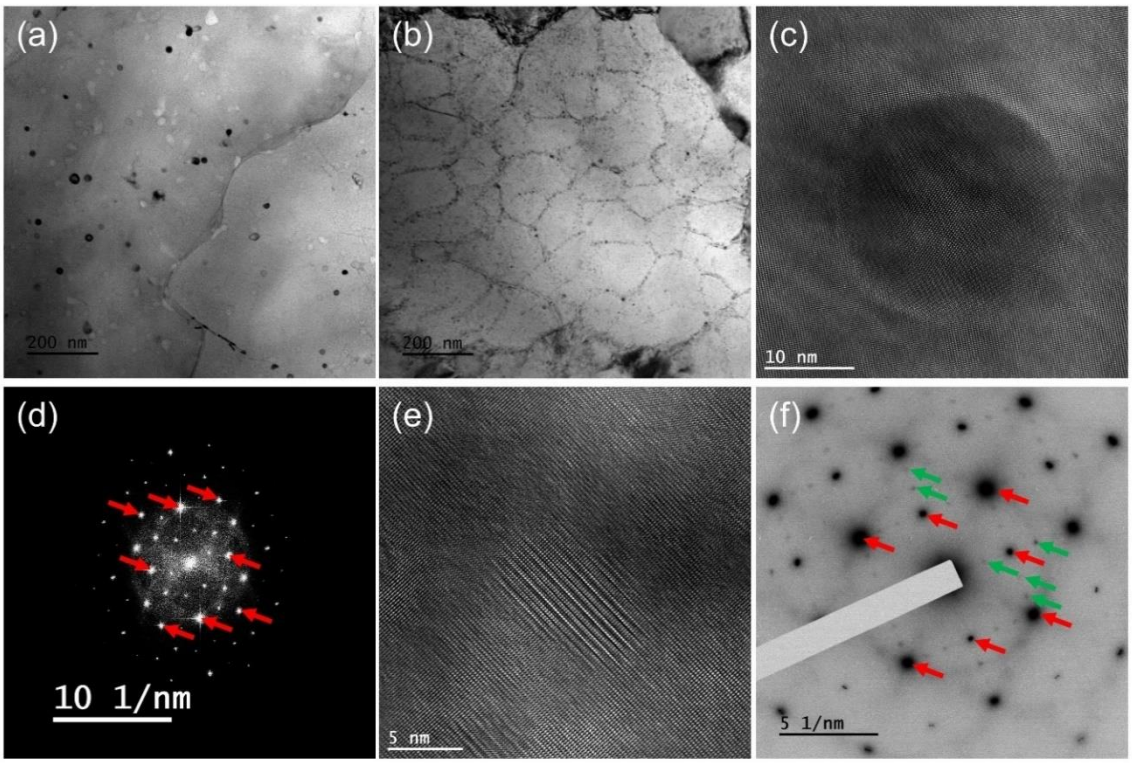

Figure 4.16 TEM micrographs representative of the distribution and structure of secondary phases in the S500 samples of AM $Ni_{51.2}Ti_{48.8}$. (a) A bright Field (BF)-TEM image showing region with randomly distributed, spherical particles. (b) Another BF-TEM image showing region with networked, non-uniformly shaped particles. (c) Absolute background filtered HRTEM showing a spherical particle. (d) FFT of (c) with [110]-oriented NiTi austenite matrix reflections indicated by red arrows. (e) Absolute background filtered HRTEM showing a coherent particle representative of the networked particles shown in (b). f) The selected area electron diffraction (SAED) image from an area with networked particles with [100]-oriented NiTi austenite matrix reflections indicated by red arrows and secondary phase reflections indicated by green arrows.

While it is difficult to quantify the particle density due to the unknown thickness of the samples and the variation in visibility of particles due the various orientations present, the line-intercept method was used to determine the network spacing in both conditions. The mean network spacing for the S500 specimens were 104.1 nm, whereas

for the S100 specimens it was 127.6 nm, indicating a higher volume of oxide particles in the S500 specimens.

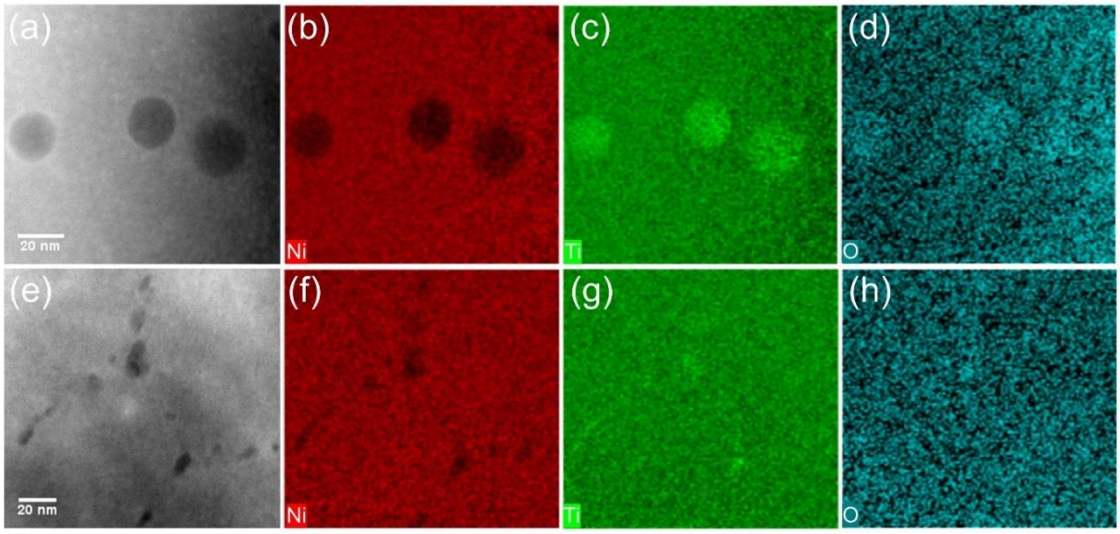

Figure 4.17 STEM-HAADF and EDS maps of (a-d) spherical secondary phase particles and (e-h) networked particles in the S500 samples of AM $Ni_{51.2}Ti_{48.8}$. (a & e) HAADF images with brightness proportional to atomic mass. (b & f) at. % Ni maps. (c & g) at. % Ti maps. (d & h) at. % O maps.

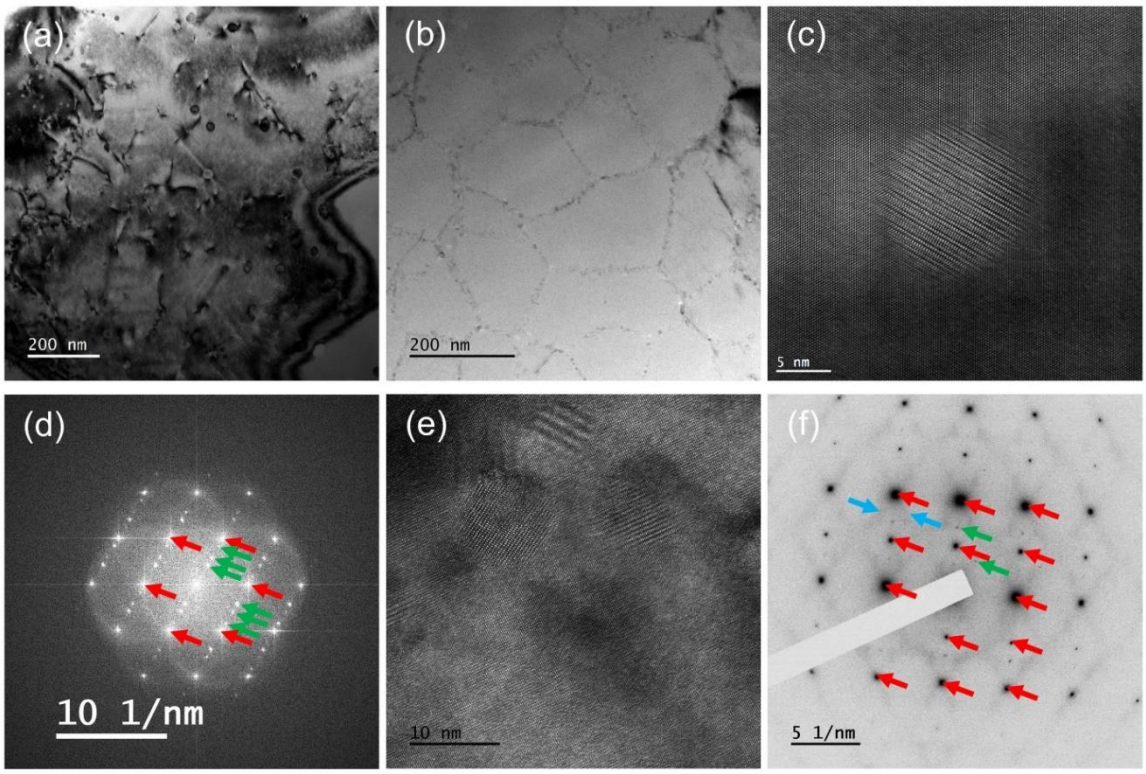

Figure 4.18 TEM micrographs representative of the distribution and structure of secondary phases in the S100 samples of AM $Ni_{51.2}Ti_{48.8}$. (a) A BF-TEM image showing region with randomly distributed, spherical particles. (b) Another BF-TEM image showing region with networked, non-uniformly shaped particles. (c) Absolute background filtered HRTEM image showing a 14 nm diameter, coherent particle. (d) FFT of (c) with [111]-oriented NiTi austenite matrix reflections indicated by red arrows and secondary phase reflections indicated by green arrows. (e) Another HRTEM image showing several particles of different orientations representative of the networked particles shown in (b). (f) SAED from an area with networked particles with [110]-oriented NiTi austenite matrix reflections indicated by red arrows and secondary phase reflections indicated by green arrows. Blue arrows highlight streaking observed in the pattern indicating a potential range of lattice parameters in the secondary phase particles present.

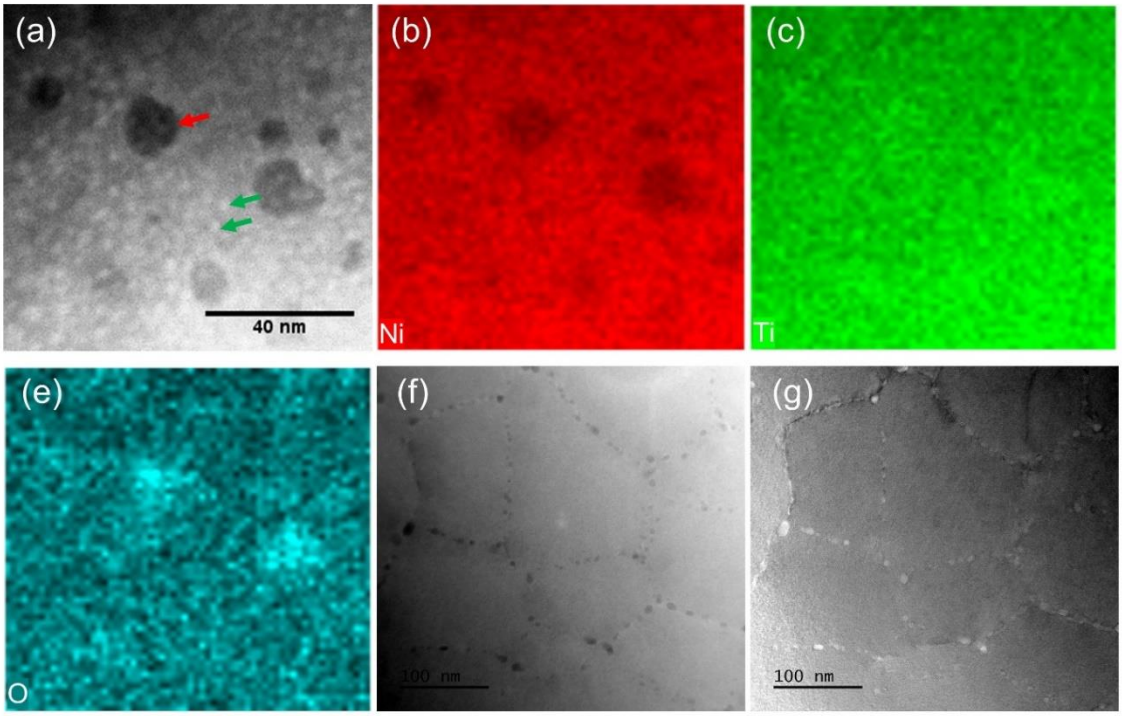

Figure 4.19 STEM images and EDS maps showing secondary phase particles in the S100 samples of AM $Ni_{51.2}Ti_{48.8}$. (a) A HAADF image showing larger, Ni-poor oxide particles like the one indicated by the red arrow and smaller, Ni-rich particles like those indicated by the green arrows. (b) at.% Ni map corresponding to (a). (c) at.% Ti map. (d) at.% O map. € A HAADF image of the region containing networked, Ni-poor oxide particles. (f) The STEM-BF image of the region shown in €.

As observed from the TEM images presented in this section, it is clear that the build chamber O_2 level plays an important role in the formation of Ti-rich oxides. It is also likely that the high VED values (198 J/mm^3) employed in this study exacerbated the oxidation as observed from the colored oxide layer formed on the rectangular prisms (Figure 4.7).

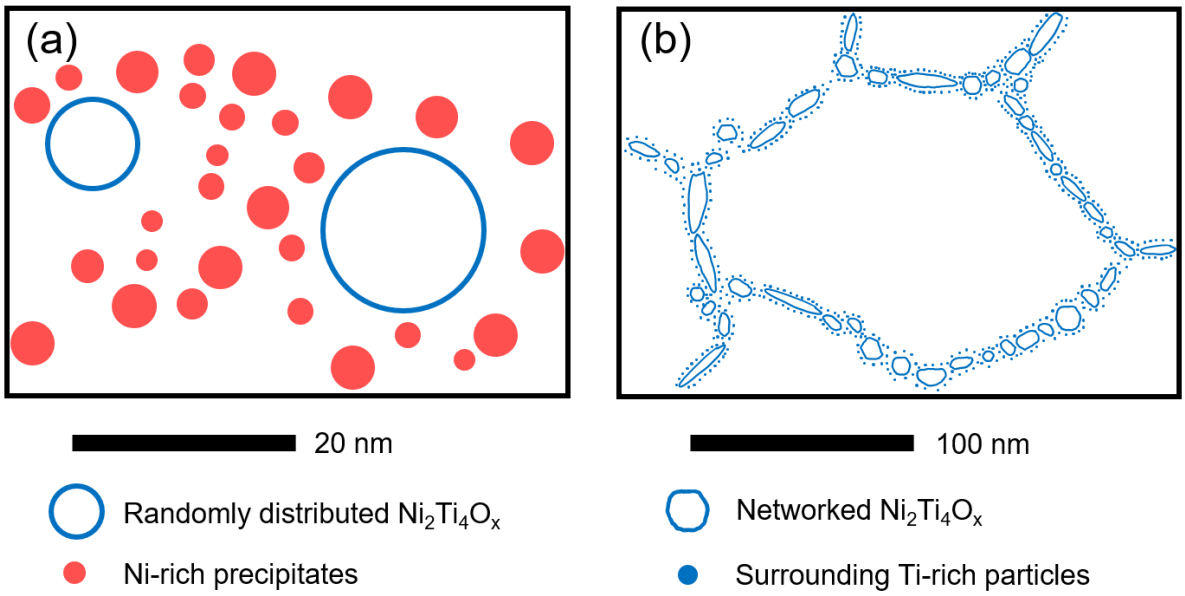

Figure 4.20 Schematic of the precipitates and non-metallic inclusion particles observed in AM NiTi samples in this study. (a) Randomly distributed Ti-rich oxides surrounded by Ni-rich precipitates; (b) networked Ti-rich oxides surrounded by Ti-rich particles.

As shown in Figure 4.20, there are four types of particles observed in the AM NiTi samples based on the TEM study. Ultrafine Ni-rich precipitates (with a size range of 2-4 nm) were identified in the S100 material around the randomly distributed Ti-rich oxides in the grain interior. The depletion of Ti from the matrix due to the formation of Ti-rich oxides has dual effects: first, it increases the Ni/Ti ratio in the matrix, hence decreasing the transformation temperatures; second it promotes the formation of Ni-rich precipitates. Coherent nanosized Ni_4Ti_3 precipitates are known to strongly influence the mechanical and shape memory properties of NiTi SMAs such as transformation temperatures [103], appearance of the intermediate R-phase transformation [104], functional and structural fatigue [93] and superelasticity [56, 105, 106]. In addition, the nano-oxides should generate elastic strain fields in the surrounding area and serve as

preferential nucleation sites for martensite at interfaces. All these nanosized particles strengthen the matrix by acting as barriers against slip deformation and potentially suppress the irreversibility associated with the martensitic transformation. It is likely that the presence of nanosized particles in the present AM samples (in addition to favourable crystallographic texture) resulted in the good superelastic behavior. On the other hand, there is a notably higher volume fraction of oxide particles in the S500 samples, resulting in the inferior ductility and premature failure during the tension tests.

So far, there are only a few studies showing the existence of Ni_4Ti_3 type precipitates in AM NiTi in the as-printed condition [107, 108]. It is possible that the repetitive thermal cycling during the AM process is too fast to have enough time and preferable temperature for the growth of Ni-rich precipitates. It is also likely that the Ni-rich precipitates may be dissolved during the melting of subsequent layers. To the best of authors' knowledge, this is the first time that ultrafine Ni-rich precipitates with a size range of a few nanometres were identified in AM NiTi SMA. Most importantly, the highest superelastic strain achieved in this study is more than the double of what has been reported in the literature for AM NiTi (Figure 4.21).

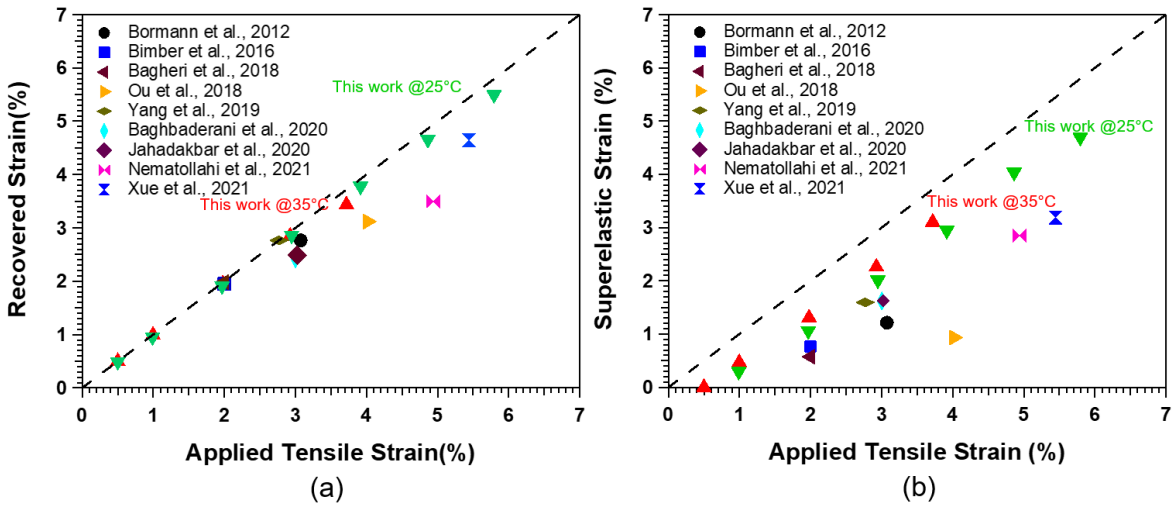

Figure 4.21 Comparison of the tensile superelastic strain levels achieved in AM NiTi samples in the present work in comparison with what is reported in the literature so far.

Based on the thermal diffusivity measurements, neither build chamber O_2 level nor the measurement direction were found to have a significant impact on thermal conductivity values. Therefore, superelastic strain in AM NiTi can be increased as demonstrated here

without a detrimental effect on thermal transport properties. Additionally, part orientation during printing does not have to be considered in order to optimize thermal transport, since thermal transport properties were not found to be anisotropic. Nevertheless, as a future work, a thorough systematic study is needed to evaluate the effects of different processing parameters on thermal transport properties to be able to fully implement AM NiTi parts in applications where the knowledge of thermal conductivity is significant, e.g. in the case of actuation applications, with the cycle time dependent on how quickly the SMA can cool down; or elastocaloric applications, where the heat absorbed or released during stress induced martensitic transformation should rapidly be transferred between different media for increased operation frequency.

4.5 *Thermophysical Properties*

The specific heat capacities of the S100 and S500 materials were measured to be 0.43 and 0.44 J/g·K respectively, showing good agreement with specific heat capacity values of NiTi SMAs reported in the literature [66]. Thermal conductivity of samples is plotted against temperature in Figure 4.22. In Figure 4.22a, the thermal conductivity measured parallel to the build direction (with heat flux along the normal to the plane of the substrate surface) is shown for both the S100 (open circles) and S500 (solid squares) samples. Each data point represents the average of the thermal conductivities measured in seven samples taken from varying heights within the as built prisms. Although there was some scatter among the thermal conductivities measured at different build heights (indicated by the 1-standard deviation error bars) there was no trend with respect to build height in either the 100 ppm or 500 ppm samples. Furthermore, there was little

difference in thermal conductivity between the 100 ppm and 500 ppm samples as indicated by the proximity of the corresponding curves in Figure 4.22, the thermal conductivity measured perpendicular to the build direction (with heat flux direction within the plane of the build plate surface) is plotted against temperature for the 100 ppm and 500 ppm samples, where each data point represents the average thermal conductivity measured in three samples. Although the average thermal conductivity of the 100 ppm samples is lower than that of the 500 ppm samples, significant spread in the 500 ppm data suggests that the difference may not be statistically significant, as shown by the overlapping error bars between the two curves. In order to determine whether the measurement direction or build chamber O_2 level have a statistically significant effect on the thermal conductivity of the printed material, t-tests were performed on the 55 °C data points using 95% confidence intervals (significance level $\alpha = 0.05$). In each case, the resulting p-value was greater than the significance level, indicating that the observed differences in thermal conductivity are not statistically significant. Therefore, it cannot be concluded that build chamber O_2 level or measurement direction has an effect on the thermal conductivity.

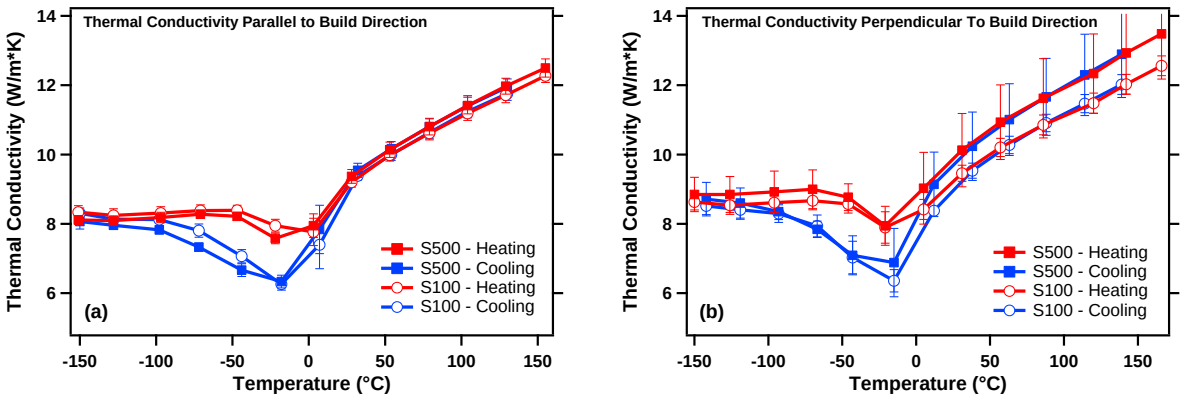

(a) **(b)**

Figure 4.22 Thermal conductivity of AM $Ni_{51.2}Ti_{48.8}$ measured (a) parallel to the build direction and (b) perpendicular to the build direction. Measurements taken from S100 material are represented by the blue curves, and those taken from S500 material are represented by the green curves. The error bars correspond to one standard deviation above and below the average value.

Regardless of measurement direction and build chamber O_2 level, the thermal conductivity curves show similar behavior with changing temperature. Upon heating from -150 °C, thermal conductivity increases slightly and subsequently dips during reverse martensitic transformation. The austenite phase shows higher thermal conductivity as well as increased sensitivity to temperature increase compared to the martensite phase. As the samples were cooled down through martensitic transformation, thermal conductivity dipped significantly lower than during the reverse transformation. The thermal conductivities in both the martensite and austenite phases are lower compared to the thermal conductivity measured in bulk $Ni_{50}Ti_{50}$ [109]. At temperatures of -100 °C and 100 °C representing the martensite and austenite phases respectively, bulk $Ni_{50}Ti_{50}$ showed thermal conductivities of approximately 12 and 16 W/m·K [109],

whereas the AM Ni-rich NiTi of the present study showed average thermal conductivities of approximately 8.5 and 11.5 W/m·K. This difference in thermal conductivity may be attributed to the differing composition and the unique microstructure of AM NiTi with increased number of defect sources, e.g., non-metallic inclusions, precipitates and increased dislocation density, acting as phonon scattering centers. Further investigation is needed to isolate the effects of compositional and microstructural effects on the thermal conductivity of AM NiTi SMAs.

4.6 Summary

In this Chapter, highly textured Ni-rich NiTi SMA parts were successfully fabricated without notable porosity or microcracks using the L-PBF technique and tensile superelasticity values up to 6% could be achieved through the selection of optimal processing parameters and formation of nanosized precipitates and oxide inclusions. The following summary statements and conclusions can be drawn:

CHAPTER V

SUMMARY OF RESULTS, CONCLUSIONS AND SUGGESTIONS FOR FUTURE WORK

5.1 Results and Conclusions

1. For $Ni_{51.1}Ti_{48.9}$ (at. %) and $Ni_{50.3}Ti_{49.7}$ (at. %), fully dense NiTi parts were successfully fabricated using several different combinations of processing parameters in a large region of the processing parameter space. Porosity was detected in parts that were printed with processing parameters positioned near keyholing or lack of fusion defect boundaries on the constructed optimum printability map following the framework. This was attributed to a possible shift of the defect boundaries due to heat accumulation while printing 3D parts. A proper keyholing criterion has been identified for these NiTi SMAs to eliminate the porosity near these boundaries.
2. The transformation temperatures of the NiTi parts, fabricated using $Ni_{50.8}Ti_{49.2}$ (at. %) powder, increase almost monotonically with the volumetric energy density (VED) used for printing due to the Ni evaporation during the melting process. Hence it is possible to precisely tailor the chemical composition and the functional properties of Ni-rich NiTi SMAs by varying the processing parameters. The amount of Ni evaporation as a function of VED was calculated using the measured transformation temperatures, which exhibits an impressively good correlation with VED. On the other hand, transformation temperatures of

parts fabricated using the $Ni_{50.1}Ti_{49.9}$ (at. %) powder only changed minimally due to the insensitivity of transformation temperatures for Ni contents below 50 at. %.

3. As-printed NiTi specimens exhibited tensile ductility up to 16%. This is a remarkable value compared to literature results considering the fact that a simple scanning strategy was used, and the oxygen level in the building chamber was at 500 ppm during printing. This was attributed to consistently achieving fully dense parts in the optimum printability region of the process parameter space.
4. As-printed NiTi specimens also showed good shape memory effect and superelasticity. Up to 6% strain could be recovered in shape recovery tests, and 4% superelastic strain was achieved in NiTi parts fabricated using the $Ni_{50.8}Ti_{49.2}$ (at. %) powder. Superelasticity levels slightly improved after an aging heat treatment at 400 °C for 1h. The complete superelasticity was not achieved due to the Ni evaporation and the lack of a sufficient amount of excess Ni in the matrix to precipitate out enough Ni_4Ti_3 precipitates.
5. Crack and delamination issues observed in the printed parts ($Ni_{51.2}Ti_{48.8}$, at. %) may originate from the residual stresses generated due to the large thermal gradients during printing, and they were mitigated by using smaller hatch spacing and higher VED values. It is possible that with increased transformation temperatures and the initiation of the martensitic transformation when the printed parts cool down, residual stresses might be relaxed.

6. O_2 control of the atmosphere in the chamber was also found to be critical for the ductility of the printed parts and the achieved superelasticity levels. O_2 concentration of 500 ppm led to the parts ($Ni_{51.2}Ti_{48.8}$, at. %) that failed in a brittle manner at low strains without showing any sign of superelasticity, while decreasing the O_2 concentration to 100 ppm yielded parts ($Ni_{51.2}Ti_{48.8}$, at. %) that exhibit show 6% superelastic strain without any post fabrication heat treatment, which is the highest reported to date in literature.
7. The unique AM microstructure with strong texture, the presence of nano-sized inclusions and ultrafine Ni-rich precipitates in $Ni_{51.2}Ti_{48.8}$ (at. %) suggest a possible approach for achieving high levels superelasticity in AM NiTi in the as-fabricated condition. Thermal history during the process needs to be further studied in order to provide the ideal conditions for the growth of Ni-rich precipitates, otherwise post heat treatments may be necessary for the achievement of superelasticity.
8. The strong favorable crystallographic texture in the as-printed tension samples ($Ni_{51.2}Ti_{48.8}$, at. %) indicated that the superelastic properties are orientation dependent.
9. Thermal conductivity values of the as-printed NiTi were found to be independent of the build chamber O_2 level, in the range studied in the present study, or orientation of the part. As a future work, a more detailed study is required to characterize the effects of processing parameters such as laser power, scan speed

and hatch spacing for a complete understanding of the relationship between microstructure and thermal transport properties in AM NiTi.

5.2 Future work

Based on the results and findings of this research, several recommendations are made for future studies.

1. In addition to composition, a detailed study could be performed on powders with different particle size distribution to understand its effect on the quality and functional properties of the NiTi prints. The impurity (e.g., oxygen and carbon) level of the powder shall also be characterized to ensure repeatability.
2. The transformation temperatures of the NiTi prints were observed to increase with increasing VED or evaporation of Ni. However, the transformation temperatures were observed to shift differently before and after solution heat treatment. Microstructural study on different NiTi prints from a given powder could be performed to understand the precipitation evolution and other effects (e.g., residual stress and dislocation density) in additive manufacturing NiTi. This could further help with the prediction of the functional properties for a given sets of parameters in the as-printed NiTi.
3. Functional or compositional graded NiTi can be additive manufactured using the findings from this work.

4. Further engineering the texture in additive manufactured NiTi may favor better mechanical properties (i.e. strength and superelasticity level) for the near-net-shape fabrication of complex functional NiTi parts.
5. The variability and repeatability shall be investigated for additive manufactured NiTi. And the effect of using recycled powder shall also be studied.
6. NiTi shape memory alloy parts with complex geometries shall be fabricated and tested to validate the process optimization framework in this work. Functional and texture gradient can also be applied to explore their potential in application.
7. Post-processing (e.g., post-process heat treatment and electropolishing and) shall be investigated to improve the properties and quality of the additive manufactured NiTi parts. And their corrosion resistance needs to be evaluated.

REFERENCES

[1] E. Kaya, İ.J.T.I.J.o.A.M.T. Kaya, A review on machining of NiTi shape memory alloys: The process and post process perspective, 100(5) (2019) 2045-2087.

[2] H. Lin, K. Lin, Y.J.J.o.m.p.t. Chen, A study on the machining characteristics of TiNi shape memory alloys, 105(3) (2000) 327-332.

[3] K. Weinert, V.J.M.s. Petzoldt, e. A, Machining of NiTi based shape memory alloys, 378(1-2) (2004) 180-184.

[4] K. Malukhin, K. Ehmann, Material characterization of NiTi based memory alloys fabricated by the laser direct metal deposition process, Journal of Manufacturing Science and Engineering-Transactions of the Asme 128(3) (2006) 691-696.

[5] B.V. Krishna, S. Bose, A. Bandyopadhyay, Laser Processing of Net-Shape NiTi Shape Memory Alloy, Metallurgical and Materials Transactions A 38(5) (2007) 1096-1103.

[6] J. Ma, B. Franco, G. Tapia, K. Karayagiz, L. Johnson, J. Liu, R. Arroyave, I. Karaman, A. Elwany, Spatial control of functional response in 4D-printed active metallic structures, Scientific Reports 7(1) (2017) 1-8.

[7] C. Haberland, H. Meier, J. Frenzel, On the properties of Ni-rich NiTi shape memory parts produced by selective laser melting, Smart Materials, Adaptive Structures and Intelligent Systems, American Society of Mechanical Engineers, 2012, pp. 97-104.

[8] S. Saedi, A.S. Turabi, M.T. Andani, C. Haberland, H. Karaca, M.J.J.o.A. Elahinia, Compounds, The influence of heat treatment on the thermomechanical response of Ni-rich NiTi alloys manufactured by selective laser melting, 677 (2016) 204-210.

[9] S. Dadbakhsh, M. Speirs, J. Van Humbeeck, J.-P.J.M.b. Kruth, Laser additive manufacturing of bulk and porous shape-memory NiTi alloys: From processes to potential biomedical applications, 41(10) (2016) 765-774.

[10] Q. Zhou, M.D. Hayat, G. Chen, S. Cai, X. Qu, H. Tang, P.J.M.S. Cao, E. A, Selective electron beam melting of NiTi: Microstructure, phase transformation and mechanical properties, 744 (2019) 290-298.

[11] T. Bormann, R. Schumacher, B. Müller, M. Mertmann, M. de Wild, Tailoring Selective Laser Melting Process Parameters for NiTi Implants, Journal of Materials Engineering and Performance 21(12) (2012) 2519-2524.

[12] S. Dadbakhsh, B. Vrancken, J.-P. Kruth, J. Luyten, J. Van Humbeeck, Texture and anisotropy in selective laser melting of NiTi alloy, Materials Science and Engineering A 650 (2016) 225-232.

[13] M.D. Hayat, G. Chen, N. Liu, S. Khan, H.P. Tang, P. Cao, Physical and tensile properties of NiTi alloy by selective electron beam melting, Key Engineering Materials, Trans Tech Publ, 2018, pp. 148-154.

[14] S. Shiva, I. Palani, S. Mishra, C. Paul, L.J.O. Kukreja, L. Technology, Investigations on the influence of composition in the development of Ni–Ti shape memory alloy using laser based additive manufacturing, 69 (2015) 44-51.

[15] R.F. Hamilton, T.A. Palmer, B.A.J.S.M. Bimber, Spatial characterization of the thermal-induced phase transformation throughout as-deposited additive manufactured NiTi bulk builds, 101 (2015) 56-59.

[16] B.A. Bimber, R.F. Hamilton, J. Keist, T.A. Palmer, Anisotropic microstructure and superelasticity of additive manufactured NiTi alloy bulk builds using laser directed energy deposition, Materials Science and Engineering: A 674 (2016) 125-134.

[17] R.F. Hamilton, B.A. Bimber, T.A.J.J.o.A. Palmer, Compounds, Correlating microstructure and superelasticity of directed energy deposition additive manufactured Ni-rich NiTi alloys, 739 (2018) 712-722.

[18] B.A. Bimber, R.F. Hamilton, T.A.J.S.M. Palmer, Superelasticity, Ni-Concentration dependence of directed energy deposited NiTi alloy microstructures, 5(2) (2019) 182-187.

[19] C. Wang, X. Tan, Z. Du, S. Chandra, Z. Sun, C. Lim, S. Tor, C. Lim, C.J.J.o.M.P.T. Wong, Additive manufacturing of NiTi shape memory alloys using pre-mixed powders, 271 (2019) 152-161.

[20] M. Das, V.K. Balla, T.S. Kumar, I. Manna, Fabrication of biomedical implants using laser engineered net shaping (LENS™), 72(3) (2013) 169-174.

[21] T. Habijan, C. Haberland, H. Meier, J. Frenzel, J. Wittsiepe, C. Wuwer, C. Greulich, T. Schildhauer, M.J.M.S. Köller, E. C, The biocompatibility of dense and porous nickel–titanium produced by selective laser melting, 33(1) (2013) 419-426.

[22] X. Wang, S. Kustov, J.J.M. Van Humbeeck, A short review on the microstructure, transformation behavior and functional properties of NiTi shape memory alloys fabricated by selective laser melting, 11(9) (2018) 1683.

[23] N.S. Moghaddam, S. Saedi, A. Amerinatanzi, E. Saghaian, A. Jahadakbar, H. Karaca, M. Elahinia, Selective laser melting of Ni-rich NiTi: Selection of process parameters and the superelastic response, in: H.E. Naguib (Ed.), Behavior and Mechanics of Multifunctional Materials and Composites Xii2018.

[24] M. Mehrpouya, A. Gisario, A. Rahimzadeh, M. Nematollahi, K.S. Baghbaderani, M. Elahinia, A prediction model for finding the optimal laser parameters in additive manufacturing of NiTi shape memory alloy, Int. J. Adv. Manuf. Technol. 105(11) (2019) 4691-4699.

[25] X. Wang, J. Yu, J. Liu, L. Chen, Q. Yang, H. Wei, J. Sun, Z. Wang, Z. Zhang, G. Zhao, Effect of process parameters on the phase transformation behavior and tensile properties of NiTi shape memory alloys fabricated by selective laser melting, Additive Manufacturing 36 (2020) 101545.

[26] J.M. Walker, C. Haberland, M. Taheri Andani, H.E. Karaca, D. Dean, M. Elahinia, Process development and characterization of additively manufactured nickel–titanium shape memory parts, Journal of Intelligent Material Systems and Structures 27(19) (2016) 2653-2660.

[27] M. Mahmoudi, G. Tapia, B. Franco, J. Ma, R. Arroyave, I. Karaman, A. Elwany, On the printability and transformation behavior of nickel-titanium shape memory alloys

fabricated using laser powder-bed fusion additive manufacturing, Journal of Manufacturing Processes 35 (2018) 672-680.

[28] H. Meier, C.J.M.u.W. Haberland, Experimental studies on selective laser melting of metallic parts, 39(9) (2008) 665-670.

[29] M. Letenneur, A. Kreitcberg, V. Brailovski, Optimization of Laser Powder Bed Fusion Processing Using a Combination of Melt Pool Modeling and Design of Experiment Approaches: Density Control, Journal of Manufacturing and Materials Processing 3(1) (2019).

[30] A. Foroozmehr, M. Badrossamay, E. Foroozmehr, S.i. Golabi, Finite Element Simulation of Selective Laser Melting process considering Optical Penetration Depth of laser in powder bed, Materials & Design 89 (2016) 255-263.

[31] L. Johnson, M. Mahmoudi, B. Zhang, R. Seede, X. Huang, J.T. Maier, H.J. Maier, I. Karaman, A. Elwany, R. Arróyave, Assessing printability maps in additive manufacturing of metal alloys, Acta Materialia 176 (2019) 199-210.

[32] R. Seede, D. Shoukr, B. Zhang, A. Whitt, S. Gibbons, P. Flater, A. Elwany, R. Arroyave, I. Karaman, An ultra-high strength martensitic steel fabricated using selective laser melting additive manufacturing: Densification, microstructure, and mechanical properties, Acta Materialia 186 (2020) 199-214.

[33] A. Jahadakbar, M. Nematollahi, K. Safaei, P. Bayati, G. Giri, H. Dabbaghi, D. Dean, M.J.M. Elahinia, Design, modeling, additive manufacturing, and polishing of stiffness-modulated porous nitinol bone fixation plates followed by thermomechanical and composition analysis, 10(1) (2020) 151.

[34] Z. Xiong, Z. Li, Z. Sun, S. Hao, Y. Yang, M. Li, C. Song, P. Qiu, L. Cui, Selective laser melting of NiTi alloy with superior tensile property and shape memory effect, Journal of Materials Science & Technology 35(10) (2019) 2238-2242.

[35] J.-N. Zhu, E. Borisov, X. Liang, E. Farber, M. Hermans, V.J.A.M. Popovich, Predictive analytical modelling and experimental validation of processing maps in additive manufacturing of nitinol alloys, 38 (2021) 101802.

[36] J. Ma, B. Franco, G. Tapia, K. Karayagiz, L. Johnson, J. Liu, R. Arroyave, I. Karaman, A. Elwany, Spatial Control of Functional Response in 4D-Printed Active Metallic Structures, Scientific Reports 7 (2017).

[37] J. Sam, B. Franco, J. Ma, I. Karaman, A. Elwany, J.H. Mabe, Tensile actuation response of additively manufactured nickel-titanium shape memory alloys, Scripta Materialia 146 (2018) 164-168.

[38] B.E. Franco, J. Ma, B. Loveall, G.A. Tapia, K. Karayagiz, J. Liu, A. Elwany, R. Arroyave, I. Karaman, A Sensory Material Approach for Reducing Variability in Additively Manufactured Metal Parts, Scientific Reports 7 (2017).

[39] S. Saedi, N. Shayesteh Moghaddam, A. Amerinatanzi, M. Elahinia, H.E. Karaca, On the effects of selective laser melting process parameters on microstructure and thermomechanical response of Ni-rich NiTi, Acta Materialia 144 (2018) 552-560.

[40] J. Frenzel, E.P. George, A. Dlouhy, C. Somsen, M.-X. Wagner, G. Eggeler, Influence of Ni on martensitic phase transformations in NiTi shape memory alloys, Acta Materialia 58(9) (2010) 3444-3458.

[41] B. Kockar, I. Karaman, J.I. Kim, Y.I. Chumlyakov, J. Sharp, C.J. Yu, Thermomechanical cyclic response of an ultrafine-grained NiTi shape memory alloy, Acta Materialia 56(14) (2008) 3630-3646.

[42] C. Haberland, M. Elahinia, J.M. Walker, H. Meier, J. Frenzel, On the development of high quality NiTi shape memory and pseudoelastic parts by additive manufacturing, Smart Materials and Structures 23(10) (2014) 104002.

[43] M. Speirs, X. Wang, S. Van Baelen, A. Ahadi, S. Dadbakhsh, J.-P. Kruth, J.J.S.M. Van Humbeeck, Superelasticity, On the transformation behavior of NiTi shape-memory alloy produced by SLM, 2(4) (2016) 310-316.

[44] M. Elahinia, N.S. Moghaddam, M.T. Andani, A. Amerinatanzi, B.A. Bimber, R.F. Hamilton, Fabrication of NiTi through additive manufacturing: A review, Progress in Materials Science 83 (2016) 630-663.

[45] Y. Yang, J. Zhan, B. Li, J. Lin, J. Gao, Z. Zhang, L. Ren, P. Castany, T.J.M. Gloriant, Laser beam energy dependence of martensitic transformation in SLM fabricated NiTi shape memory alloy, 6 (2019) 100305.

[46] T. Bormann, B. Müller, M. Schinhammer, A. Kessler, P. Thalmann, M. de Wild, Microstructure of selective laser melted nickel–titanium, Mater. Charact. 94 (2014) 189-202.

[47] K.S. Baghbaderani, M. Nematollahi, P. Bayatimalayeri, H. Dabbaghi, A. Jahadakbar, M.J.a.p.a. Elahinia, Mechanical Evaluation Of Selective Laser Melted Ni-Rich Niti: Compression, Tension, And Torsion, (2020).

[48] A. Bagheri, M.J. Mahtabi, N.J.J.o.M.P.T. Shamsaei, Fatigue behavior and cyclic deformation of additive manufactured NiTi, 252 (2018) 440-453.

[49] N.S. Moghaddam, S. Saedi, A. Amerinatanzi, A. Hinojos, A. Ramazani, J. Kundin, M.J. Mills, H. Karaca, M. Elahinia, Achieving superelasticity in additively manufactured NiTi in compression without post-process heat treatment, Scientific Reports 9(1) (2019) 1-11.

[50] S.-F. Ou, B.-Y. Peng, Y.-C. Chen, M.-H.J.M. Tsai, Manufacturing and characterization of NiTi alloy with functional properties by selective laser melting, 8(5) (2018) 342.

[51] Y. Yang, J. Zhan, Z. Sun, H. Wang, J. Lin, Y. Liu, L.J.J.o.A. Zhang, Compounds, Evolution of functional properties realized by increasing laser scanning speed for the selective laser melting fabricated NiTi alloy, 804 (2019) 220-229.

[52] H. Sehitoglu, I. Karaman, R. Anderson, X. Zhang, K. Gall, H. Maier, Y. Chumlyakov, Compressive response of NiTi single crystals, Acta Materialia 48(13) (2000) 3311-3326.

[53] K. Gall, H. Sehitoglu, R. Anderson, I. Karaman, Y.I. Chumlyakov, I.V.J.M.S. Kireeva, E. A, On the mechanical behavior of single crystal NiTi shape memory alloys and related polycrystalline phenomenon, 317(1-2) (2001) 85-92.

[54] C.A. Biffi, J. Fiocchi, F. Valenza, P. Bassani, A. Tuissi, Selective Laser Melting of NiTi Shape Memory Alloy: Processability, Microstructure, and Superelasticity, Shape Memory and Superelasticity 6(3) (2020) 342-353.

[55] B.E. Franco, Engineering the martensitic transformation hysteresis of Ni-rich NiTi alloys, 2014.

[56] F. Jiang, Y. Liu, H. Yang, L. Li, Y. Zheng, Effect of ageing treatment on the deformation behaviour of Ti-50.9 at.% Ni, Acta Materialia 57(16) (2009) 4773-4781.

[57] A. Sinha, B. Mondal, P.P.J.M.S. Chattopadhyay, E. A, Mechanical properties of Ti–(∼ 49 at%) Ni shape memory alloy, part II: Effect of ageing treatment, 561 (2013) 344-351.

[58] H. Mohamad, A.S. Mahmud, M.N. Nashrudin, M.F. Razali, Effect of ageing temperatures on pseudoelasticity of Ni-rich NiTi shape memory alloy, AIP Conference Proceedings, AIP Publishing LLC, 2018, p. 020008.

[59] D. Favier, Y. Liu, L. Orgeas, A. Sandel, L. Debove, P. Comte-Gaz, Influence of thermomechanical processing on the superelastic properties of a Ni-rich Nitinol shape memory alloy, Materials Science

Engineering: A 429(1-2) (2006) 130-136.

[60] X. Liu, Y. Wang, D. Yang, M.J.M.C. Qi, The effect of ageing treatment on shape-setting and superelasticity of a nitinol stent, 59(4) (2008) 402-406.

[61] C. Haberland, M. Elahinia, J. Walker, H. Meier, J. Frenzel, Additive manufacturing of shape memory devices and pseudoelastic components, ASME 2013 conference on smart materials, adaptive structures and intelligent systems, American Society of Mechanical Engineers Digital Collection, 2013.

[62] J. Frenzel, A. Wieczorek, I. Opahle, B. Maass, R. Drautz, G. Eggeler, On the effect of alloy composition on martensite start temperatures and latent heats in Ni-Ti-based shape memory alloys, Acta Materialia 90 (2015) 213-231.

[63] T. Eagar, N. Tsai, Temperature fields produced by traveling distributed heat sources, Welding journal 62(12) (1983) 346-355.

[64] C.D. Boley, S.C. Mitchell, A.M. Rubenchik, S.S.Q. Wu, Metal powder absorptivity: modeling and experiment, Appl. Opt. 55(23) (2016) 6496-6500.

[65] C. Zanotti, P. Giuliani, P. Bassani, Z. Zhang, A. Chrysanthou, Comparison between the thermal properties of fully dense and porous NiTi SMAs, Intermetallics 18(1) (2010) 14-21.

[66] F. Cheng, L. Hu, J.N. Reddy, I. Karaman, E. Hoffman, M. Radovic, Temperature-dependent thermal properties of a shape memory alloy/MAX phase composite: Experiments and modeling, Acta Materialia 68 (2014) 267-278.

[67] M. Mahmoudi, G. Tapia, K. Karayagiz, B. Franco, J. Ma, R. Arroyave, I. Karaman, A. Elwany, Multivariate calibration and experimental validation of a 3d finite element thermal model for laser powder bed fusion metal additive manufacturing, Integrating Materials and Manufacturing Innovation 7(3) (2018) 116-135.

[68] B. Zhang, R. Seede, L. Xue, K.C. Atli, C. Zhang, A. Whitt, I. Karaman, R. Arroyave, A. Elwany, An Efficient Framework for Printability Assessment in Laser Powder Bed Fusion Metal Additive Manufacturing, Additive Manufacturing (2021).

[69] U.S. Bertoli, A.J. Wolfer, M.J. Matthews, J.-P.R. Delplanque, J.M.J.M. Schoenung, Design, On the limitations of volumetric energy density as a design parameter for selective laser melting, 113 (2017) 331-340.

[70] J.C. Heigel, B.M. Lane, Measurement of the melt pool length during single scan tracks in a commercial laser powder bed fusion process, Journal of Manufacturing Science and Engineering 140(5) (2018).

[71] B. Cheng, S. Shrestha, K. Chou, Stress and deformation evaluations of scanning strategy effect in selective laser melting, Additive Manufacturing 12 (2016) 240-251.

[72] Z.X. Khoo, Y. Liu, Z.H. Low, J. An, C.K. Chua, K.F. Leong, Fabrication of SLM NiTi shape memory alloy via repetitive laser scanning, Shape Memory and Superelasticity 4(1) (2018) 112-120.

[73] S. Khademzadeh, S. Carmignato, N. Parvin, F. Zanini, P.F. Bariani, Micro porosity analysis in additive manufactured NiTi parts using micro computed tomography and electron microscopy, Materials & Design 90 (2016) 745-752.

[74] R. Li, J. Liu, Y. Shi, L. Wang, W. Jiang, Balling behavior of stainless steel and nickel powder during selective laser melting process, The International Journal of Advanced Manufacturing Technology 59(9) (2012) 1025-1035.

[75] C. Haberland, M. Elahinia, J.M. Walker, H. Meier, J. Frenzel, On the development of high quality NiTi shape memory and pseudoelastic parts by additive manufacturing, Smart Materials and Structures 23(10) (2014).

[76] D.C. Ren, H.B. Zhang, Y.J. Liu, S.J. Li, W. Jin, R. Yang, L.C. Zhang, Microstructure and properties of equiatomic Ti-Ni alloy fabricated by selective laser melting, Mater. Sci. Eng. A-Struct. Mater. Prop. Microstruct. Process. 771 (2020) 10.

[77] T. Bormann, B. Müller, M. Schinhammer, A. Kessler, P. Thalmann, M. de Wild, Microstructure of selective laser melted nickel-titanium, Mater. Charact. 94 (2014) 189-202.

[78] J. Khalil-Allafi, A. Dlouhy, G. Eggeler, Ni4Ti3-precipitation during aging of NiTi shape memory alloys and its influence on martensitic phase transformations, Acta Materialia 50(17) (2002) 4255-4274.

[79] J.K. Allafi, X. Ren, G. Eggeler, The mechanism of multistage martensitic transformations in aged Ni-rich NiTi shape memory alloys, Acta Materialia 50(4) (2002) 793-803.

[80] K. Otsuka, X. Ren, Physical metallurgy of Ti–Ni-based shape memory alloys, Progress in Materials Science 50(5) (2005) 511-678.

[81] G. Laplanche, T. Birk, S. Schneider, J. Frenzel, G. Eggeler, Effect of temperature and texture on the reorientation of martensite variants in NiTi shape memory alloys, Acta Materialia 127 (2017) 143-152.

[82] Z. Wu, A. Mahmud, J. Zhang, Y. Liu, H.J.M. Yang, Design, Surface oxidation of NiTi during thermal exposure in flowing argon environment, 140 (2018) 123-133.

[83] T. Hara, T. Ohba, E. Okunishi, K. Otsuka, Structural study of R-phase in Ti-50.23 at.% Ni and Ti-47.75 at.% Ni-1.50 at.% Fe alloys, Materials Transactions, JIM 38(1) (1997) 11-17.

[84] M.-X. Wagner, S. Dey, H. Gugel, J. Frenzel, C. Somsen, G.J.I. Eggeler, Effect of low-temperature precipitation on the transformation characteristics of Ni-rich NiTi shape memory alloys during thermal cycling, 18(6) (2010) 1172-1179.

[85] A. International, B962-17 Standard Test Methods for Density of Compacted or Sintered Powder Metallurgy (PM) Products Using Archimedes' Principle, ASTM International, West Conshohocken, PA, 2017.

[86] L. Xue, K.C. Atli, S. Picak, C. Zhang, B. Zhang, A. Elwany, R. Arroyave, I. Karaman, Controlling martensitic transformation characteristics in defect-free NiTi shape memory alloys fabricated using laser powder bed fusion and a process optimization framework, Acta Materialia 215 (2021) 117017.

[87] B. Zhang, R. Seede, L. Xue, K.C. Atli, C. Zhang, A. Whitt, I. Karaman, R. Arroyave, A. Elwany, An Efficient Framework for Printability Assessment in Laser Powder Bed Fusion Metal Additive Manufacturing, Additive Manufacturing 46 (2021) 102018.

[88] M. Bram, M. Bitzer, H.P. Buchkremer, D. Stover, Reproducibility Study of NiTi Parts Made by Metal Injection Molding, Journal of Materials Engineering and Performance 21(12) (2012) 2701-2712.

[89] L.A. Parry, I.A. Ashcroft, R.D. Wildman, Geometrical effects on residual stress in selective laser melting, Additive Manufacturing 25 (2019) 166-175.

[90] S. Miyazaki, Y. Kohiyama, K. Otsuka, T.W. Duerig, Effects of Several Factors on the Ductility of the Ti-Ni Alloy, Materials Science Forum 56-58 (1990) 765-770.

[91] K. Gall, H. Sehitoglu, R. Anderson, I. Karaman, Y.I. Chumlyakov, I.V. Kireeva, On the mechanical behavior of single crystal NiTi shape memory alloys and related polycrystalline phenomenon, Materials Science and Engineering A 317(1-2) (2001) 85-92.

[92] K. Gall, H. Sehitoglu, Y.I. Chumlyakov, I.V. Kireeva, Tension-compression asymmetry of the stress-strain response in aged single crystal and polycrystalline NiTi, Acta Materialia 47(4) (1999) 1203-1217.

[93] K. Gall, N. Yang, H. Sehitoglu, Y.I. Chumlyakov, Fracture of precipitated NiTi shape memory alloys, International Journal of Fracture 109(2) (2001) 189-207.

[94] S.R. Suwas, Ranjit Kumar, Crystallographic Texture of Materials, Springer2014.

[95] N.S. Moghaddam, S. Saedi, A. Amerinatanzi, A. Hinojos, A. Ramazani, J. Kundin, M.J. Mills, H. Karaca, M. Elahinia, Achieving superelasticity in additively manufactured NiTi in compression without post-process heat treatment, Scientific Reports 9 (2019).

[96] M. Nematollahi, S.E. Saghaian, K. Safaei, P. Bayati, P. Bassani, C. Biffi, A. Tuissi, H. Karaca, M. Elahinia, Building orientation-structure-property in laser powder bed fusion of NiTi shape memory alloy, J Alloy Compd 873 (2021).

[97] O. Andreau, I. Koutiri, P. Peyre, J.-D. Penot, N. Saintier, E. Pessard, T. De Terris, C. Dupuy, T. Baudin, Texture control of 316L parts by modulation of the melt pool morphology in selective laser melting, Journal of Materials Processing Technology 264 (2019) 21-31.

[98] K.A. Sofinowski, S. Raman, X. Wang, B. Gaskey, M. Seita, Layer-wise engineering of grain orientation (LEGO) in laser powder bed fusion of stainless steel 316L, Additive Manufacturing 38 (2021).

[99] S.-H. Sun, T. Ishimoto, K. Hagihara, Y. Tsutsumi, T. Hanawa, T. Nakano, Excellent mechanical and corrosion properties of austenitic stainless steel with a unique crystallographic lamellar microstructure via selective laser melting, Scripta Materialia 159 (2019) 89-93.

[100] C.A. Biffi, P. Bassani, J. Fiocchi, A. Tuissi, Microstructural and Mechanical Response of NiTi Lattice 3D Structure Produced by Selective Laser Melting, Metals-Basel 10(6) (2020).

[101] R.R. Dehoff, M.M. Kirka, W.J. Sames, H. Bilheux, A.S. Tremsin, L.E. Lowe, S.S. Babu, Site specific control of crystallographic grain orientation through electron beam additive manufacturing, Materials Science and Technology 31(8) (2015) 931-938.

[102] F. Geiger, K. Kunze, T. Etter, Tailoring the texture of IN738LC processed by selective laser melting (SLM) by specific scanning strategies, Materials Science and Engineering A 661 (2016) 240-246.

[103] E.Y. Panchenko, Y.I. Chumlyakov, I.V. Kireeva, A.V. Ovsyannikov, H. Sehitoglu, I. Karaman, Y.H.J. Maier, Effect of disperse Ti3N4 particles on the martensitic transformations in titanium nickelide single crystals, Physics of Metals and Metallography 106(6) (2008) 577-589.

[104] J.I. Kim, Y.N. Liu, S. Miyazaki, Ageing-induced two-stage R-phase transformation in Ti-50.9at.%Ni, Acta Materialia 52(2) (2004) 487-499.

[105] Y.I. Chumlyakov, S.P. Efimenko, I.V. Kireeva, E.Y. Panchenko, H. Sehitogly, K. Gall, L.H. Yahia, Effects of shape memory and superelasticity in aged TiNi single crystals, Doklady Physics 46(12) (2001) 849-852.

[106] H. Sehitoglu, J. Jun, X. Zhang, I. Karaman, Y. Chumlyakov, H.J. Maier, K. Gall, Shape memory and pseudoelastic behavior of 51.5%Ni-Ti single crystals in solutionized and overaged state, Acta Materialia 49(17) (2001) 3609-3620.

[107] B.A. Bimber, R.F. Hamilton, J. Keist, T.A. Palmer, Anisotropic microstructure and superelasticity of additive manufactured NiTi alloy bulk builds using laser directed energy deposition, Materials Science and Engineering A 674 (2016) 125-134.

[108] J. Gan, L. Duan, F. Li, Y. Che, Y. Zhou, S. Wen, C. Yan, Effect of laser energy density on the evolution of Ni4Ti3 precipitate and property of NiTi shape memory alloys prepared by selective laser melting, J Alloy Compd 869 (2021) 159338.

[109] B.D. Ingale, W.C. Wei, P.C. Chang, Y.K. Kuo, S.K. Wu, Anomalous transport and thermal properties of NiTi and with Cu and Fe-doped shape memory alloys near the martensitic transition, Journal of Applied Physics 110(11) (2011).